LIÈGE université
Sciences Appliquées

AIAA

OPULOX-1

Ultra Premium, Long Range Business Jet

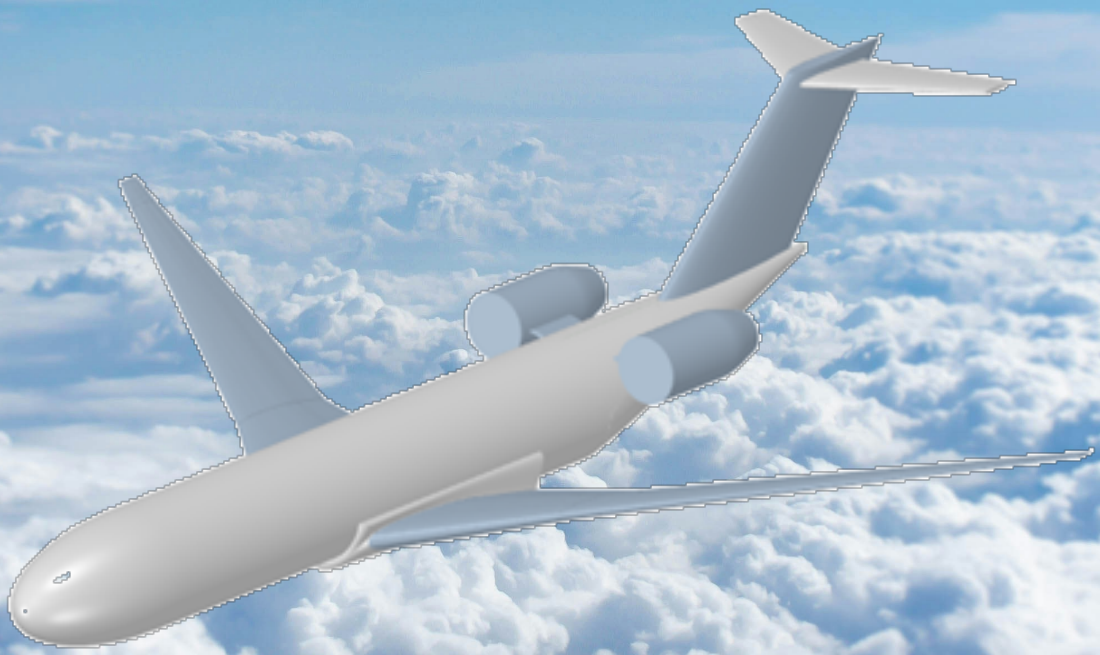

2024–2025 Graduate Team Aircraft Design Competition

Team

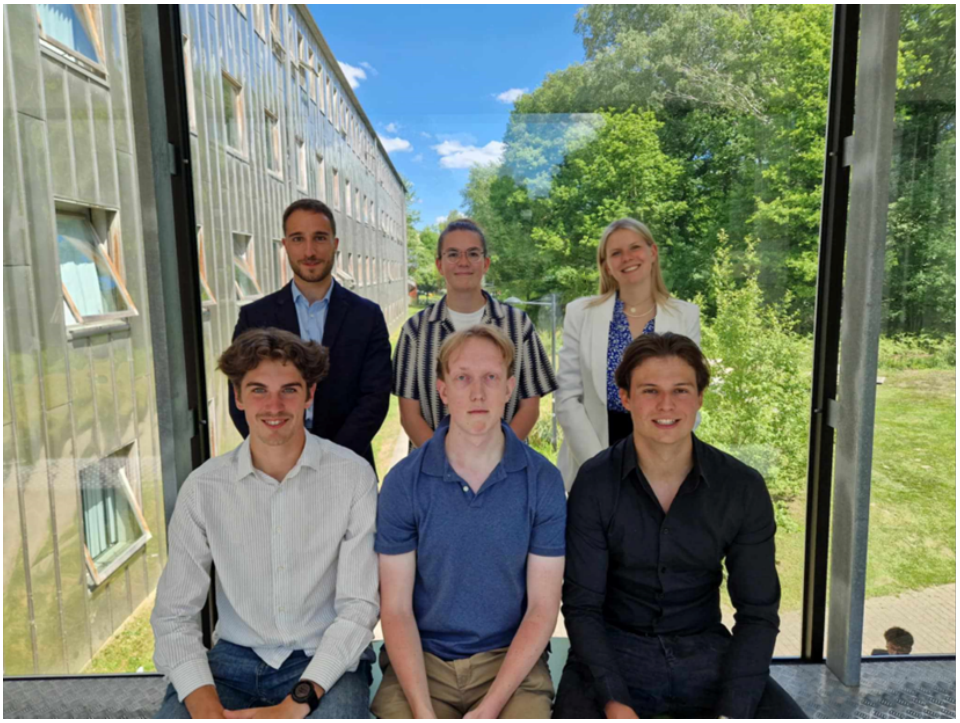

Name	Student number	AIAA number	Signature	
Claire Jewasinski	S212564	1746880		
Tyler Mattson	S2403268	1747110		
Matteo Schmetz	S215386	1749677		
Noam Schmitz	S214896	1749908		
Thomas Ucci	S214900	1749147		
Irina Vanhaverbeke	S214770	1746881		

Professors : Thomas Andrianne and Ludovic Noels.

Assistants : Arnaud Budo and Paul Dechamps

Cost
M$ 39.5

MTOW
91,238 lbs

Passengers
8

Mach
0.935

takeoff
4,268 ft

Range
8,000 NM

Landing
1,699 ft

Span
101.71 ft

Contents

1 Introduction

In today's world where international mobility is a key asset, the demand for ultra-premium, long-range business jets continues to grow steadily. Private jets offer unmatched advantages such as time savings, flexibility, and unparalleled comfort, allowing business professionals to optimize their productivity during travel. In this context, the 2024–2025 AIAA Graduate Team Aircraft Design Competition challenged participants to develop a next-generation business jet, combining luxurious interiors, long range capabilities, and transonic cruise performance, while maintaining operability from shorter runways.

In response to this demanding proposal, the OPULOX-1 was conceived. Designed to meet and exceed all mandatory requirements, the OPULOX-1 offers an impressive maximum cruise Mach number of 0.935, a maximum range of 8,000 nautical miles, and the ability to operate from runways as short as 4,268 feet for takeoff and 1,699 feet for landing. The project also focused heavily on ensuring maximum comfort, incorporating a wide fuselage offering a spacious and luxurious cabin with a volume of 4,944 ft^3, one of the largest among competing aircraft. The OPULOX-1 is configured to accommodate 8 passengers in complete luxury, alongside 2 pilots and 1 flight attendant, fully aligning with the competition's mission requirements. The name OPULOX-1 comes from the combination of its key strengths. The mix between *opulence* for the luxury, and *velox* for the high velocity capabilities of OPULOX-1.

The design process was built around three primary pillars: aerodynamic performance, structural feasibility, and passenger experience. A high-aspect-ratio wing and a span-reduction mechanism were selected to ensure airport compatibility without compromising aerodynamic efficiency. Powered by two GE Passport-class engines, the OPULOX-1 achieves the necessary thrust for both short takeoff operations and high-speed cruise, while ensuring fuel efficiency for extended missions.

The OPULOX-1 development carefully addressed the design passenger mission, as well as the Aspen Economic Mission and the Napa Economic Mission outlined in the competition statement. Special attention was given to short field performance to open access to strategic airports near major cities, a strong selling point in today's premium jet market.

This report presents the comprehensive development of the OPULOX-1, starting from the mission analysis and general methodology, leading through the aerodynamic and structural design phases, propulsion selection, and concluding with performance evaluations, cost analysis, and trade studies that highlight the choices and innovations made during the project.

2 Mission analysis

The objective is to design an ultra-premium long-range business jet. The jet must be able to achieve 3 different missions: Design Passenger Mission, Aspen Economic Mission, and Napa Economic Mission. The main requirements of each mission are summarized in Tab.1.

The Design Passenger Mission presents the most demanding scenario for aircraft design. Consequently, the aircraft is specifically designed to meet the requirements of this mission.

In comparison, the Aspen Economic Mission requires a shorter range and longer takeoff and landing distances. Therefore, this mission being less demanding than the primary mission, it does not pose any challenge for the aircraft.

However, the Napa Economic Mission imposes the most stringent takeoff distance requirement among the three missions, despite having a shorter range. Given that the fuel required for this mission is significantly lower than that for the other two, the aircraft's takeoff weight is also reduced. As a result, it is initially assumed that the aircraft can operate within this distance constraint. This assumption will later be verified through a detailed evaluation of the takeoff performance.

General Requirements	
Minimum cruise Mach	0.85
Target cruise Mach	0.92
Certification	FAA 14 CFR Part 25
Design Passenger Mission	
Crew	2 pilots and 1 flight attendant
Passengers capacity	8 passengers
Range	8,000 nm
takeoff	6,000 foot runway
Landing	6,000 foot runway

Table 1: Main requirements of different missions.

Aspen Economic Mission	
Passengers capacity	4 passengers
Range	743.4 nm, from KNV to KASE
takeoff	8,000 foot runway, KVNY
Landing	8,006 foot runway, KASE
Altitude	7,821.52 ft

Table 2: Aspen Economic Mission

Napa Economic Mission	
Passengers capacity	8 passengers
Range	1,680 nm, from KAPC to MEX
takeoff	5,930 foot runway, KAPC
Landing	12,800 foot runway, MEX
Altitude	36.09 ft

Table 3: Napa Economic Mission

3 General methodology

The methodology used is represented in Fig. 3.1. The starting point is to design the biggest aspects of the aircraft based on the different mission requirements. Additionally, the goal of this aircraft is to provide a lot of space for passengers and to be able to takeoff and land on short distances. It is necessary to take these two additional objectives into account while designing aircraft components.

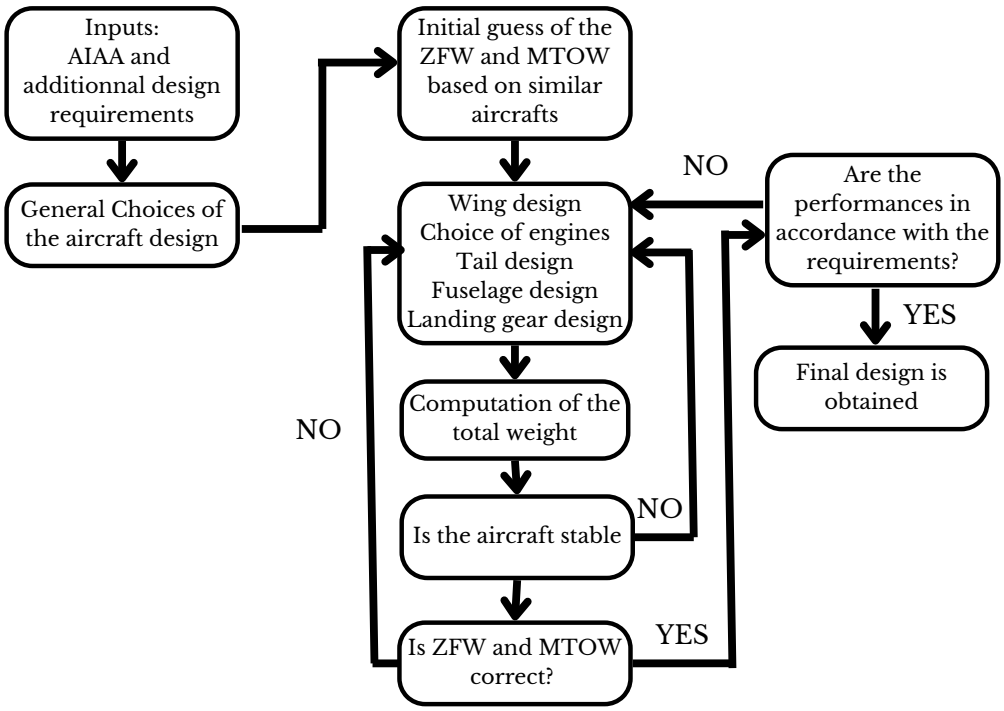

Figure 3.1: Design methodology scheme.

The first step of the iterative process involved researching existing aircraft with similar requirements. This research helped to make initial high-level design choices and estimate the aircraft's weight, ensuring that the initial assumptions were reasonably accurate. From these preliminary estimates, refinement of the design of each component with greater precision were done. During each iteration, the aircraft's stability has been verified . If instability was detected, component placements were adjusted, such as shifting the wing. Another key checkpoint was weight convergence, ensuring that the estimated weight remained consistent across iterations. Finally, the aircraft's performances were assessed. If it meets the required specifications, the final design is obtained.

4 Context and general choices

4.1 Market analysis

4.1.1 Existing aircraft

While the private jet market is well developed, finding an aircraft that meets all the AIAA competition requirements is not straightforward. Tab.4 presents a list of existing aircrafts that more or less satisfy the range requirement (8,000 NM). However, a closer analysis reveals that aircraft such as the Gulf-stream G800 or the Bombardier Global 8000 have takeoff and landing distances that are too long to comply with the short runway constraint defined in the proposal.

Aircraft	Range [NM]	Passenger [pers]	Cabin volume [ft³]	Takeoff distance [ft]	landing distance [ft]	price [M$]
Bombardier G7500	7,700	13	1,671.89	7,381.89	7,020.99	75
Bombardier G8000	7,900.11	17	2,360.53	5,905.512	2,460.63	73
Gulf-stream G800	7,996.76	17	2,311.43	6,000	3,000	71.5
Falcon 10x	7,505.39	8	1,700.08	4,921.26	3,937.01	75

Table 4: Existing aircrafts comparable to the OPULOX-1 [3].

4.1.2 Short takeoff

One of the main design goals of the OPULOX-1 is short takeoff capability.

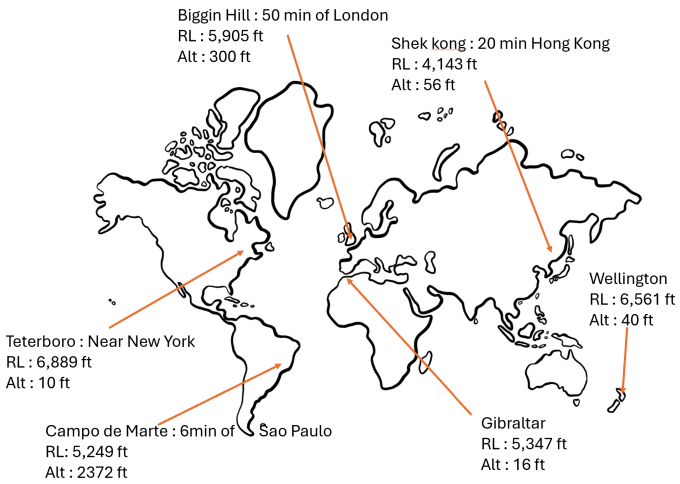

Figure 4.1: Small airport examples, RL = runway length, Alt = Altitude.

The figure Fig.4.1 highlights a selection of strategically located airports. These airports are situated near major cities but are

characterized by relatively short runways. After taking into account the CAA safety factor of 1.33 [9] on the takeoff distance, it is clear that neither of the well-known business jets discussed in Tab.4 is allowed to takeoff on the different airport runways showed in Fig.4.1. This is where the OPULOX-1 becomes so attractive. Being able to take off and land at such airports provides a significant operational advantage, offering greater flexibility, reducing transfer times for passengers, and opening access to destinations that are typically inaccessible to larger long-range business jets. This capability will make the OPULOX-1 particularly attractive on the market, offering unique operational versatility compared to competing aircraft in the same category.

4.2 General choices

Fuselage size

The cabin section was designed to ensure lot of spacing for the passengers, with a maximum width of 118.11 inches and a maximum height of 90.55 inches and a cabin volume of 4,944 ft^3, the cabin is the largest available on the market (Tab. 4) . The interior is also designed to ensure luxury experience with large seats.

Wing position and design

Wing of OPULOX-1 is low mounted to improve aerodynamic efficiency. As a span limitation was imposed by the Aspen-Pitkin airport [8] a foldable wingtip is included. This technology allows to increase the wing span in cruise condition leading to larger aerodynamic efficiency. A symmetric airfoil is selected at the wing root as it help with attachment on the fuselage and a cambered airfoil is located near wingtip to improve aerodynamic efficiency.

Tail shape

The T-tail shaped is selected for several reason. First, it positions the stabilizers away from the engine wake, wing wakes, wing vortices, and fuselage wake, minimizing interference and enhancing pitch control, longitudinal stability, and aerodynamic efficiency at high speeds. Additionally, the elevated position of the horizontal stabilizer helps prevent damage to control surfaces during takeoff and landing.

Engines selection

The engine was selected to be able to take off in short distances while ensuring a good efficiency at cruise. Due to the high thrust of the engine, the achievable mach in cruise reaches 0.935 in shorter range missions while it is maintained at 0.85 for longer range missions to improve flight efficiency. These engines are placed towards the rear of the fuselage leading to improved wing

aerodynamics (no disturbance due to engine). It also reduces the landing gear height as a ground clearance of at least 9 inches is required.

5 CAD representation

The CAD representation of the aircraft was created using ANSYS SpaceClaim, and consists of 5 principal components. Those being the fuselage, wing, engine, vertical tail, and horizontal tail. The CAD was constructed to give a realistic view of the shape and scale of the aircraft to use as an aid while designing.

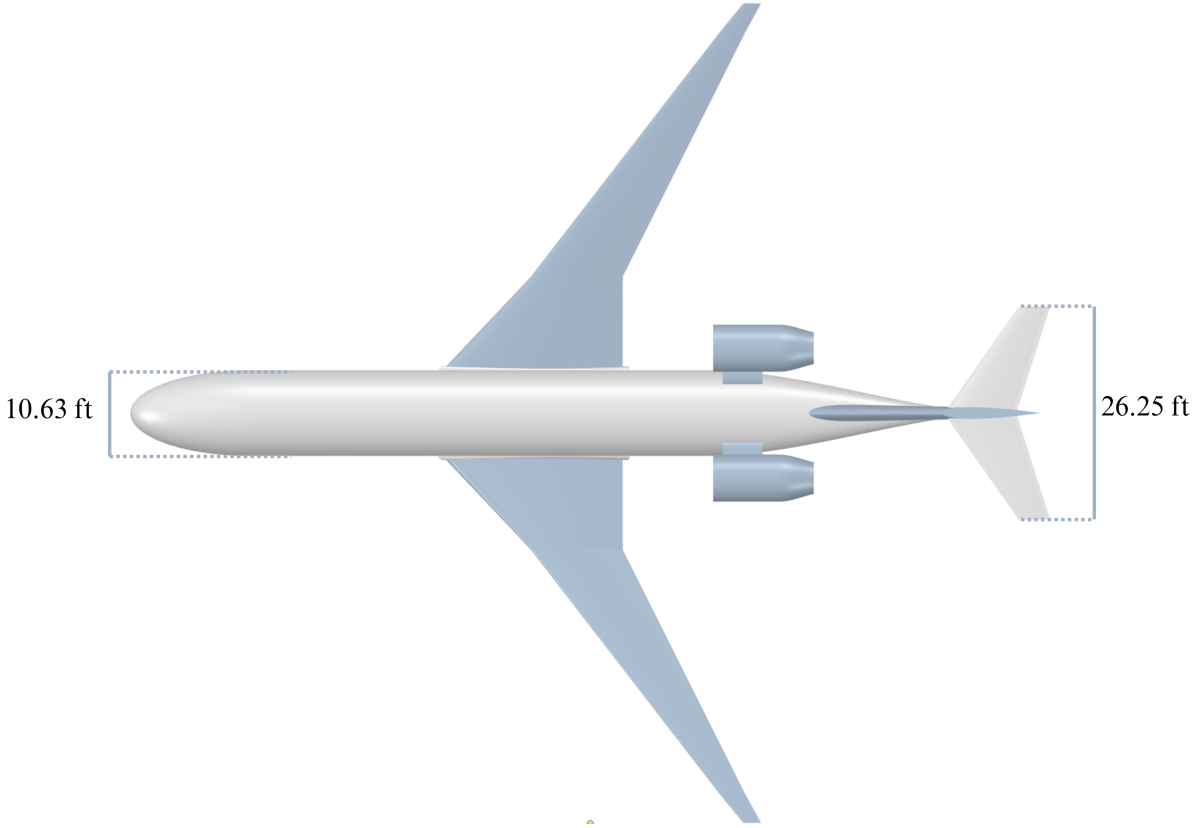

Figure 5.1: Top-Down View of Aircraft CAD.

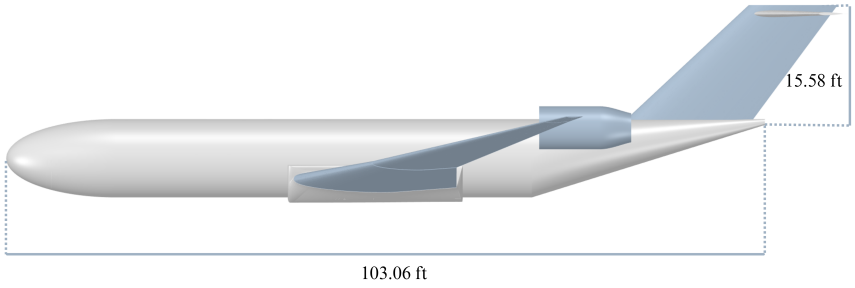

Figure 5.2: Side View of Aircraft CAD.

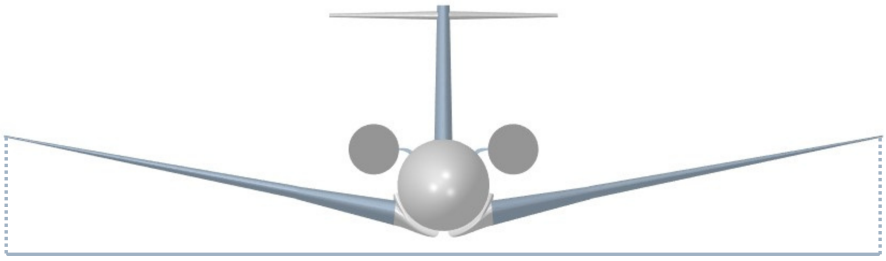

Figure 5.3: Front View of Aircraft CAD.

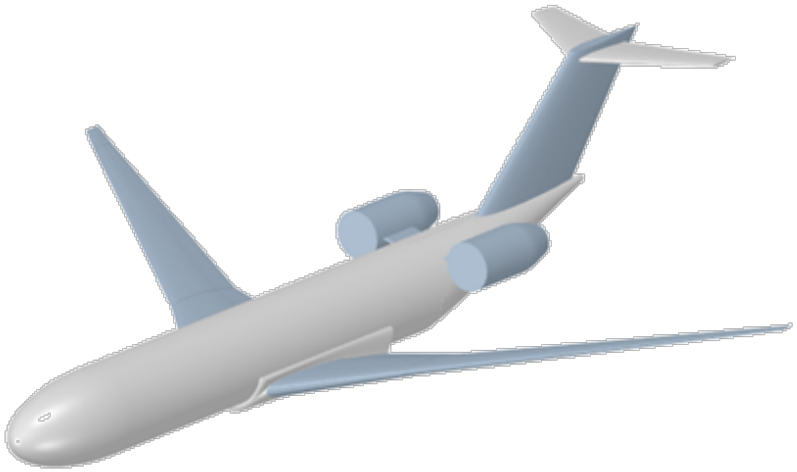

Figure 5.4: Isometric View of Aircraft CAD.

6 Components design

6.1 Fuselage

6.1.1 Cabin Design

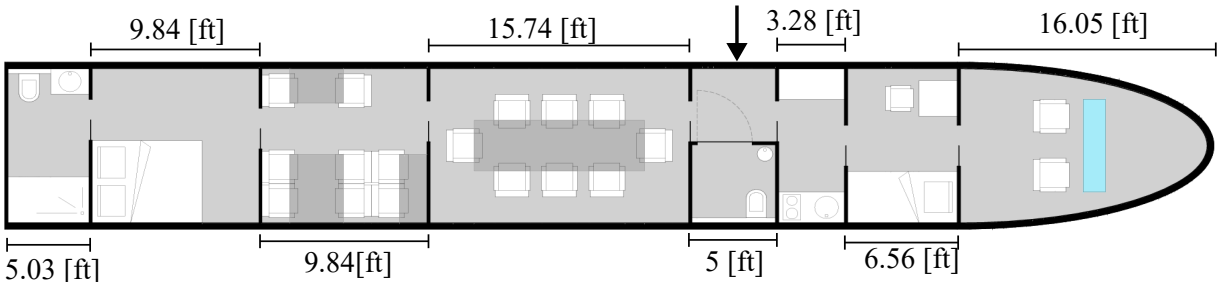

Figure 6.1: Layout Of Passengers Accommodations.

The interior design of the cabin is represented on Fig. 6.1. The door is indicated by the arrow. The total length of the cabin is 55.77 ft and is divided into 7 parts. The length of each subpart is represented of Fig. 6.1.

- **Crew section:** This place includes a one person bed, a small table, and a chair. This space is reserved for the crew to stay and to rest during the flight.
- **Kitchen:** This section measures 3.28 ft and includes a sink and cooking plates placed on a kitchen worktop. There is also plenty of storage.
- **Accessible bathroom:** The accessible bathroom is 4.67 ft wide.
- **Business room:** This section is designed such that seats are very comfortable measuring 26.5 inch wide. This section is also equipped with a large table allowing business meetings in a comfortable place. These seats are rotatable to allow a larger mobility. A TV is placed on the wall located on the left side of the plane looking in the flight direction.
- **Seats section:** This section includes 8 seats that are the same model as the ones in the business room, and tables that allow passengers to have create more space. There are 2.3 ft of free space between the seats facing each other and 1.31 ft free space for seats facing the wall. The aisle is 2.95 ft wide.
- **Bedroom:** This room includes a queen size bed of 60 inches by 80 inches.
- **Lavatory:** The last part of the jet is the bathroom including a shower of 2.62 ft wide, a sink, a mirror and a toilet.

6.1.2 Fuselage Cross Section

The fuselage has a maximum height of 7.55 ft and a width of 9.84 ft. These large dimensions ensure a high level of comfort and luxury. The baggage compartments are located at the bottom of the fuselage. It has a cross area of 12.11 ft^2. There is one baggage compartment located at 22.97 ft from the nose and measuring 13.12 ft long. The compartment is accessible via a door located in the part closer the nose.

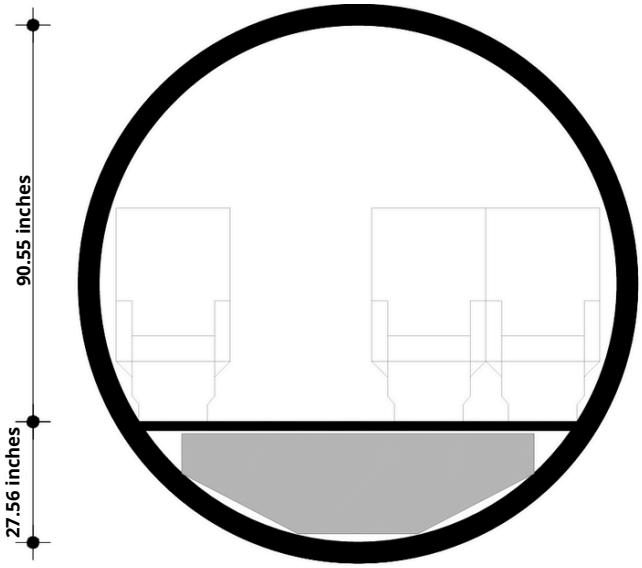

Figure 6.2: Cross section representation, the upper part represents a cut at 54.45 ft and the lower part a cut at 30 ft.

The location of the luggage compartment is represented in Fig. 6.3. The location of door is indicated by the arrow. The compartment allows a luggage volume of 198.72 ft^3. The compartments can be filled with the luggage using a treadmill.

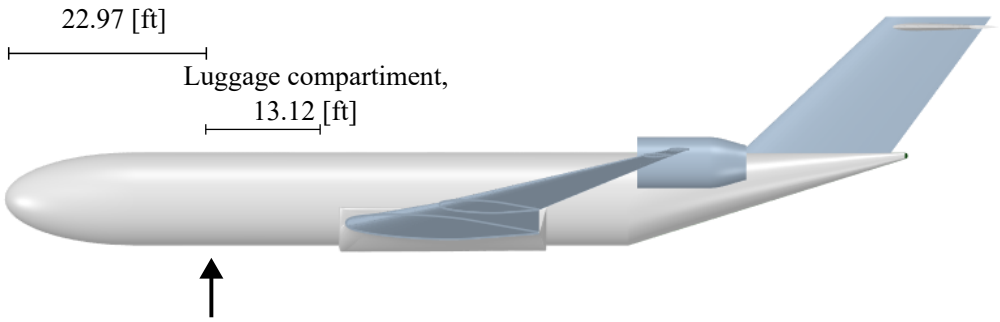

Figure 6.3: Luggage compartment location.

6.1.3 Cockpit And Tail Design

The cockpit has an ellipsoidal shape. The nose length to diameter ratio is fixed to 1.51 as it must be larger than 1.5 to avoid drag divergence. This results in a nose section length of 16.05 ft. Regarding the tail of the aircraft, the tail length to diameter ratio is equal to 2.98 leading to a 31.65 ft tail length.

6.2 Wing

6.2.1 Planform Design

To achieve long-range transonic flight, the principal goal of the wing design is to maximize the aspect ratio of the wing to reduce induced drag, mitigate the effects of drag increases in the transonic regime, and be capable of carrying the fuel needed to reach the required range of 8,000 NM.

The wing span has been limited to 95 ft due to one of the representative mission airports, Aspen-Pitkin [8], being prohibited to allow the operation of aircraft with a wingspan of over 95 ft. To mitigate this restriction folding wingtips were added to the end of each wing. Adding a wingtip of length 3.69 ft, that can be folded down, increases the total wingspan of the aircraft to 101.71 ft. This folding capability was created in CAD and is shown in Fig. 6.4.

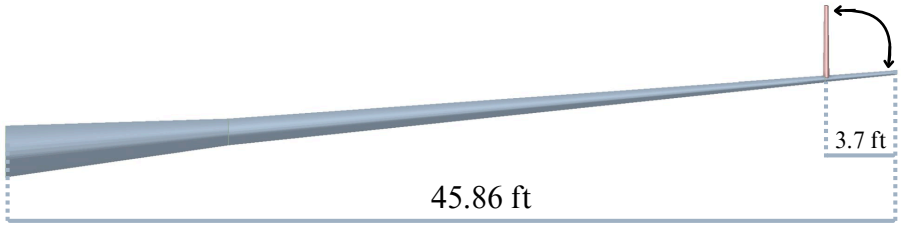

Figure 6.4: Wing CAD with foldable wingtip.

The wing-planform area is then determined using the goal of maximizing the aspect ratio while maintaining structural and size requirements. With a fixed wingspan the aspect ratio can only be increased by decreasing the surface area of the wing. This will cause an increase in the wing loading, and decrease the volume of fuel that is able to be stored in the wing. Using this criteria the wing area was designed to be 853.879 ft^2, with an aspect ratio of 9.84. After computing the wing area, the lift coefficient of the wing can be calculated using the weight of the aircraft, and the force from the horizontal tail. Using these values the lift coefficient of the wing in mid-cruise is calculated to be $C_L = 0.469$.

The wing has a root chord length of 22.146 ft, and a taper ratio of 0.1 at the wingtip, and 0.145 at the hinge at which the wingtip will rotate around. These values were decided to allow for the use of thinner airfoil sections at the wingtip. The use of small taper ratios also has the benefit of reducing the weight of the wing, and lowering the overall structural load on the aircraft.

Increasing the sweep angle of the wing will yield better aerodynamic efficiency at the higher mach numbers required by reducing the wave drag on the wing. The sweep angle was set to 35° which will increase the range of the aircraft at high-speed cruise. This analysis is conducted in tandem with the selection of the thickness of the airfoils to best determine the effect of the sweep angle on the overall aerodynamic performance of the wing.

The other design constraint for sweep angle was that increasing sweep decreases the maximum lift coefficient in approach and takeoff. Since the effect of sweep angle at takeoff directly contradicts the effect at cruise, the angle that optimizes cruise performance is chosen to ensure fulfillment of the high speed, long range cruise requirements.

The dihedral angle of the wing was chosen to be 5° which provides good passive roll stability to the aircraft and mitigates roll effects of the low wing placement on the aircraft. If the dihedral angle is increased much more the aircraft will respond sluggishly in roll, and if the value is decreased a lot below 5° there could be more unnecessary rolling motions experienced during periods of turbulence.

The parameters chosen for the wing are tabulated below in Tab. 6. A top down view of the dimensioned wing is shown in Fig. 6.5.

Parameter	**Value [units]**
Span b_T	102.36 [ft]
Aspect ratio AR	9.84 [-]
Surface area S	853.879 [ft^2]
Taper ratio TR	0.1 [-]
Root chord c_r	22.146 [ft]
Tip chord c_t	2.215 [ft]
Mean aerodynamic chord $\overline{\overline{c}}$	12.139 [ft]
Quarter-Chord Sweep Angle $\Lambda_{c/4}$	35 [°]
Dihedral Angle Γ	5 [°]
Mid-Cruise Wing AOA α_{root}	2.75 [°]
Fuel Volume V_{fuel}	$3,945.034$ [Gallons]

Table 5: Values of Geometric parameters for the wing.

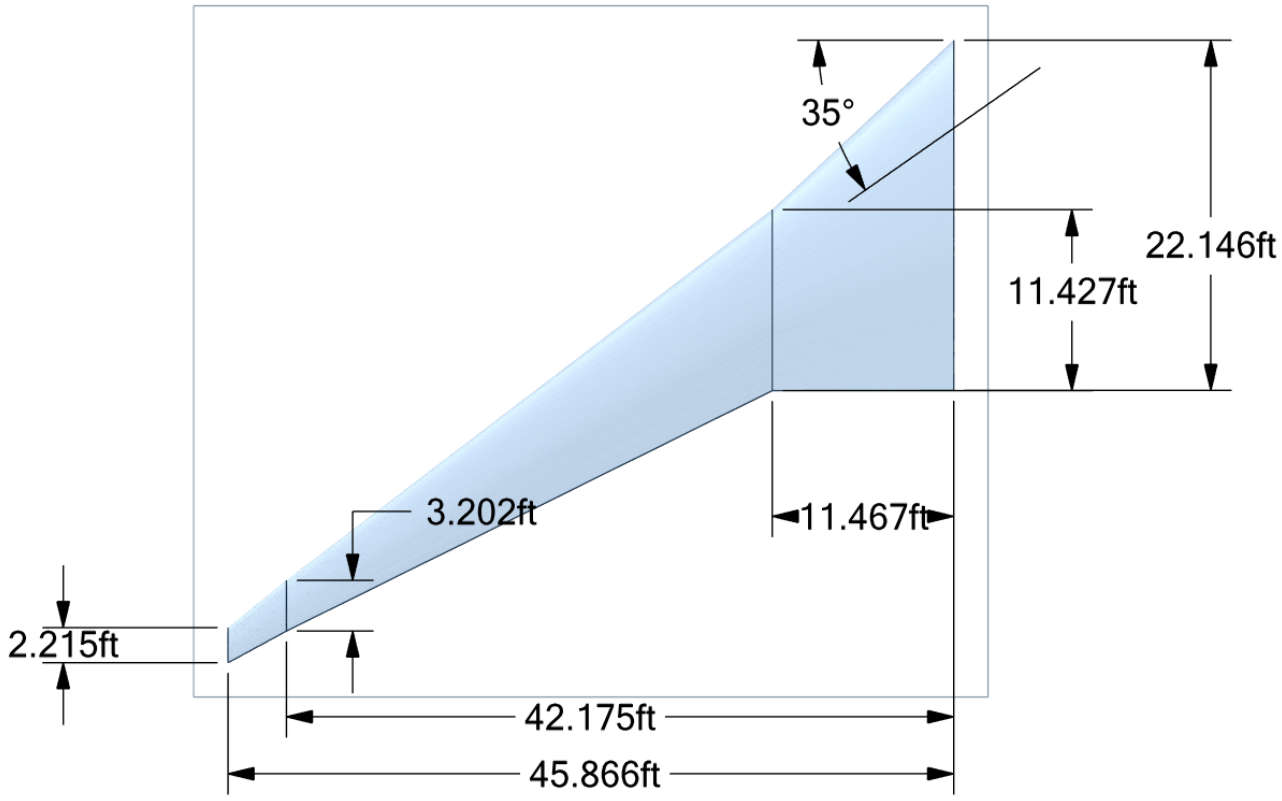

Figure 6.5: Top-Down Dimensioned View of Wing Design.

6.2.2 Airfoil Selection

Supercritical airfoils were chosen because they perform very well at transonic speeds compared to conventional airfoils. This allows for the aircraft to be more efficient at the high cruise mach number that is required. The root airfoil design criteria were that it needed to be symmetric, and it needed to be thick. The symmetric shape and thickness help with the attachment of the airfoil to the fuselage, while the thickness is mainly determined by the fuel storage needs of the aircraft, and the effect of thickness on drag at higher mach numbers. If the thickness is increased the airflow will see more local curvature and accelerate more over the top of the airfoil. This will increase the local mach number can lead to premature transonic flight, and increased wave drag. To mitigate transonic effects in high-speed cruise, the airfoil should be as thin as structurally possible to increase aerodynamic efficiency. However the volume of fuel needed for a long range flight will also need to be stored mostly in the wing, so the thickness of the airfoil will need to be sufficient to be able to hold this fuel.

Using both the required fuel volume, and the effects of thickness on the diverging mach number, the airfoil thickness values were selected to be 12% at the root, and 10% at the tip. This allows the wing to hold the calculated fuel volume while also minimizing excessive thickness in the tapered sections, where fuel storage is limited.

The airfoil for the wing tip was selected by analyzing transonic wings, and finding research that covers the effect of camber on the outboard airfoil. Research into NASA's Common Research Model (CRM) showed that it was best to have camber at the wingtip

[6]. This information allowed for the choice of airfoil at the tip to be made.

In the end the root airfoil was chosen as the NASA SC(2)-0012, which fulfills the 12% thickness and symmetrical requirements. While the wingtip airfoil was chosen to be the NASA SC(2)-0410, which is a more efficient 10% thickness airfoil that has camber that is closely matched to that found in the CRM [6].

To prevent the tip from being the part of the wing that stalls first, negative geometric twist is applied to the airfoil at the wingtip. The twist is set to 2° at the hinge point of the wingtip, and -2.5° at the wingtip itself. These values were chosen by analyzing the 2D airfoil Lift curve and shifting the angle of attack to ensure that stall first occurs away from the wingtip.

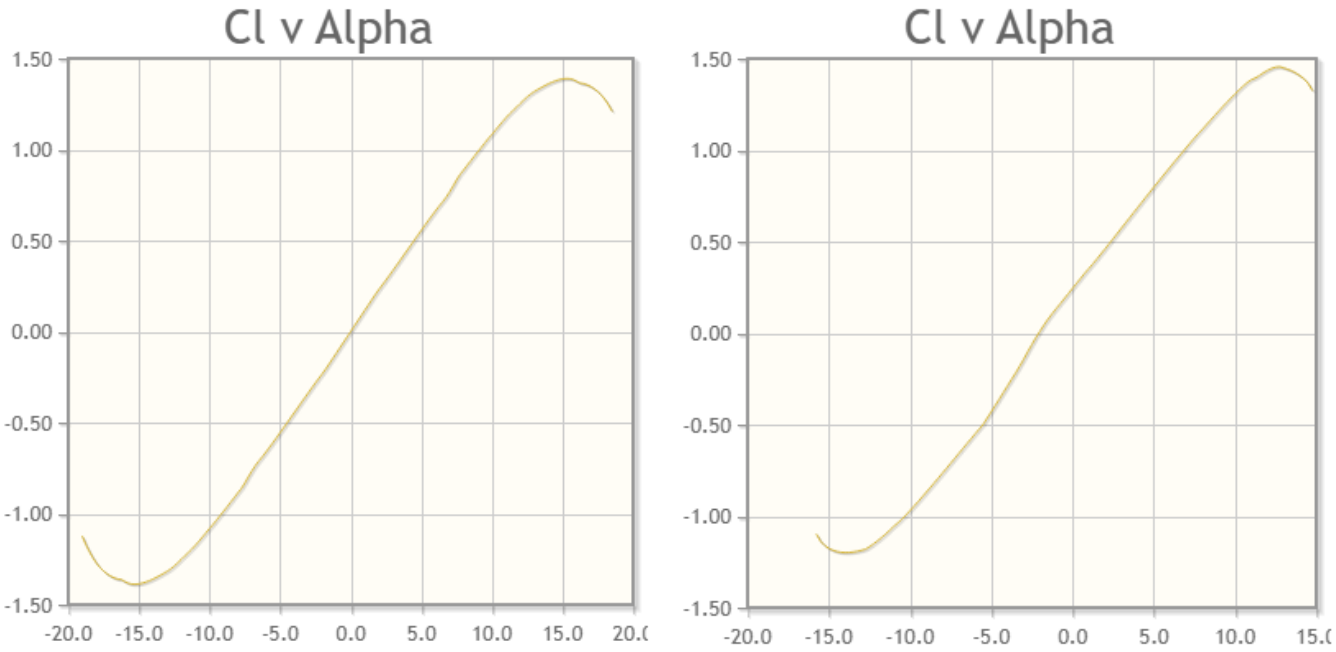

(a) NASA SC(2)-0012 Airfoil (Root).

(b) NASA SC(2)-0410 Airfoil (Tip).

Figure 6.6: Cl v Alpha Curves for Chosen Airfoils [23].

By twisting the wingtip downwards 2.5°, the 2D stall angle can be moved past the stall angle that is experienced inboard, which will ensure that the outboard section will not stall first.

6.2.3 Control Surfaces

The control surfaces on the wing were chosen to include both leading edge slats, and trailing edge flaps. This allows for greater lift augmentation compared to if only flaps were included in the design. This increased lift will facilitate the desired capability of short takeoff and landing.

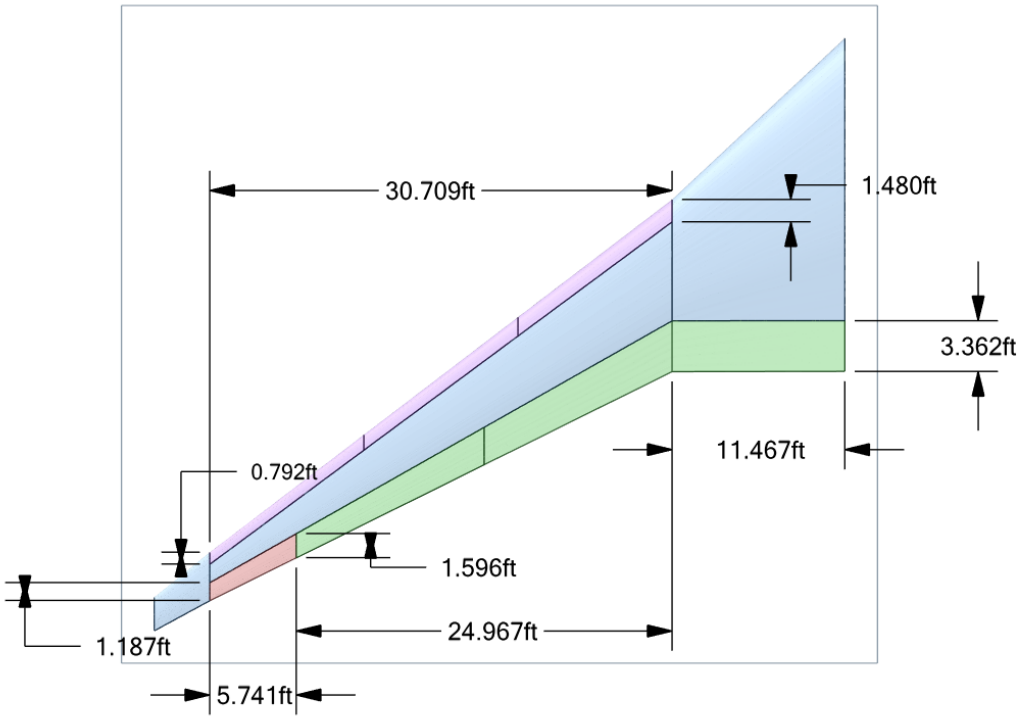

Figure 6.7: Top-Down Dimensioned View Of Wing Control Surfaces, purple = slats, green = flaps, red = ailerons.

Where the purple region represents the area dedicated to the slats at the leading edge of the wing, the green sections represent area dedicated to the flaps at the trailing edge of the wing, and the red section represents the outboard aileron. One important consideration made is that there will be no control surfaces added to the movable wingtip to reduce the complexity of the system.

Parameter	**Value [units]**
Flap Surface Area	201.460 [ft^2]
Aileron Surface Area	15.980 [ft^2]
Slat Surface Area	69.729 [ft^2]
Takeoff Flap Deflection Angle δ_{max}	20.0 [°]
Landing Flap Deflection Angle δ_{max}	50.0 [°]

Table 6: Values of Geometric parameters for Wing Control Surfaces.

6.2.4 Position of the Wing

The position of the wing was split into two different decisions. The location of the wing along the length of the fuselage, and the height at which the wing is attached on the fuselage. The height of the wing was chosen to be low-mounted due to the increased aerodynamic efficiency. The longitudinal position was decided using stability analysis while optimizing aircraft performance.

6.2.5 Design Considerations for Foldable Wingtip

To determine the feasibility of a foldable wingtip, the structure of the wingtip will need to be studied to ensure that the wingtip is unable to move mid-flight. To analyze this a foldable structure, and mechanism to rotate it would be designed. These components would then be tested using the aerodynamic loads computed at the hinge point. In addition to ensuring the wingtip is incapable of unfolding in mid-flight, the wing would also follow the proposed special conditions for the Boeing 777-9 folding wingtips from the EASA [1]. Following these conditions would ensure that the folding wingtip is safe to implement on the aircraft.

6.3 Empennage

6.3.1 Empennage Selection

A conventional tail configuration for business jet provides better longitudinal stability and is more efficient for cruise flight, which is the primary operating mode of a business jet. It also aligns with standard industry practices, simplifying certification and maintenance compared to a canard configuration. Given these factors, the choice of a conventional tail was the most logical and optimized solution.

There are multiple types of tail configurations, each with its own advantages. The chosen one for this business jet is the T-tail, and here are the reasons behind this choice. The T-tail keeps the stabilizers out of the engine wake, improving pitch control and aerodynamic efficiency at high speeds. It also optimizes airflow by placing the horizontal stabilizer away from the wake generated by the wings, reducing interference and enhancing longitudinal stability. Additionally, this configuration provides structural simplicity and stiffness, key factors for high-performance aircraft. Another benefit is that the elevated position of the horizontal stabilizer helps prevent damage to control surfaces during takeoff and landing, an important consideration for business jets operating from various types of runways. While a cruciform tail could be considered to mitigate deep stall risks associated with T-tail designs, the aerodynamic and operational advantages of a T-tail make it the optimal choice for this aircraft.

6.3.2 Airfoil Selection

The selection of the empennage airfoil is crucial for ensuring stability, aerodynamic efficiency, and structural integrity. The NACA 0012 was chosen based on the following considerations:

The symmetrical airfoil selected for the OPULOX-1 offers significant advantages in terms of simplicity and cost-effectiveness. Its geometry greatly facilitates manufacturing processes, thereby reducing production costs. The absence of complex curvature allows for a standardized design, simplifying fabrication and improving production efficiency.

From an aerodynamic standpoint, the profile demonstrates high efficiency. Its low thickness of 12% minimizes drag, which is critical for achieving high-speed cruise at Mach 0.85. Additionally, the streamlined shape optimizes lift without compromising aircraft stability.

The stall characteristics of the airfoil have also been carefully considered. Its progressive stall behavior enhances predictability and provides better control for the pilot. Furthermore, the tailplane stalls after the wing, ensuring improved maneuverability under critical flight conditions.

Structurally, the thin profile contributes to overall weight reduction while maintaining sufficient rigidity. The balanced combination of flexibility and strength plays a crucial role in preventing flutter at high speeds, supporting safe and efficient operation during cruise and maneuvering phases.

6.3.3 Geometry Design

All geometry aspects such as the area of the different stabilizers, their respective span, and more are calculated by first computing the translational equilibrium in the direction normal to the earth and a rotational equilibrium along the axis which drives the pitching moment. This equilibrium takes into account the lifts generated by the wing and the horizontal stabilizer, the weight of the aircraft and the drag generated by the tail since this part of the drag is not compensated by its symmetric counterpart, as is the case for engines for a rotational equilibrium around the yaw moment axis, for example. It has a non-negligible contribution to the moment equilibrium due to the large leader arm between the center of gravity and the point of application of the drag. The tail design was carried out using a sizing approach based on tail volume coefficients proposed by Gudmundsson [20], ensuring a balanced relationship between the lifting surfaces and the tail assemblies. The initial results from this method were then refined and validated through comparisons with data from existing business jets of similar configuration.

The geometric parameters are then calculated and presented below in Tab.7 and 8, respectively, for the horizontal and vertical stabilizers. These parameters allow to construct the tail presented in Fig. 6.8 and 6.9

Parameter	Value [units]
Selected airfoil	NACA 0012
Span b_T	26.247 [ft]
Aspect ratio AR_T	4.5 [-]
Surface area S_T	153.087 [ft^2]
Taper ratio TR_T	0.4 [-]
Root chord $c_{r,T}$	8.332 [ft]
Tip chord $c_{r,T}$	3.333 [ft]
Standard mean chord $\bar{c}_T$	5.833 [ft]
Mean aerodynamic chord $\overline{\overline{c_T}}$	6.190 [ft]
Distance from wing to tail	46.249 [ft]
Leading edge swept angle $\Lambda_{LE,T}$	35 [°]
Trailing edge swept angle $\Lambda_{TE,T}$	17.706 [°]
Distance from aircraft nose to horizontal stabilizer root leading edge	100.880 [ft]

Table 7: Values Of Geometric Parameters For Horizontal stabilizer.

Parameter	Value [units]
Selected airfoil	NACA 0012
Span b_F	15.584 [ft]
Aspect ratio AR_F	1.063 [-]
Surface area S_F	228.518 [ft^2]
Taper ratio TR_F	0.7 [-]
Root chord $c_{r,F}$	17.251 [ft]
Tip chord $c_{r,F}$	12.076 [ft]
CD_F	0.025 [-]
Standard mean chord $\bar{c}_F$	14.664 [ft]
Leading edge swept angle $\Lambda_{LE,F}$	47 [°]
Trailing edge swept angle $\Lambda_{TE,F}$	36.511 [°]
Distance from aircraft nose to vertical stabilizer root leading edge	84.170 [ft]

Table 8: Values Of Geometric Parameters For Vertical stabilizer.

There are also other parameters that can be calculated that are function of time since fuel is burn during the flight. These parameters are presented in Tab. 9 for the start and the end of the cruise since those are the limit values.

Parameter	Start of cruise	End of cruise
Tail moment arm l_T	52.102 [ft]	49.5725 [ft]
Angle of incidence i_T	-0.041 [°]	2.116 [°]
CL_T	-0.00257 [-]	0.132 [-]
CD_T	0.0250 [-]	0.0264 [-]
Fin moment arm l_F	8.852 [ft]	8.918 [ft]

Table 9: Time Dependant Parameters.

The tail incidence angle i_t is set to balance the overall pitching moment. This was achieved using a recursive code refreshing the drags and lifts values as well as the tail incidence angle. The main contributors to the pitching moment are the moment from the horizontal stabilizer's lift, the moment from the wing's lift, and the moment from the horizontal and vertical stabilizer's drag.

6.3.4 Control Surfaces

The T-tail configuration, where the horizontal stabilizer is mounted on top of the vertical stabilizer, offers advantages such as reduced interference with the main wing wake and improved pitch authority. However, it also introduces challenges related to control effectiveness, stability in deep stall conditions, and structural loads. In deep stall conditions, control effectiveness is compromised due to the loss of control authority, increased control forces, and aerodynamic interference, making the aircraft harder to control. Stability is challenged by longitudinal instability, unpredictable recovery behavior, and hysteresis, complicating stall recovery. Structural loads are increased by high load factors, unsteady aerodynamic forces, and the risk of flutter or divergence, which can put excessive strain on the aircraft's structure and potentially lead to damage. These challenges require careful design to ensure safe and effective aircraft performance.

The selected control surfaces for this T-tail business jet are: elevators and trim tabs on the horizontal stabilizer and Rudder and trim tabs on the vertical stabilizer. The elevators provide pitch control, counteracting pitching moments and ensuring smooth handling. Trim tabs reduce pilot workload and enhance stability by allowing fine pitch adjustments without continuous control input.

The rudder controls yaw and provides directional stability, optimized for high-speed efficiency and effective control during cross-wind landings and engine-out scenarios. Trim tabs help reduce yaw control forces and counteract asymmetric thrust effects.

These surfaces ensure effective longitudinal and directional control, balancing stability with maneuverability. Parameters are taken from Aircraft Design: A System Engineering Approach [27] and presented in Tab. 10. The parameters are illustrated in Fig. 6.8 and 6.9.

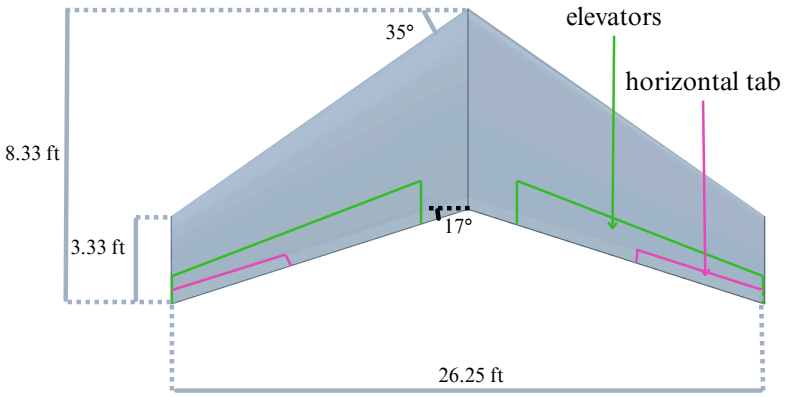

Figure 6.8: Representation Of Horizontal Stabilizer Control Surfaces.

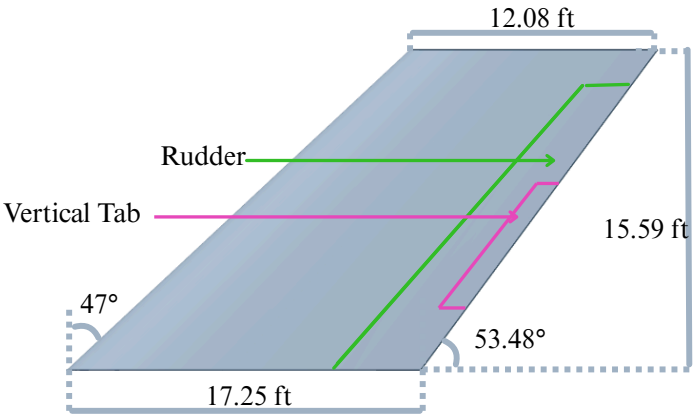

Figure 6.9: Representation Of Vertical Stabilizer Control Surfaces.

Control Surface	Elevator	Rudder	Trim Tab
Control surface area	$S_E/S_H \in [0.15\text{–}0.4]$	$S_R/S_V \in [0.15\text{–}0.35]$	$S_T/S_E \in [0.05 - 0.15]$, $S_T/S_R \in [0.1 - 0.2]$
Lifting surface area	$S_E/S_H = 0.3$	$S_R/S_V = 0.2$	$S_T/S_E = 0.1$, $S_T/S_R = 0.12$
Control surface span	$b_E/b_H \in [0.8\text{–}1]$	$b_R/b_V \in [0.7\text{–}1]$	$b_T/b_{E,R} \in [0.25 - 0.5]$
Lifting surface span	$b_E/b_H = 1$	$b_R/b_V = 0.85$	$b_T/b_E = 0.4$, $b_T/b_R = 0.45$
Control surface chord	$C_E/C_H \in [0.2\text{–}0.4]$	$C_R/C_V \in [0.15\text{–}0.4]$	$C_T/C_{E,R} \in [0.15 - 0.3]$
Lifting surface chord	$C_E/C_H = 0.3$	$C_R/C_V = 0.235$	$C_T/C_E = 0.25$, $C_T/C_R = 0.267$
Control surface max deflection (negative)	$\delta_E = -25°$ (up)	$\delta_R = -30°$ (right)	$\delta_T = -25°$ (up), $-30°$ (right)
Control surface max deflection (positive)	$\delta_E = +20°$ (down)	$\delta_R = +30°$ (left)	$\delta_T = +20°$ (down), $+30°$ (left)

Table 10: Control Surface Parameters For A T-Tail Business Jet. The indices H, V, E, R, T refer to horizontal stabilizer, vertical stabilizer, elevator, rudder, and trim tab, respectively.

6.4 Propulsion

The propulsion-related analysis presented in this section are developed in coherence with the aerodynamic characteristics of the aircraft. In particular, drag estimations used for performance and sizing purposes are based on the results of the drag study detailed later in the report in section 7.4. This forward reference ensures consistency between propulsion requirements and the actual aerodynamic behavior of the OPULOX-1.

6.4.1 Engine selection

By looking at the different types of engine and their efficiency at various velocities, it is possible to choose the type of engine that is the most suitable for purpose of the business jet.

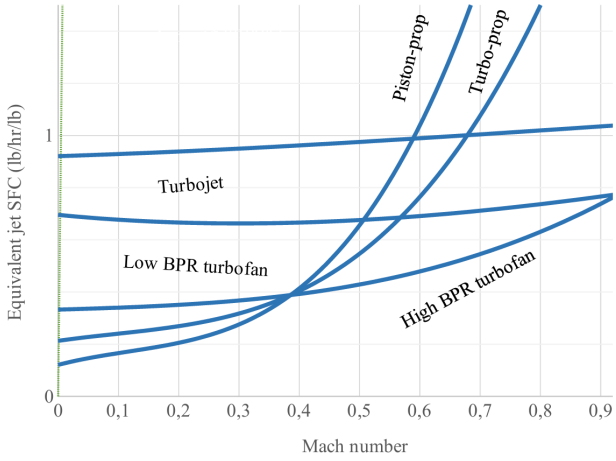

(a) Specific fuel consumption trends at typical cruise altitudes for different propulsion systems, data retrieved from [25].

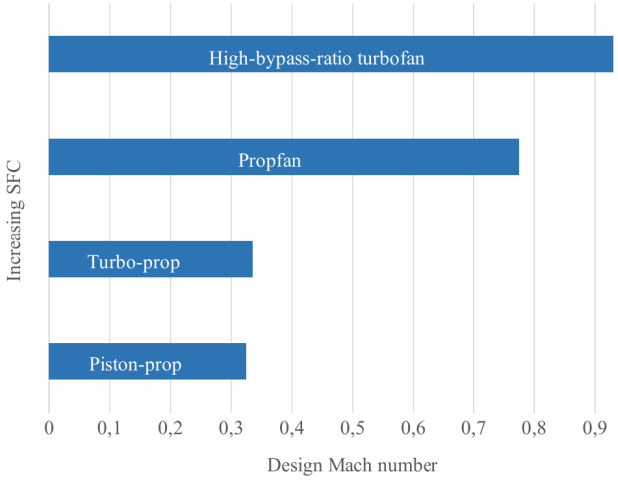

(b) Propulsion system designed speeds, data retrieved from [25].

Figure 6.10: Types of propulsion system comparison.

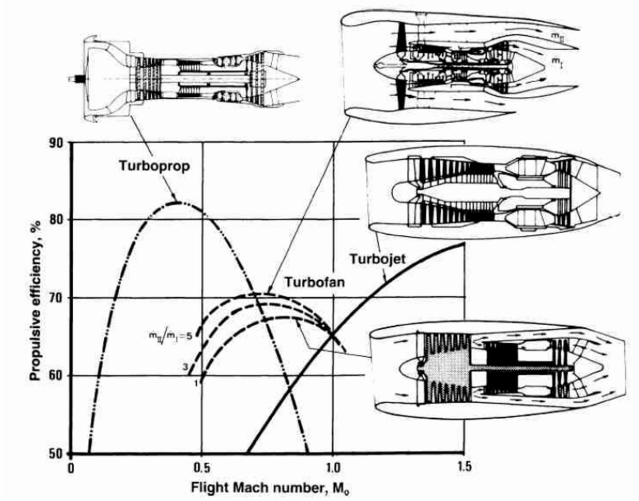

Figure 6.11: Different engine types comparison, diagram originates from Koen Hillewaert's course on propulsion [21].

Upon analyzing these graphs, it becomes evident that a turbofan propulsion system is the most suitable choice for this project. Turbofan engines are specifically designed to operate efficiently across a wide range of speeds and altitudes, which aligns well with the typical flight profile of a business jet.

A comprehensive review of turbofan engines currently available on the market for business jets similar to OPULOX-1 was conducted, and several potential options were identified for further evaluation. Additionally, the ambition to differentiate OPULOX-1 design from existing solutions has driven an exploration of various sizes and types of turbofan engines, with some very various bypass ratio and thrust values.

Tab.11 presents the primary engine candidates considered for selection. By comparing their key characteristics, they have been ranked based on our specific requirements. Given that the designed aircraft is a business jet, engine dimensions play a crucial role, as they must remain relatively compact compared to those used in commercial aviation. As previously shown, the 2 engines will be mounted on the rear fuselage, necessitating a weight that remains within structural limits to avoid excessive stresses that could compromise the aircraft's integrity.

Specific fuel consumption (SFC) is also one of the critical factors in the engine selection process. This parameter, along with other key performance criteria, have been carefully evaluated in the following table to determine the optimal engine for the OPULOX-1.

Engine	Static SL Thrust [lbf]	Dry Mass [lbs]	TSFC [lbs/lbf/hr]	BPR	Length [in]	Diameter [in]
PW 815GA	16,011	3,135	0.624	5.5	105.8	50
Rolls-Royce BR725	16,900	3,605	0.657	4.2	130	50
PW 1700G	17,000	3,800	0.56	50	113.5	62
CF34-10	18,500	3,760	0.64	5.4	115	53
GE Passport	18,920	3,950	0.5225	5.6	102.7	52
LEAP 1B-27	27,220	6,130	0.54	9	124	69.4

Table 11: Engine characteristics comparison.

To enhance the takeoff performance of OPULOX-1, it is essential to select an engine with a higher thrust capacity. For this reason, the GE Passport engine has been chosen, represented in Fig.6.12.

While its thrust output exceeds the minimum required to meet performance criteria, it aligns perfectly with the short takeoff configuration envisioned for the aircraft.

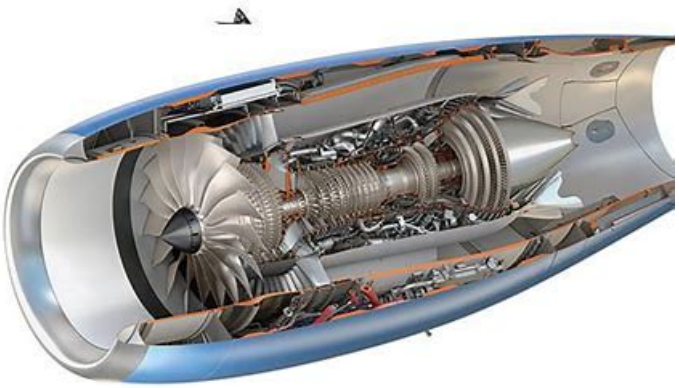

Figure 6.12: GE Passport.

The variation of the maximum available thrust as a function of the altitude and the Mach number is unknown during the preliminary design study. The latter is thus approximated for different Mach numbers in the range of Mach that will be encountered during cruise by using the following approximated model from [22]. A slight increase in thrust is seen due to increasing compressibility effects at these transonic velocities. The decrease in thrust with altitude is a consequence of the decrease of density in the air.

$$T = T_{SL,\max} \cdot \left(\frac{\rho}{\rho_{SL}}\right) \cdot (1 + 0.05M) \tag{6.1}$$

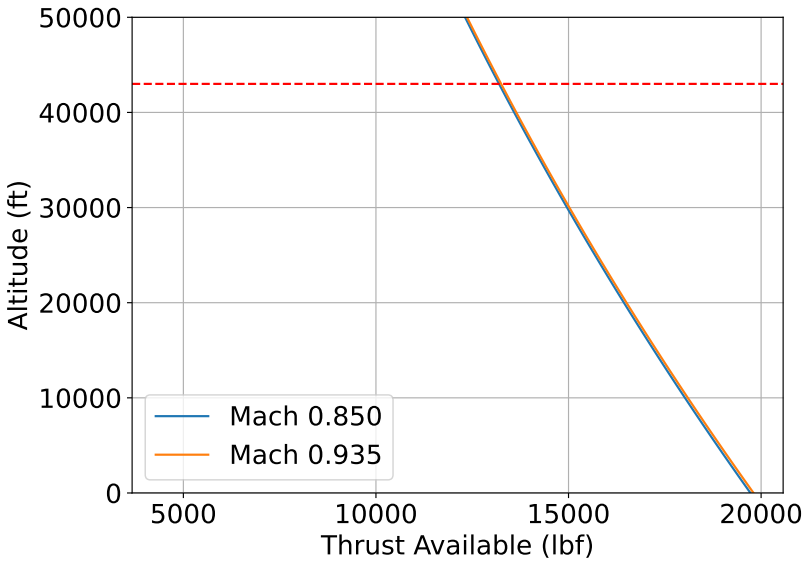

Figure 6.13: Maximum thrust available as a function of the flight altitude and velocity.

When plotting the evolution of the max available thrust using this equation Eq. 6.1, it comes that the available thrust at 43,000 ft cruise altitude and Mach 0.85 cruise speed is 13,610 lbf which is large enough to balance the cruise drag forces acting on the aircraft at such velocity and altitude.

6.4.2 Fuel analysis

The total amount of fuel to carry on for each mission is summarized in the table below, considering a Mach 0.85 cruise velocity for the longest mission and a Mach 0.935 cruise velocity for the shorter missions. The calculations are done using Breguet Range equation in section 8, and taking into account the different values of lift-to-drag ratio, and different SFC values, depending on the flight speed. The fuel weight are indicated with the fuel reserves already taken into account.

Mission	Range [NM]	Cruise Mach [-]	Fuel weight [lbs]
Design Passenger Mission	8,000	0.85	45,068
Aspen Economic Mission	643.4	0.935	7,596
Napa Economic Mission	1,680	0.935	12,150

Table 12: Fuel needs for requested missions.

In this section, the question of fuel storage within the aircraft is explained.

The distribution of the total fuel weight inside the aircraft results of the process of considering the volume available inside the wing, which is filled with fuel. If needed, the remaining mass of fuel is stored inside the fuselage. The computation of the available volume for fuel tank in the wings takes into account the geometry of the wing and calculates that the wings can store 3,945 US gallons.

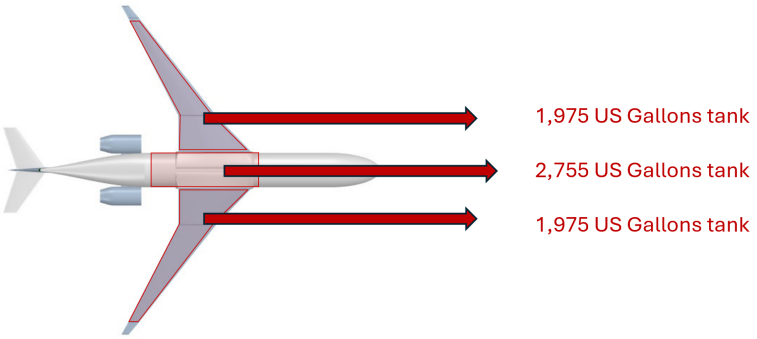

Figure 6.14: Fuel repartition within the aircraft.

The density of kerosene is obtained through documentation $\rho_{\text{kerosene}} = 6.8$ lbs·US Gallons^{-1} [32]. Then, the total mass of kerosene that can be put in the wings is 26,826 lbs. This means that the tanks located in the wings are not sufficient for the Design Passenger mission, which means that an additional tank in the fuselage is needed. To store the additional 18,728.5 lbs of fuel needed for this ultra-long range mission, a 2,755 US gallons tank is placed within the fuselage. A schematic of the fuel distribution in the aircraft is represented in Fig.6.14 .

6.5 Landing Gear

6.5.1 Landing Gear Type

First, designing a landing gear, the type must be determined. A tricycle landing gear was chosen. This configuration, enhances stability on the ground during taxiing, as the center of gravity is ahead of the main gear. It allows one to have a horizontal cabin floor when the airplane is on the ground. Finally, visibility is greater for the pilot using this type of landing gear.

6.5.2 Position

The longitudinal position of both nose and main landing gear are determined fixing that the nose landing gear must support 10% of the total weight and main landing gear must support 90%. The wheelbase is also deduced as it is defined as the distance between nose and main landing gears.

The height should be large enough to achieve a 9 inches clearance of the propellers. These are located high enough so that this requirement is immediately achieved. Secondly, the tip-back angle must be considered. The height of the landing gear must be such that the tail of the airplane does not touch the ground during landing. The landing angle is such that 90 % of the maximum lift is generated. The corresponding angle is usually between $10°$ and $15°$. To prevent the aircraft from tipping back on its tail, the configuration should ensure that the angle between the center of gravity and the main wheel position is greater than $15°$ (tip-back angle) but less than $25°$, otherwise, porpoising may occur. Additionally, the height should be such that the wing is 6 inches from touching the ground during a $5°$ roll. Overturn angle measures the aircraft's tendency to overturn when turning sharply. This angle should not be greater than $63°$ and was therefore fixed at $63°$.

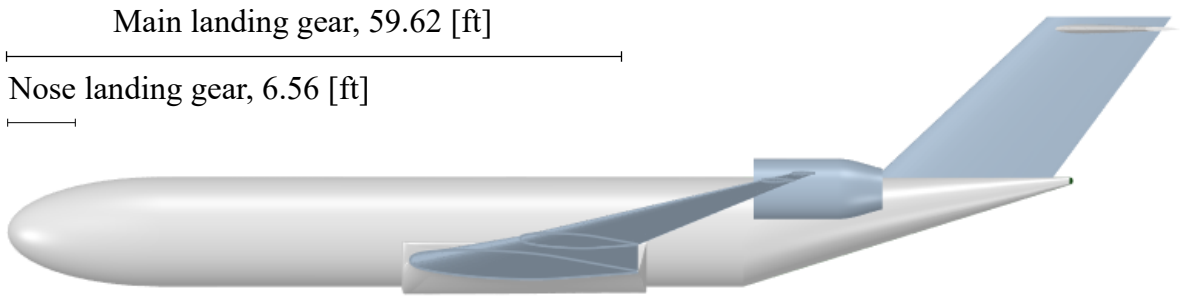

Figure 6.15: Landing gear location representation.

All the characteristics of both main and nose landing gear are written in Tab. 13.

Distance from nose to nose landing gear [ft]	6.56
Wheel base [ft]	53.06
Wheel track [ft]	7.81
Weight on each main landing gear wheel [lbs]	23,381.1
Weight on nose landing gear wheel [lbs]	5,195.8
Overturn angle [°]	63
Height of main landing gear [ft]	3.48
Height of nose landing gear [ft]	4.02
Tail strike angle [°]	15

Table 13: Geometrical parameters of the landing gear.

6.5.3 Tire Design

For added stability, each bogie is equipped with two tires, resulting in a total of four tires for the main landing gear, and two tires for the nose landing gear. It is assumed that the weight is evenly distributed among all tires within their respective landing gear systems. For security reasons, an additional weight corresponding to 20 % of the supported weight is added.

	Main Landing Gear	**Nose Landing Gear**
Tire Size	40×14	$9.50 - 16$
Maximum Static Load [lbs]	33,500	9,250
Maximum Width [in]	14	9.7
Maximum Diameter [in]	39.80	33.35

Table 14: Tires specifications.

6.5.4 Brakes Design

As the aircraft must be capable of quick landings, the brake design is very important. The braking force is computed on the basis of the following formula:

$$F_{\text{brakes}} = m\frac{v_{\text{landing}}^2}{2d} - C_{\text{rolling resistance}} \cdot m - \frac{C_{\text{d, landing}} \cdot \rho \cdot v^2 \cdot S}{2} \tag{6.2}$$

Applying this equation the required brake force per wheel is 3,824 lbf. As the required braking force per wheel is large, the best braking system is a multiple disk brake system. The principle is that kinetic energy is transformed into thermal energy. Carbon fiber has improved heat dissipation performance and also requires less maintenance than steel. The braking system is thus a multiple disk system build in carbon fiber.

7 Aircraft analysis

7.1 Weight and center of gravity

The weight of the aircraft is computed using estimated component weights. These component weights are computed using correlations from the book Aircraft Design: Synthesis and Analysis [14]. To calculate the fuel quantity needed for the mission requiring the longest range (8,000 nm), Breguet Range equation has been used to determine the fuel weight.

Component	**Mass [lbs]**	**Position x [ft]**
Wing with ailerons	4,650	53.02
Horizontal empennage and elevators	1,290	106.07
Fin without rudder	1,048	92.60
Rudder	422	94.10
Fuselage	11,034	46.37
Landing gear front	198	6.56
Landing gear rear	2,295	59.62
Electro-mechanical system of control surfaces	1,264	53.02
Engines	12,640	70.08
APU	70	10.30
Instruments	1,200	4.81
Water stock	643	1.03
Electrical	130	46.37
Electronics	1,500	70.08
Furnishing	1,123	51.53
AC and deicing	150	16.05
Operating items	320	56.87
Flight crew	430	19.33
Flight attendant	195	56.87
Passengers with luggage	2,520	56.87
Fuel	45,068	56.43
Zero Fuel Weight and $x_{CG,ZFW}$	46, 169	56.68
Maximum takeoff Weight and $x_{CG,MTOW}$	91, 238	54.73

Table 15: Masses and longitudinal locations of the different aircraft components.

All detailed weight information is provided in Tab. 15, which also includes the longitudinal positions relative to the aircraft's nose, denoted as Position x.

7.2 Stability

This section contains the static and dynamic stability computations for the OPULOX-1 business jet.

7.2.1 Static stability

Evaluation Of The Aerodynamic Center

The aerodynamic center is computed as a function of the Mach number, sweep, and aspect ratio, according to the graph from Conceptual Design [24]. The aerodynamic centers in cruise at Mach 0.85 are located at 41% the mean aerodynamic chord for the wing and at 32% of the mean aerodynamic chord for the horizontal stabilizer. Their positions moves forward as Mach increases. At the beginning of the cruise, the aerodynamic center is at 53.03 ft, reaching 54.36 ft at the maximum Mach for the wing. For the horizontal stabilizer the difference is smaller and a constant value of 106.7 ft is used.

Longitudinal stability

The longitudinal stability corresponds to pitch stability. The following condition on the derivative of the pitching moment around the rotation point C_m with respect to the lift coefficient must be satisfied.

$$\frac{\partial C_m}{\partial C_L} < 0. \tag{7.1}$$

The static margin can be introduced to evaluate the previous derivative. It takes into account the contributions of the wing, fuselage, and tail.

$$\mathrm{K}_n = h_n - \frac{h}{\bar{\bar{c}}} = \frac{h_0}{\bar{\bar{c}}} + \bar{V}_t \frac{a}{a_1}\left(1 - \frac{d\epsilon}{d\alpha}\right) - \frac{\partial C_{\mathrm{m,fus}}}{\partial C_{\mathrm{L,wing}}} - \frac{h}{\bar{\bar{c}}} > 0. \tag{7.2}$$

With the neutral point h_n, the center of gravity position h, the aerodynamic center position h_0, tail volume coefficient $\bar{V}_t$, the mean aero chord $\bar{\bar{c}}$ and the downwash ratio $\frac{d\epsilon}{d\alpha}$. The fuselage contribution $\frac{\partial C_{\mathrm{m,fus}}}{\partial C_{\mathrm{L,wing}}}$ is computed using the Gilruth correlation [14]. This static margin needs to be greater than 5% to ensure safety and lower than 35% to stay maneuverable in cruise. Extreme situations must be analyzed to ensure stability throughout the entire cruise. The first is lowest velocity in case of landing with only the reserve of fuel remaining. And the second is during cruise flight with all the passengers positioned at the top of the fuselage with the fuel tanks fully loaded.

Situations	h_0 [ft]	h [ft]	K_n [%]
MTOW takeoff with passengers	53.03	55.41	13.42
ZFW landing with passengers	53.03	56.22	6.49
Starting cruise, all passengers in the kitchen	54.36	54.49	32.5
End cruise, passengers in the bathroom	54.36	56.81	11.37

Table 16: Evolution of aerodynamic center, center of gravity and the static margin throughout the cruise.

These situations are presented here below on Tab.16, the static margin is between 6.49% and 32.50% . In Fig.7.1, the cases of landing and take off are considered separately from cruise due to the different positions of the aerodynamic centers. The Fig.7.1 represents the evolution of the center of gravity of the actual plane in black and the allowed positions in color. This figure highlights that the static margin is smaller for the take off and landing, meaning that the plane is more maneuverable in these situations than during cruise. It is ideal for OPULOX-1 that want to have short runway distances for operations.

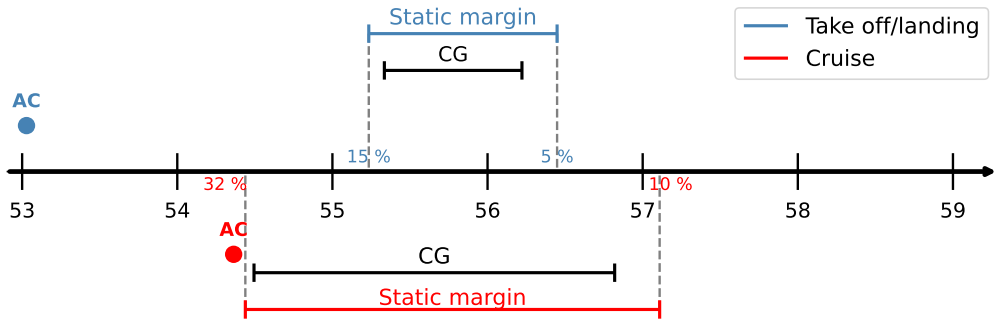

Figure 7.1: Evolution of the center of gravity and representation of acceptable position of the center of gravity.

Lateral stability

The lateral stability correspond to the stability in yall motion, and following Conceptual design course [24] the stability is satisfied if:

$$\frac{\partial C_N}{\partial \beta} = C_{N\beta} > 0. \tag{7.3}$$

With $C_{N\beta} = C_{N\beta,\mathrm{f}} + C_{N\beta,\mathrm{w}} + C_{N\beta,\mathrm{t}}$ the contribution of the fuselage, wing and vertical tail. This condition must be verified throughout the entire cruise. The fuselage contribution is computed with the method of the Aircraft Design book [33] and is $C_{N\beta,\mathrm{f}} = -0.17$, the fuselage is destabilizing . The wing are low-mounted so their value is fixed at $C_{N\beta,\mathrm{w}} = 0.024$. Finally,

the vertical tail (the fin) is designed to ensure the yaw stability and $C_{N\beta,\text{t}} = C_{L\beta,\text{fin}} \frac{S_\text{F} L_\text{F}}{Sb} = 0.17$ is obtained. The total one is $C_{N\beta} = 0.024$ so stability is verified.

Evaluation Of Derivatives

The evolution of the derivative of the lift coefficient with the angle of attack for the wing and the tail is computed by taking in account, the sweep, the Mach number, the aspect ratio and the 2D lift coefficient. This coefficient depends on the airfoil, for the wing based on sweep for a transonic regime $c_{l\alpha,2d} = 9.549$ rad^{-1}. Using the formula of derivative of the C_L for 3D wing from [24], the derivatives of the lift coefficient for the wing and tail are respectively $a = 5.079$ rad^{-1} and $a_1 = 4.664$ rad^{-1}.

7.2.2 Dynamic stability

The methodology used to assess the stability and control derivatives is based on the empirical correlations found in the US Air Force Stability and Control Data Compendium (USAF DATCOM). This method gives good approximations for preliminary design. A key point to mention is that this method was developed for conventional subsonic aircraft and as OPULOX-1 is a business jet that flies at transonic speeds, the results must be carefully analyzed. This method has been described by Finck [17] and Roskam [26].

Derivatives	**USAF DATCOM [/rad]**
C_{L_α}	7.807
C_{D_α}	0.253
C_{M_α}	-1.675
C_{L_u}	1.650
C_{D_u}	0.069
C_{M_u}	0
C_{L_q}	12.689
C_{D_q}	0
C_{M_q}	-28.919
$C_{L_{\dot\alpha}}$	1.872
$C_{D_{\dot\alpha}}$	0
$C_{M_{\dot\alpha}}$	-7.716
C_{L_η}	0.075
C_{D_η}	0
C_{M_η}	-0.312

(a) Longitudinal stability derivatives.

Derivatives	**USAF DATCOM [/rad]**
C_{Y_β}	-4.775
C_{l_β}	-0.248
C_{n_β}	0.1139
C_{Y_p}	-0.097
C_{l_p}	-0.536
C_{n_p}	-0.044
C_{Y_r}	0.603
C_{l_r}	0.254
C_{n_r}	-0.094
C_{Y_ξ}	0
C_{l_ξ}	0.419
C_{n_ξ}	-0.151
C_{Y_ζ}	0.278
C_{l_ζ}	0.005
C_{n_ζ}	-0.033

(b) Lateral stability derivatives.

Table 17: Stability and control derivatives of the OPULOX-1.

The stability derivatives for both longitudinal and lateral cases are listed in Tab.17. The equilibrium configuration under consid-

eration is the mid-cruise flight condition.

The state-space form of the equations of motion can then be constructed using these derivatives and separated into the longitudinal and the lateral contributions. It is written as

$$\mathbf{x}(t) = \mathbf{A}\,\mathbf{x}(t) + \mathbf{B}\,\mathbf{u}(t), \quad \text{where} \quad \mathbf{x} = [u, v, w, p, q, r, \theta, \phi, \psi]^T, \quad \mathbf{u} = [\eta, \xi, \zeta]^T$$

The eigenvalues of the **A** matrix are listed in Tab. 18 for both cases.

Longitudinal	**Lateral**
$-3.133 + 2.031j$	-5.25
$-3.133 - 2.031j$	$-0.255 + 1.169j$
$-0.00195 + 0.058j$	$-0.255 - 1.169j$
$-0.00195 - 0.058j$	0.0389
	0

Table 18: Eigenvalues for longitudinal and lateral equations of motion.

Longitudinal modes and flying qualities

The longitudinal eigenvalues consist of two complex conjugate pairs with negative real parts, which indicates that the aircraft's longitudinal dynamics are stable. These pairs correspond to the two classical longitudinal motion modes: the short-period oscillation and the phugoid. The associated natural frequencies and damping ratios are presented in Tab.19. The frequency is given by the magnitude of the complex eigenvalue, while the damping ratio is calculated as the absolute value of the real part divided by the magnitude.

	Frequency ω [rad/s]	**Damping ratio ζ [-]**
Short period	3.7345	0.8391
Phugoid	0.0584	0.0331

Table 19: Longitudinal modes characteristics.

These values can be compared with the American Military Specification MIL-F8785C [13], as summarized by Cook [10]. OPULOX-1 is Level 1 in short period which means "flying qualities clearly adequate for the mission flight phase". It is Level 2 in phugoid, denoting "flying qualities adequate to accomplish the mission flight phase but with an increase in pilot workload"[10].

Lateral modes and flying qualities

The lateral modes consist of three modes: roll subsidence, Dutch roll, and spiral mode. Dutch roll is characterized by a complex conjugate pair with a negative real part, indicating stability. Both roll subsidence and Dutch roll are non-oscillatory modes with

specific time constants. However, the spiral mode is unstable, as indicated by the positive eigenvalue. But as it is very slow (time to double > 20 seconds), meaning pilots or autopilot systems can easily correct it. Furthermore, certification authorities (like FAA [15]) allow mild spiral instability as long as it doesn't require excessive pilot workload. Tab.20 lists the frequency, damping ratio, and time constant of these lateral modes, with the time constant being the inverse of the magnitude of the eigenvalue.

	Frequency ω [rad/s]	**Damping ratio ζ [-]**	**Time constant τ [s]**
Dutch roll	1.1964	0.2135	-
Roll subsidence	-	-	0.1905
Spiral	-	-	25.7165

Table 20: Lateral modes characteristics.

These results all align with the Level 1 flying qualities.

7.2.3 Sensitivity Analysis

By slightly varying all the non-dimensional stability derivative coefficients, we can assess whether the aircraft remains stable. Each of these coefficients is varied from -25% to +25% of their initial value, and the resulting outcomes are presented below:

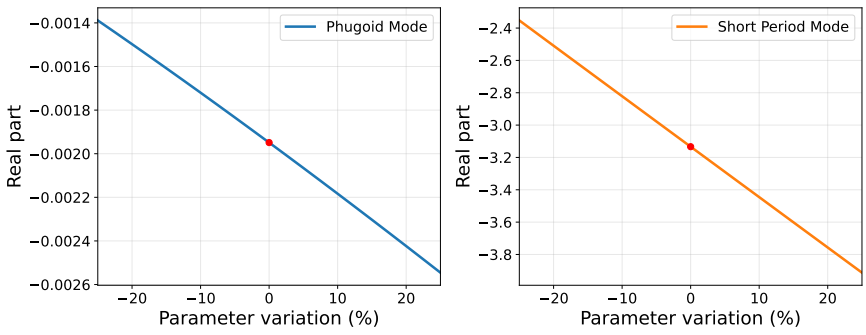

Figure 7.2: Variation of the real part of the longitudinal modes as the parameters change from -25% to +25% of their initial value.

As observed, even with changes in the parameters ranging from -25% to +25% of their initial values, all modes remain stable, as their eigenvalues have negative real parts. The only exception is the spiral mode, which remains unstable, but this does not lead to any significant consequences, as previously explained.

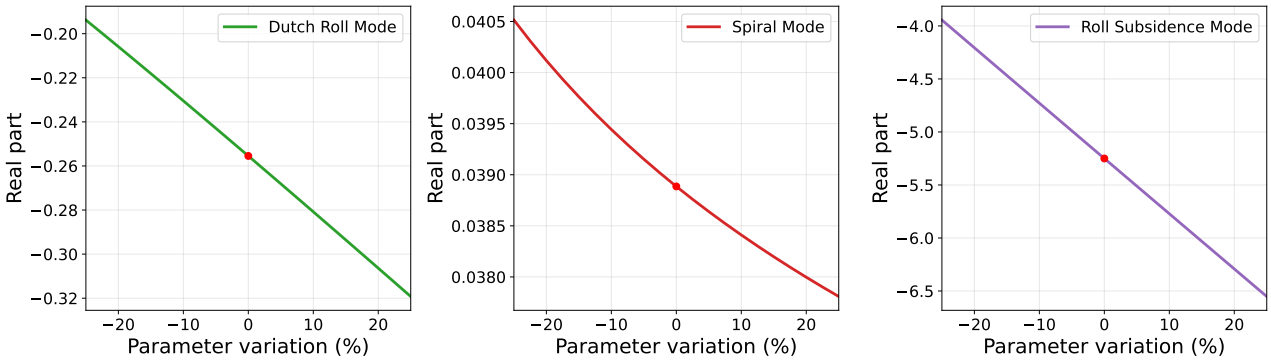

Figure 7.3: Variation of the real part of the lateral modes as the parameters change from -25% to +25% of their initial value.

7.3 Wing Aerodynamic Analysis

7.3.1 Performance Evaluation Method

The aerodynamic performance of the wing was evaluated using DARTFlo, an open-source full potential solver which is capable of solving steady transonic flows [11]. To ensure the accuracy of the simulation a mesh convergence analysis was conducted while analyzing the wing. To carry out this study the distance to the domain boundaries along with the mesh size on the wing, and on the boundaries were varied until the simulation results converged. The converged domain size along with a converged mesh are shown in Fig.7.4. The boundary conditions were set to freestream values, except at the root of the wing, where a symmetric boundary condition is imposed to reduce computational cost.

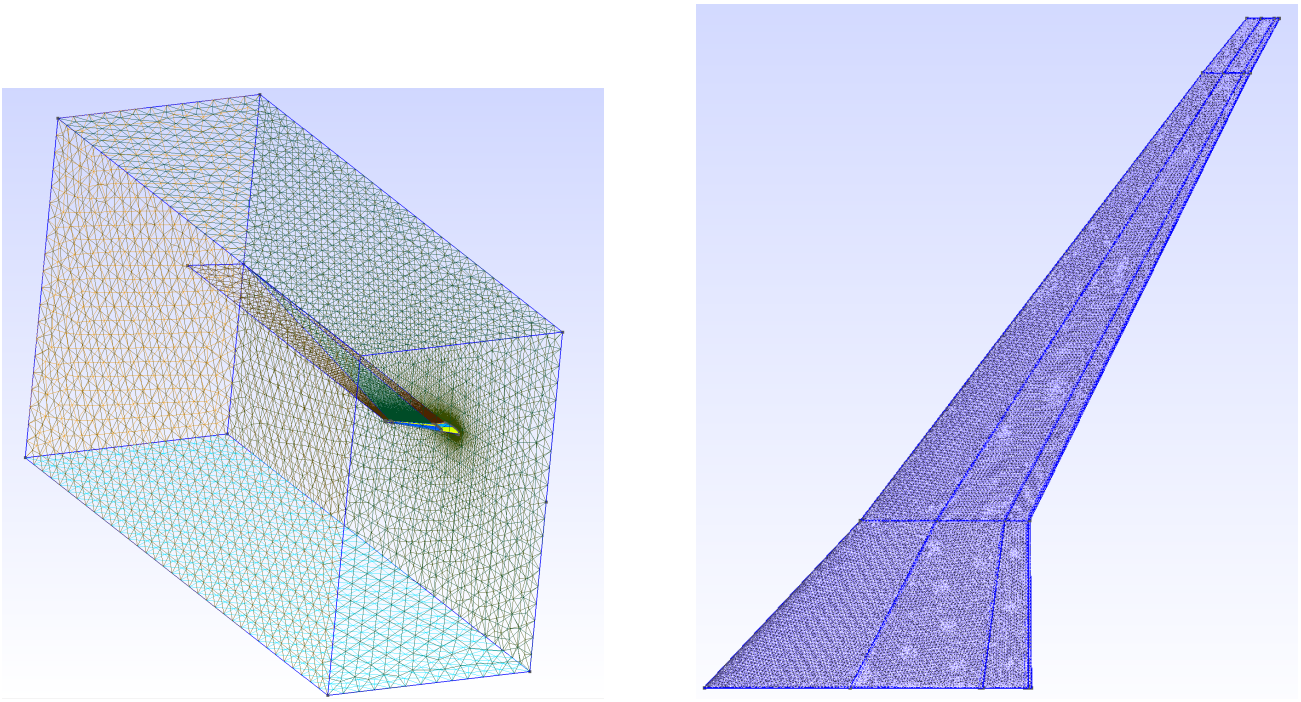

Figure 7.4: Image showing domain used for DARTflo simulation along with a converged mesh of the wing.

After ensuring that the results are converged, the aerodynamic performance of the wing can be analyzed by using the pressure distribution on the wing. The pressure distribution for the mid-cruise scenario is shown in Figure 7.5. By integrating this pressure across the surface of the wing, the Lift, Drag, and Moment coefficients can be calculated. These coefficients can then be used to characterize the performance of the wing for different flight regimes shown in Figure 7.6, or the efficiency of the wing through its lift distribution shown in Figure 7.7.

7.3.2 Aerodynamic Analysis Results

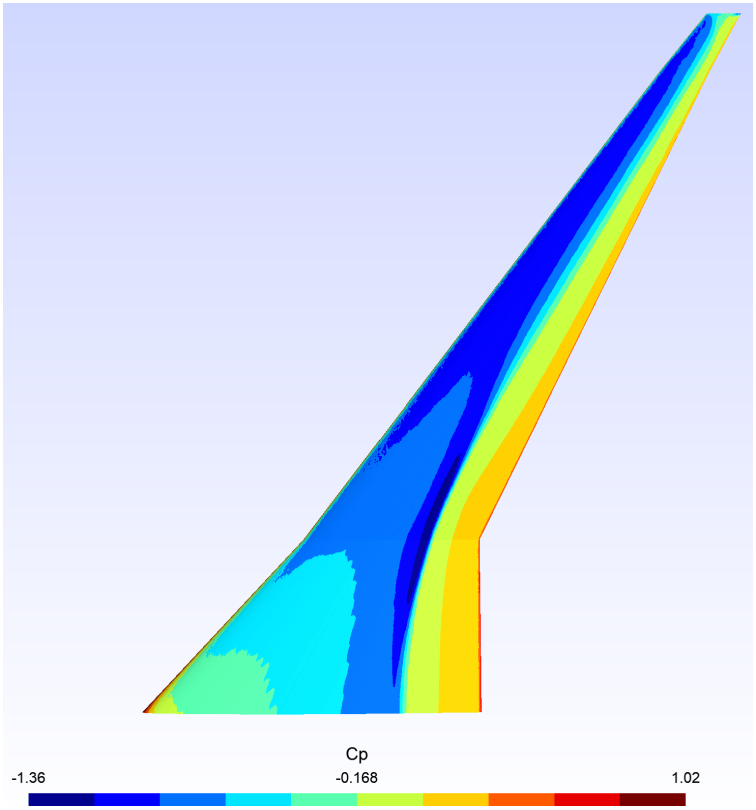

Figure 7.5: Coefficient of Pressure (C_P) on the upper surface of the wing for M = 0.85, α = 2.75°

To determine the efficiency of the wing at different flight speeds, the Lift/Drag ratio was calculated over a sweep of potential cruise mach numbers for the mid-cruise weight configuration. The results of which are shown in Fig. 7.6.

Analyzing Fig. 7.6 reveals that the performance of the wing drops sharply as the mach number is increased through the transonic regime, with the Lift/Drag ratio at the target cruise Mach of 0.92 being nearly half of the Lift/Drag ratio at the required cruise Mach of 0.85.

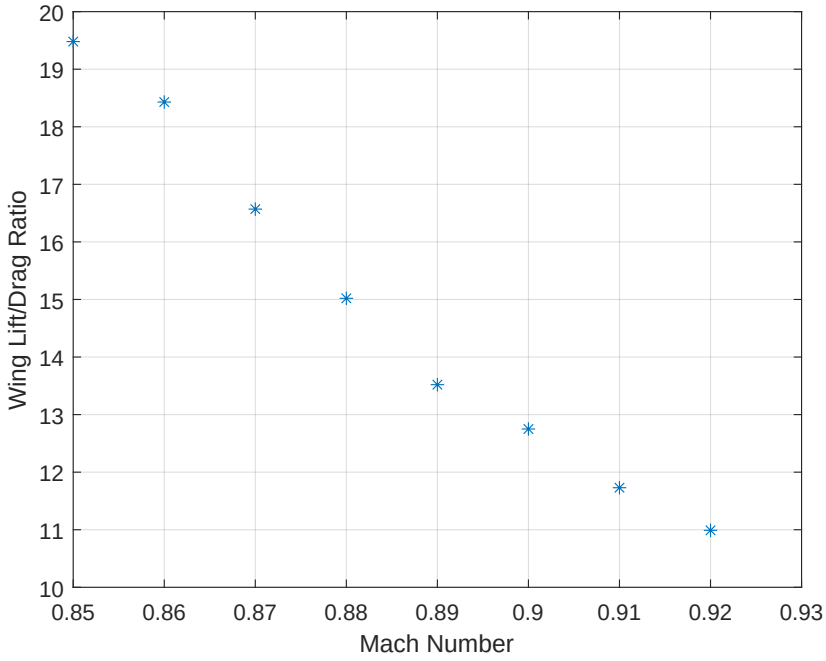

Figure 7.6: Lift/Drag ratio of wing for different mach numbers in mid-cruise at M = 0.85, altitude = 43000 ft.

To determine the efficiency of the lift produced by the wing, the spanwise lift distribution of the half-wing can be compared to that of an elliptical lift distribution, where the efficiency factor is 1.0. This comparison is displayed in Fig.7.7, and shows that the lift distribution matches the shape of the elliptic lift distribution with differing data near the wing root, and near b = 6-10 ft. This discrepancy in lift distribution may be caused by the placement of the Yehudi located at 11.464 ft. This could be mitigated by further varying the pitch of the wing near the Yehudi to reduce the variance and further improve the efficiency of the wing.

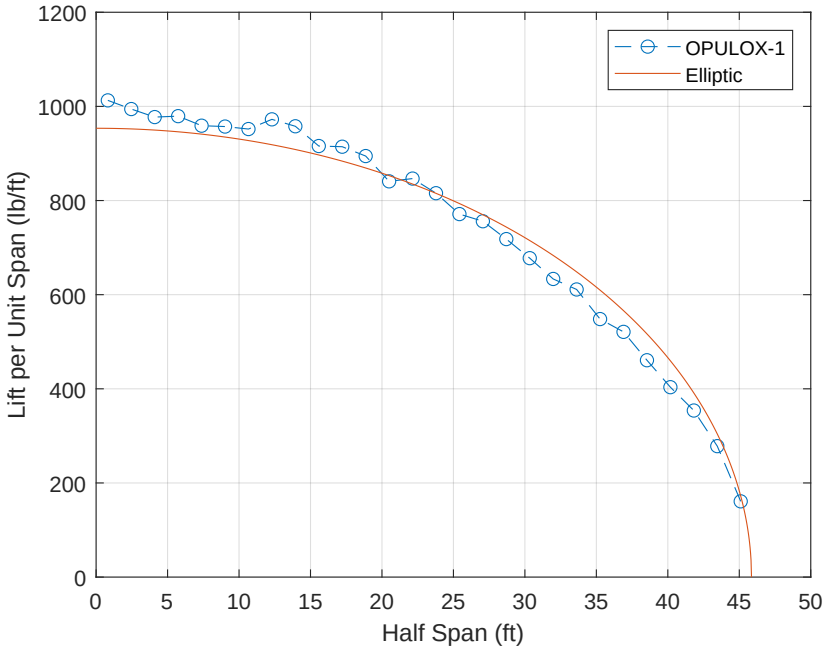

Figure 7.7: Plot of Spanwise lift distribution of Opulux wing compared to an elliptical lift distribution

7.4 Drag study

7.4.1 Methodology

The drag evaluation process for the OPULOX-1 relies on a detailed decomposition of the main aerodynamic contributions proposed by Torenbeek in ref [30]: vortex-induced drag, profile drag, interference effects and protuberance drag. This breakdown, illustrated in Fig.7.8, was applied across the key flight phases: cruise, takeoff, landing, and climb. Although the underlying methodology is rooted in general aircraft design principles, specific adjustments were introduced to reflect the aerodynamic behavior of modern business jets. Where necessary, complementary models and empirical relations from alternative references were incorporated to enhance the fidelity of the predictions.

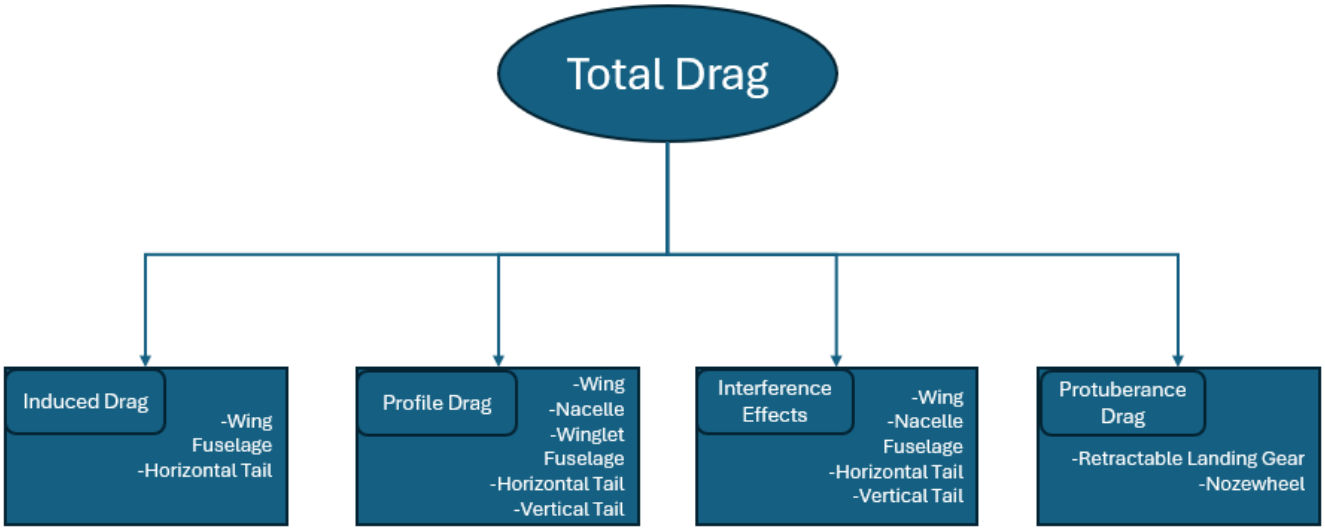

Figure 7.8: Illustration of the Drag Breakdown.

Vortex-Induced Drag

The drag originating from lift production, commonly referred to as vortex-induced drag, is evaluated separately for the main lifting surfaces and the fuselage. To maintain clarity in the modeling process, interactions between components are not considered at this stage. The wing's contribution is estimated using aerodynamic surface theory, refined to include the influence of wing twist on vortex patterns. A similar methodology is applied to the horizontal tail, acknowledging its secondary yet non-negligible role. Although the fuselage generates only a modest amount of lift-related drag, it has been accounted for through the use of experimental correlations, providing a reasonable estimate in the absence of direct modeling of component interaction effects.

Profile Drag

The profile drag comprising both skin friction and pressure drag is estimated using an approach based on the flat plate analogy. An adjustment factor is introduced to better reflect the geometric discrepancies between an idealized flat plate and an actual streamlined shape. The thickness correction factor ϕ_W, introduced by Egbert Torenbeek, is employed to more precisely capture the characteristics of the wing's airfoil geometry.

$$\phi_W = 2.7 \cdot \left(\frac{t}{c}\right) + 100 \cdot \left(\frac{t}{c}\right)^4 \tag{7.4}$$

where $\frac{t}{c}$ corresponds to the maximum thickness to chord ratio. Assuming a fully turbulent boundary layer, as done by Torenbeek in his reference work, results in a conservative estimation of the total drag. Since the laminar portion is neglected while it would normally contribute to lowering drag this approach slightly overestimates the aircraft's overall drag. Accordingly, the skin friction coefficient used in this study is the one proposed by Egbert Torenbeek.

$$C_F = \frac{0.455}{(\log_{10}(\mathrm{Re}))^{2.58}} \tag{7.5}$$

Interference Effects

In the drag estimation, additional correction terms are introduced to account for interactions between components, which are otherwise treated as isolated. These interference effects are expected to be minor, and in some cases may even reduce total drag. However, due to the difficulty of accurately quantifying such effects during early design stages, the adopted approach relies on simplified approximations that likely underestimate their actual impact. The interactions considered include those between the wing and fuselage, wing and tailplane, as well as between the fuselage and engine nacelles.

Protuberance Drag

The drag penalty due to surface imperfections and roughness have been taken into account for the cockpit wingshield and some other extras like the drag which appears when control surfaces such as the ailerons or the rudder are retracted, but these contributions are quite small compared to the total drag on the aircraft.

Total Drag

Once the various sources of drag have been individually assessed, their combination yields the total drag corresponding to a given flight phase. This aggregation follows a structured breakdown of drag components, typically referenced to the wing reference area S, and can be expressed in the form:

$$C_{D_j} = \frac{(C_D S)_j}{S} \tag{7.6}$$

Each partial drag area $(C_D S)_j$ contributes to the total, which may then be reformulated using the lift coefficient C_L to obtain the polar representation of drag for different configurations:

$$C_D = A + B \cdot C_L + D \cdot C_L^2 \tag{7.7}$$

where A, B, and D are coefficients reflecting parasitic, linear, and induced drag contributions respectively.

7.4.2 Results

Optimal cruise

The cruise segment represents the majority of a private jet's flight profile. As such, the aerodynamic design choices have been primarily oriented toward maximizing efficiency during this phase. The drag breakdown corresponding to this optimized configuration will be examined with particular attention.

In this configuration, both the engines and the main landing gear are stowed to minimize additional drag. Given that the fuselage axis is aligned with the freestream, its contribution to induced drag is considered negligible.

Numerical results for the distinct drag components are compiled in Tab. 22 where the coefficients C_{D_i}, C_{D_p}, C_{int}, and $C_{D_{pr}}$ correspond respectively to induced drag, profile drag, interference effects, and protuberance drag.

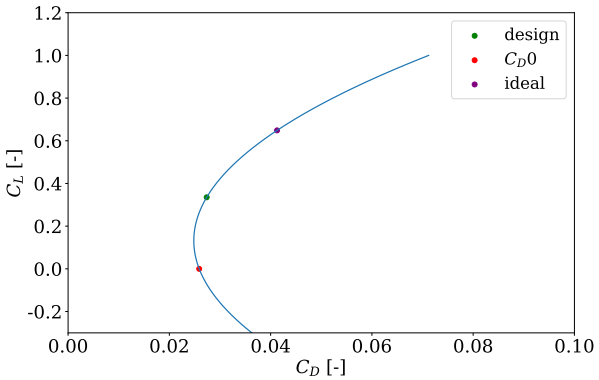

Figure 7.9: Illustration of the Drag Polar in Cruise Conditions.

	C_L	C_D	C_L/C_D
Design	0.3308	0.0273	12.134
Zero-Lift	0	0.0259	–
Ideal	0.6488	0.0413	15.719

Table 21: Associated Numerical Values of Drag and Lift coefficients.

Vortex-Induced Drag: C_{D_i}	**Profile Drag:** C_{D_p}	**Interference Effects:** $C_{D_{int}}$	**Protuberance Drag:** $C_{D_{pr}}$
0.00302	0.0169	0.00257	0.00476

Table 22: Distinct Contributions of the Different Drag Type in Cruise Conditions.

On figure 7.9 it can be observed that the design point does not coincide exactly with the optimal aerodynamic point. However, this is expected, as the aircraft's geometry and design are also driven by other requirements, such as fuel volume, structural constraints, and system integration. The result is therefore a compromise between multiple objectives, with the aim of remaining as close as possible to the ideal aerodynamic efficiency.

Equation 7.7, which defines the total drag coefficient in terms of the lift coefficient, can be expressed using three coefficients: A, B, and D. To better understand their individual roles, a breakdown of their contributions during cruise conditions is shown in Figure 7.10. The term A corresponds to the parasitic drag component and remains constant across all lift coefficients, reflecting the baseline drag when no lift is produced. Initially, the total drag is dominated by the constant A component; however, as the lift coefficient increases, The coefficient B starts to become significative and decreases the drag coefficient until, beyond a certain threshold around unity the nonlinear effect associated with D begins to dominate, indicating its growing importance at higher lift regimes.

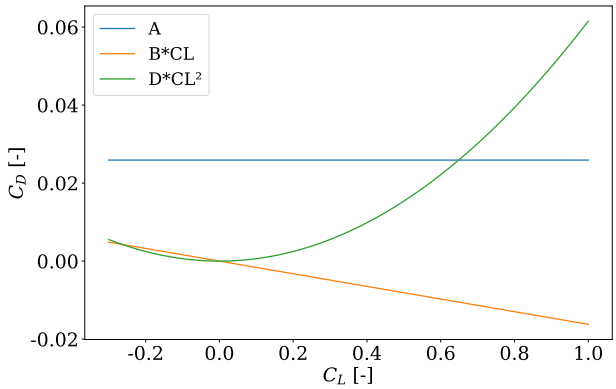

Figure 7.10: Parametric influence of drag model coefficients on total drag with respect to lift variation in cruise conditions

Based on these results, the calculated Oswald efficiency factor is 0.758 indicating a moderate level of aerodynamic efficiency for the wing configuration under consideration. This value is slightly lower than the previously assumed value of 0.8, but the difference is relatively small and remains within an acceptable range for preliminary design purposes. Therefore, the reduction in efficiency is considered negligible in this context.

Takeoff

During the takeoff phase, the aerodynamic configuration of the aircraft differs significantly from the one optimized for cruise. For the OPULOX-1, the propulsion system is operating at maximum thrust, and the main landing gear is extended, which introduces additional drag, $C_{D_{Gr}}$, due to protruding elements. However, since takeoff occurs close to the ground, ground effect contributes to a reduction in overall drag. To reflect these changes in the drag assessment, specific increments are added to account for the different sources of additional drag. Following a methodology inspired by classical aircraft design approaches, the ground effect

is incorporated as a direct adjustment to the total drag.

$$C_{L_{\text{takeoff}}} = 1.101, \qquad C_{D_{\text{takeoff}}} = 0.1337$$

C_{D_i}	C_{D_p}	$C_{D_{int}}$	$C_{D_{pr}}$	$C_{D_{Gr}}$
0.0542	0.0529	0.0154	0.00498	0.00648

Table 23: Distinct Contributions of the Different Drag Type in takeoff Conditions.

Landing

For the landing phase. It is the same as in the takeoff phase except that The engines now try to slow the aircraft and thus increase the drag. The inclination of the wing increases the lift coefficient wich evidently increases the drag coefficient

$$C_{L_{\text{Landing}}} = 2.020, \qquad C_{D_{\text{Landing}}} = 0.3075$$

C_{D_i}	C_{D_p}	$C_{D_{int}}$	$C_{D_{pr}}$	$C_{D_{Gr}}$
0.1702	0.0816	0.0155	0.0150	0.0254

Table 24: Distinct Contributions of the Different Drag Type in Landing Conditions.

Climb

The climb configuration refers to a flight condition where the two GE-Passport engines are operational, providing thrust to facilitate altitude gain, while the main landing gear is retracted. This configuration is similar to the optimal cruising configuration, with the primary difference being the 1.1° angle of attack of the fuselage.

$$C_{L_{\text{Climb}}} = 0.6198, \qquad C_{D_{\text{Climb}}} = 0.0634$$

C_{D_i}	C_{D_p}	$C_{D_{int}}$	$C_{D_{pr}}$
0.0252	0.0264	0.00899	0.00241

Table 25: Distinct Contributions of the Different Drag Type in Climb Conditions.

Discussion

The drag characteristics of the OPULOX-1 across various flight phases are illustrated in Fig. 7.11, which outlines the contributions from each drag component. A closer look reveals that, during takeoff and landing, the total drag coefficient presented previously are the sum of multiple components where one of them is negative and characterizes the interaction with the ground.

Among all the contributing factors, profile drag predominates the total aerodynamic resistance during cruise, while the contribution of induced vortex drag becomes significantly more important in other flight phases, at times surpassing profile drag. This is primarily due to the extended wetted area of the OPULOX-1, which is a consequence of its large wing surface designed to ensure high lift performance. Additionally, the flow characteristics over the wing, particularly the early transition to turbulent flow during powered phases, further contribute to the increase in profile drag.

Vortex-induced drag increases in takeoff, landing, and climb phases due to higher angles of attack and greater lift demands. These phases require more lift, which results in stronger vortex formation and higher induced drag. Additionally, lower speeds during these phases further amplify vortex-induced drag, making it more significant than in the cruise phase.

A noticeable difference between the cruise configuration and both takeoff and climb configurations lies in the profile drag level. This increase can be attributed to several factors inherent to low-speed, high-lift conditions. During takeoff, high lift coefficients are required, typically achieved by deploying high-lift devices such as slats and flaps. These elements disrupt the boundary layer development, leading to an earlier transition to turbulence and thus greater skin friction. Furthermore, the lower Reynolds number associated with the reduced airspeed in takeoff conditions amplifies viscous effects, further increasing profile drag. In contrast, the climb configuration involves partially retracted high-lift devices and a more streamlined flow, leading to lower profile drag. The cruise configuration, being optimized for low drag and moderate lift, naturally presents the most favorable profile drag characteristics.

In addition, profile drag rises again in landing configuration, for similar reasons related to flow behavior. Another variation is seen in protuberance drag, which increases during takeoff and landing due to the deployment of the main landing gear. Interference drag increases significantly between the cruise phase and other phases due to changes in airflow interactions between the aircraft components, but it remains relatively low compared to profile drag and vortex-induced drag, which dominate the overall aerodynamic drag.

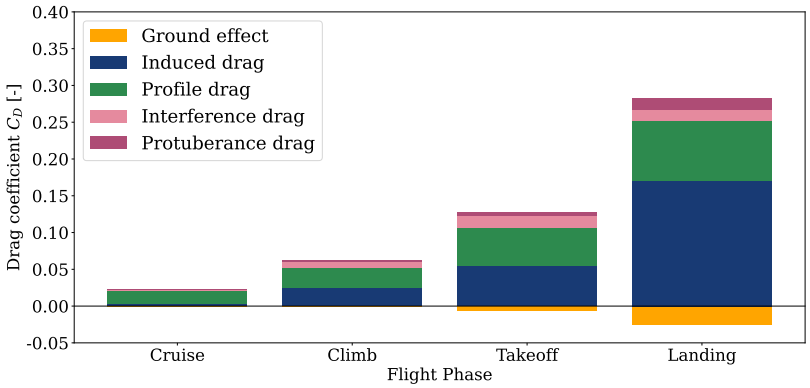

Figure 7.11: Drag Contributions in the Different Flight Phases.

The lift to drag ratios are summarized in the table 26.The lift to drag ratio in cruise is the highest because the aircraft operates at an optimal angle of attack and speed, balancing lift and drag efficiently for fuel economy. In takeoff, the aircraft must generate a significant amount of lift to overcome its weight, which increases the angle of attack and, consequently, the induced drag. This results in a lower lift to drag ratio compared to cruise. During landing, the aircraft maintains a high angle of attack to ensure enough lift at lower speeds, which increases induced drag further, reducing the ratio. Finally, in climb, the aircraft requires sufficient lift to gain altitude, but the drag is somewhat lower than in landing as the aircraft isn't descending or heavily loaded. The climb phase thus has a moderately high lift-to-drag ratio, though still lower than cruise due to the necessary balance between lift and drag at lower speeds.

	Cruise	**Takeoff**	**Landing**	**Climb**
CL/CD	12.134	8.222	6.570	9.777

Table 26: Lift to Drag Ratios for the Different Flight Stages.

Engine Failure during Cruise

As part of the flight safety assessment for the OPULOX-1 altitude. This scenario considers a sudden and complete loss of thrust, assuming no residual power remains available from the propulsion system.

Although the OPULOX-1 does not use a propeller-based propulsion system, a conservative estimation was conducted to evaluate the aerodynamic penalties resulting from non-operating engine components exposed to the freestream.

Parasitic drag increases significantly following engine shutdown, as structural elements such as nacelles, air intakes, and any non-retracted components contribute more prominently to aerodynamic resistance.

In addition, the absence of propulsive flow alters the local airflow around the engine housings. This change in flow characteristics increases the likelihood of separation and amplifies drag in those regions.

It is important to note that, although the aircraft is no longer in steady cruise flight after an engine failure, the aerodynamic analysis

is based on the cruise configuration in order to provide a conservative estimate of the drag increase at the moment of failure. The estimated aerodynamic penalty in this failure scenario is represented by a drag coefficient increment of:

$$\Delta C_{D\text{failure}} = 0.0148$$

which equates to a rise of approximately 53.6% in total drag compared to the optimal cruise configuration. Detailed values for drag and the lift to drag ratio during engine failure are provided in the table 27.

	Symbol	Value [-]
Total Drag	$C_{D\text{failure}}$	0.0421
Lift to Drag Ratio	$\frac{L}{D_{failure}}$	7.861

Table 27: Drag Coefficient and L/D Ratio Under Engine-Out Conditions.

7.4.3 Comparison with DARTFlo software

Fig. 7.12 shows the drag coefficient C_D as a function of the lift coefficient C_L, computed using both the DARTFlo software and the Torenbeek method. A clear divergence between the two estimations appears beyond $C_L \approx 0.4$, where the drag predicted by DARTFlo becomes higher than that given by the Torenbeek method.

This behavior can be explained by the intrinsic nature of the two approaches. DARTFlo relies on a potential flow method, which does not inherently account for viscous effects such as skin friction and doesn't predict really accurately the wave drag and those errors on the prediction of these components rise quadratically with the lift coefficient. Consequently, the C_D predicted by DARTFlo is primarily composed of vortex-induced drag. Since friction and compressibility effects are neglected, the shock location on the chord is not accurately captured, typically being delayed further aft than it should be. As a result, the drag rise associated with transonic effects is underestimated or shifted.

In contrast, the Torenbeek method [33] is based on experimental correlations derived from wind tunnel data and real aircraft measurements. These include contributions from all major drag components: profile drag, vortex-induced drag, wave drag, and interference effects. Thus, it offers a more comprehensive estimation of total drag, particularly at higher lift coefficients where viscous and compressibility effects become significant. The increase in compressibility effects can be explained by the presence of more shocks at high lift coefficients

The intersection of the two curves can be attributed to these modeling differences. At low C_L, DARTFlo underpredicts total drag due to the absence of friction and wave drag. However, at higher C_L, the increase in induced drag becomes dominant, and

DARTFlo's predictions exceed those of Torenbeek, which accounts for a more balanced contribution of drag components. From the design perspective, this discrepancy is reflected in the values of C_{D0}, C_D, and the lift-to-drag ratio C_L/C_D reported in Tab. 28. The design point, typically chosen around the optimal C_L/C_D, would be affected depending on the method used, with DARTFlo potentially leading to an overestimation of performance at low C_L, and an underestimation at higher C_L values.

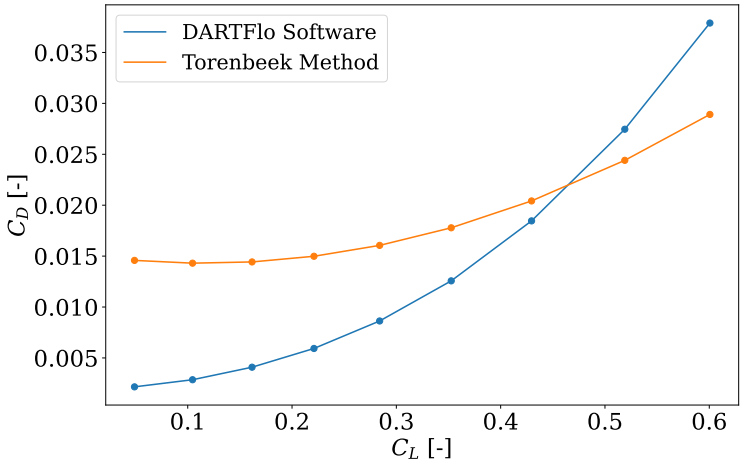

Figure 7.12: Computed drag coefficient comparison between Torenbeek method and DARTFlo software

	Torenbeek	**DARTFlo**
CL [-]	0.3308	0.3308
CD0 [-]	0.0151	0.00196
CD [-]	0.0172	0.0113
CL/CD [-]	19.267	29.223

Table 28: Drag Coefficient and L/D Ratio Under Engine-Out Conditions.

7.5 Structural analysis

To assess the structural limits of the aircraft's operational flight envelope, the Placard Diagram and the V-n Diagram are first examined. These two flight envelopes make it possible to determine the aerodynamic loads acting on the aircraft, which are then used to design its structure.

7.5.1 Placard Diagram

As illustrated in Fig. 7.13, the Placard Diagram defines the aircraft's flight envelope, which is delimited by different types of boundaries. First, depending on the altitude at which the aircraft is flying, the minimum allowable velocity is given by the stall velocity. Then, the maximum altitude that the aircraft can reach is determined by its ceiling, where the available lift and thrust become insufficient to sustain further ascent. (Note that the ceiling of the plane will be computed in the Performance Analysis section 7.6.) Finally, the maximum speed at which the aircraft can operate depends on where the aircraft is flying relative to its design altitude. Above the design altitude, the maximum speed is limited to the maximum cruise speed, or dive speed if the aircraft is descending. Since the temperature remains nearly constant beyond the stratospheric limit, the speed of sound is considered a constant, meaning the aircraft's maximum true airspeed (TAS) remains constant at higher altitudes. Below the design cruise altitude, the aircraft's maximum flight speed is constrained by dynamic pressure due to structural limitations.

The most critical design case lies near the intersection of the Mach and dynamic pressure limits, corresponding to the dive condition. For OPULOX-1, the dive Mach number was set to $M_D = 1.25M_C$, ensuring the structure is evaluated under the most demanding flight conditions.

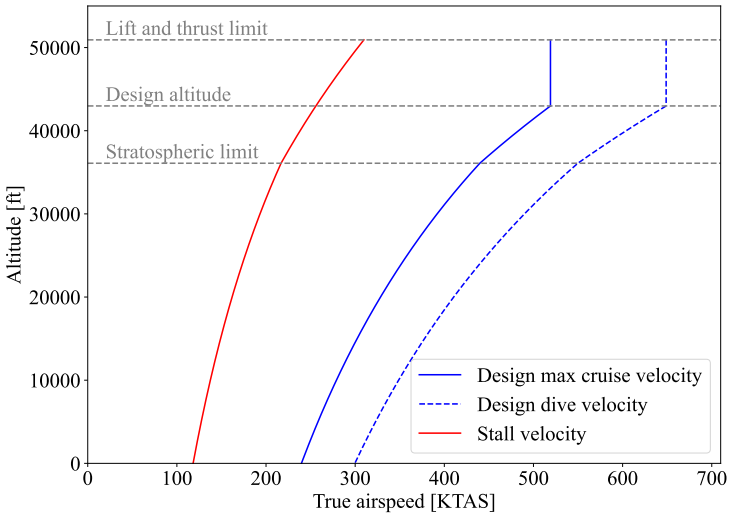

Figure 7.13: Placard diagram for the jet OPULOX-1.

Therefore, the design max cruise velocity and design dive velocity boundaries are derived from the maximum cruise speed V_C, corresponding to M_C, evaluated with the corresponding air properties at cruise altitude. This maximum cruise speed has been obtained by equalizing thrust and drag at the design cruise altitude. Because both drag and thrust models depend on velocity, iterative process has been used to find the value of V_C leading to this equality. At the end, as mentioned earlier in the report, the obtained max cruise speed V_C is 519.06 knots, corresponding to a Mach number of $M_C = 0.935$.

7.5.2 V-n Diagram

In order to consider the different critical loading conditions encountered by the aircraft during flight,the maneuver and gust envelopes of the plane need to be investigated. These envelopes define the operational flight zone where the aircraft can safely maneuver without risking structural failure.

The maneuver diagram shows how load factor varies with airspeed during maneuvers. At low speeds, the maximum load factor is limited by the aircraft's maximum lift coefficient, while at higher speeds it is restricted by FAR Part 25 regulations [16]. For airplanes heavier than 50,000 lbs, the maximum maneuver load factor is +2.5, with a minimum of -1.0 up to the cruise speed V_c, decreasing linearly to 0 at dive speed V_D. It is also required that the aircraft can finish its mission when it has been subjected to a load factor $n_{\text{ultimate}} = 1.5\, n_{\text{max}}$, i.e. the aircraft structure can have permanent deformations, but the plane is still flyable.

Vertical gust loads must also be evaluated across the full speed range, with their calculations detailed in FAR regulations. For the design altitude of the aircraft, the FAR's regulations state that the maximum equivalent gust speeds, encountered for different flight speeds, are equal to: $U_{E,C} = U_{E,B} = 29.60$ ft/s and $U_{E,D} = 14.80$ ft/s. These gust speeds allow for the definition of the boundaries of the gust envelope, illustrated in Fig. 7.14. Since the gust envelope is entirely contained within the maneuver envelope, the maximum structural constraints imposed by gusts are lower than those from maneuvers. As a result, the critical points, defined by a specific speed and load factor, are determined solely by the maneuver envelope.

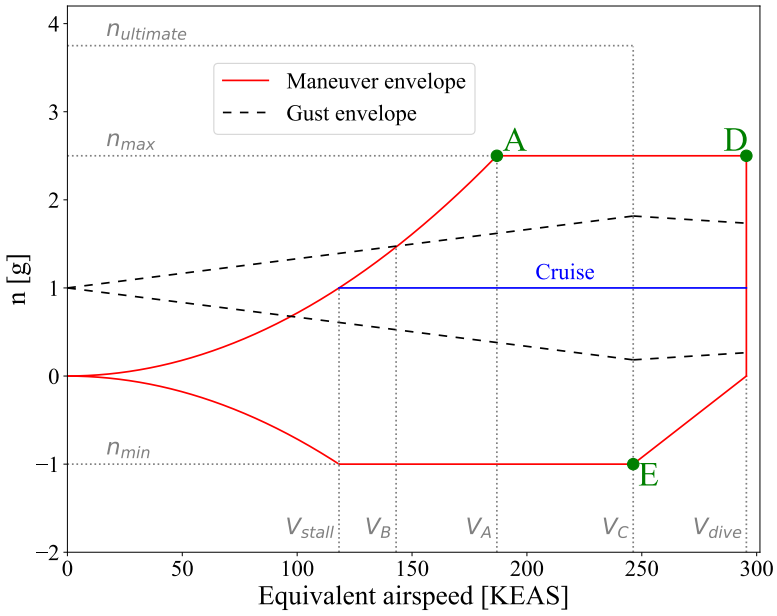

Figure 7.14: Gust and maneuver envelope for the jet OPULOX-1 at design cruise altitude of 43,000 ft.

From the full V-n diagram, several key speeds can be determined, as presented in Tab. 29. To ensure the aircraft meets the FAR

requirements and is capable of safe flight, the following inequality must be verified:

$$V_B < V_{\text{stall}} \left[n_g(V_C)\right]^{1/2}. \tag{7.8}$$

Using the key speeds derived from the V-n diagram and the computed gust load factor at cruise speed, $n_g = 1.70$, this results in $143.06 < 154.12$ ft/s, which satisfies the requirement.

It can be noticed that the maximum cruise speed V_C may look small when computed in equivalent airspeed. This is due to the high altitude at which the aircraft is flying.At cruise altitude, the air density is $\rho = 5.06 * 10^{-4}$ slug/ft^3, while at sea level, the air density is $\rho_{SL} = 0.002377$ slug/ft^3. Therefore, the maximum cruise equivalent air speed is computed as:

$$V_C(EAS) = V_C(TAS)\sqrt{\frac{\rho}{\rho_{SL}}} = 519.06\sqrt{\frac{0.01721}{0.07647}} = 246.2. \tag{7.9}$$

	Velocities [KEAS]
Cruise stall speed, V_{stall}	118.21
Design speed for maximum gust, V_B	143.06
Design maneuvering speed, V_A	186.92
Design maximum cruise speed, V_C	246.26
Design dive speed, V_{dive}	295.51

Table 29: Key equivalent airspeeds of the flight envelope.

The aircraft structure is designed to withstand the most critical aerodynamic loads. These loads are evaluated at three specific points (A, D, E) on the maneuver envelope, shown in Fig. 7.14. Point A corresponds to the stall limit, where a high angle of attack generates significant loads. Point D represents the maximum positive load factor ($n = 2.5$) at the aircraft's dive speed (V_{dive}). Point E is the equivalent for the maximum negative load factor.

7.5.3 Material selection

The material was selected using *Granta* software [7]. The objective is to find a material that has low density but high yield strength and high Young's modulus. Another criteria is that material must not be too expensive. Using material properties charts and material indices, the selected material is *Aluminum, 7068 ,T6511*. Its main properties are summarized in the table bellow.

Properties	Value
Density [lbs/in³]	0.103
Yield strength [ksi]	107.3
Shear strength [ksi]	54.4
Young's modulus [Msi]	1.06

Table 30: Properties of *Aluminum, 7068 ,T6511*.

7.5.4 Aerodynamic loads

In order to be able to dimension the aircraft's structure, the aerodynamic loads needs to be evaluated. The aircraft is subjected to several loads and moment that are computed at critical points of the maneuver envelope. The 3 critical points at which the loads are computed are: A (V_A, 2.5) , D (V_D, 2.5) and E (V_C, -1) represented on Fig. 7.14. The computation of the loads is done by computing a vertical and a momentum equilibrium around the centroid.

$$n \cdot W = L_W - P + T \cdot \sin(\alpha - \alpha_{wing}) \tag{7.10}$$

$$\ddot{\theta} I_\theta = -d_{LW} \cdot L + d_{LT} \cdot P - d_T \cdot T + d_{DW} \cdot D_W - d_{DB} \cdot D_B + M \tag{7.11}$$

The lever arms are shown in Fig. 7.15.

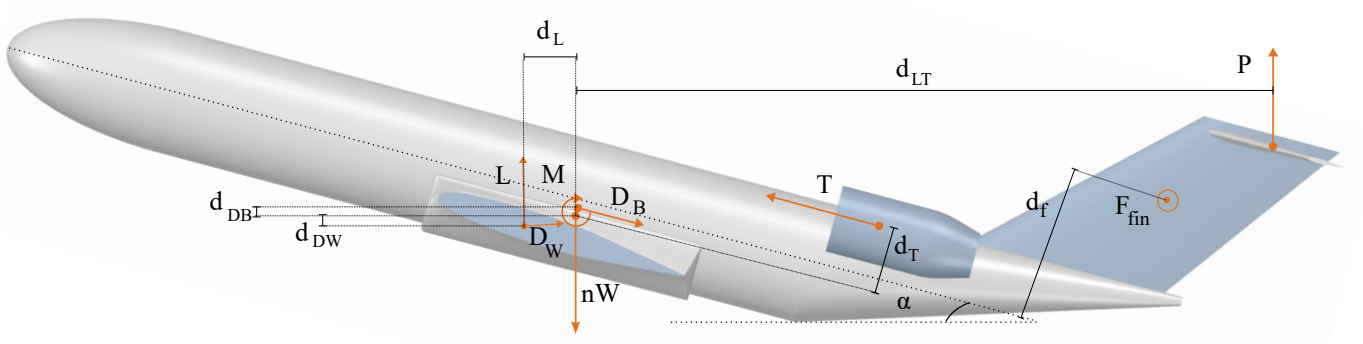

Figure 7.15: Aerodynamic loads and lever arm representation.

The maximum allowable pitching acceleration, $\ddot{\theta}$, is determined according to FAR 25.331:

- **if** $n > 0$ **:**

$$\ddot{\theta} = \frac{39n}{v}(n - 1.5) \tag{7.12}$$

- **if** $n < 0$ **:**

$$\ddot{\theta} = \frac{-26n}{v}(n - 1.5) \tag{7.13}$$

A positive pitching moment corresponds to a nose-up rotation. The forces acting on the aircraft include: the wing drag D_W, the wing lift L, the tail lift P, the aircraft weight W, the engine thrust T, and the body drag D_B. The variable I_θ is the moment of inertia around the center of gravity. As the angle of attack is unknown for critical points D and E an additional equation is required in order to solve the system.

$$L = \frac{1}{2}\rho V^2 S C_L \tag{7.14}$$

Solving this system of equation leads to the computation of the loads at the 3 critical points represented in the table bellow. The torsion moment around the fuselage is computed by applying a moment equilibrium involving the aerodynamic moment produced by the tail and force applied on the fin. The lever arm is represented on Fig. 7.15.

$$M_{fus} = M_{tail} + F_{fin} \cdot d_f. \tag{7.15}$$

Critical Point	**Load Factor** [-] α [°]	**P** [lbf]	**L** [lbf]	$\mathbf{F_{fin}}$ [lbf]	$\mathbf{M_{fus}}$ [lbf.ft]
2.5	13.00	$-1.21 \cdot 10^4$	$2.39 \cdot 10^5$	$1.64 \cdot 10^4$	$-2.17 \cdot 10^5$
2.5	4.95	$-2.12 \cdot 10^4$	$2.49 \cdot 10^5$	$3.11 \cdot 10^4$	$-4.14 \cdot 10^5$
-1	-11.00	$-6.32 \cdot 10^3$	$-8.18 \cdot 10^4$	$2.16 \cdot 10^4$	$-2.87 \cdot 10^5$

Table 31: Aerodynamic loads computation for each critical case solving equilibrium equations.

7.5.5 Rear fuselage design

The design of the rear fuselage is first done analytically. Two hypothesis are made:

- the specific inertia of stringers is neglected and stringers are modeled by booms of equivalent section,
- the skin is only submitted to shear while the booms are only submitted to bending.

Rear fuselage loads

The rear fuselage must support the weight of engine W_{eng}, the weight of the tail and its specific weight. The specific weight is modeled as a rectangular load for the part with a constant areal section and a trapezoidal load for the conical part of the fuselage. In order to compute the shear stress and bending moment in each section of interest, the resultant load of the specific weight are computed. Q_1 is the resultant of the triangular load of the end of the fuselage, Q_2 is the one of representing the rectangular load of the end of the fuselage and Q_3 is the resultant of the rectangular load of the first part of the fuselage. All these loads are represented on Fig. 7.16

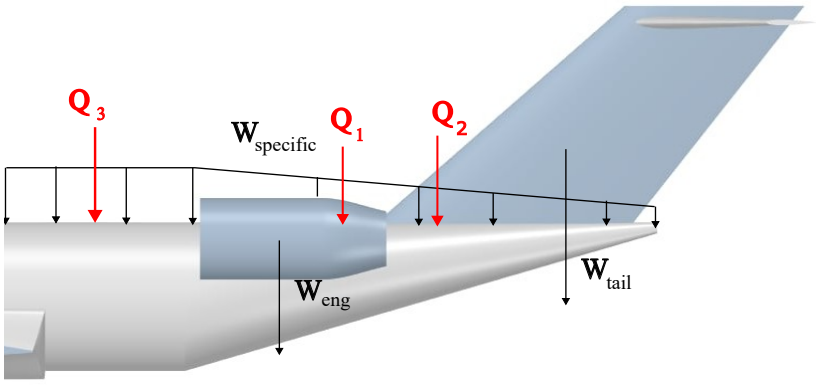

Figure 7.16: Rear fuselage loads, Q are the resultant of distributed loads.

The structure is designed by computing the loads at three sections: section AA′ at the end of the wing, section BB′ just before the tail, and section CC′ positioned midway between AA′ and BB′ as show in Fig. 7.18. First, shear stresses and bending moments are computed at each section through a Shear Force diagram (SFD). Once this is performed the resultant loads and moment at each section are computed using the following equilibrium equations:

$$T_y = -F_{fin} \tag{7.16}$$

$$T_z = (SF - P) \cdot cos(\alpha - \alpha_{wing}) \tag{7.17}$$

$$M_y = BM - P \cdot d_P \cdot cos(\alpha - \alpha_{wing}) \tag{7.18}$$

$$M_z = F_{fin} \cdot d_{fin} \tag{7.19}$$

$$M_x = -M_{fin} - d_{\text{tail, height}} \cdot F_{fin} = -M_{fus} \tag{7.20}$$

Distances, different forces and moment are defined as follow :

SF and BM are defined respectively as the shear force and the bending moment at the section of interest. The section location and the reference axis for the loads are represented on the figures bellow.

The resulting forces at each critical point for each section are represented in the three tables bellow: Tab.32, Tab.33 and Tab.34.

- d_P: distance along the fuselage axis from the section location to the application point of P,
- d_{fin}: distance along the fuselage axis from the section location to the application point of F_{fin},
- $d_{\text{tail, height}}$: lever arm along the z-axis between the fuselage centerline and the point of application of F_{fin},
- α_{wing}: the angle of attack of the wing at the location of the aerodynamic center of the wing,
- M_{fin}: torsion aerodynamic moment of the fin,
- M_{fus}: torsion moment along the fuselage axis

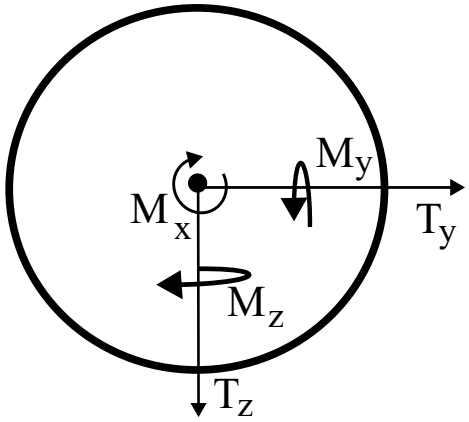

Figure 7.17: Reference axis for fuselage loads computation.

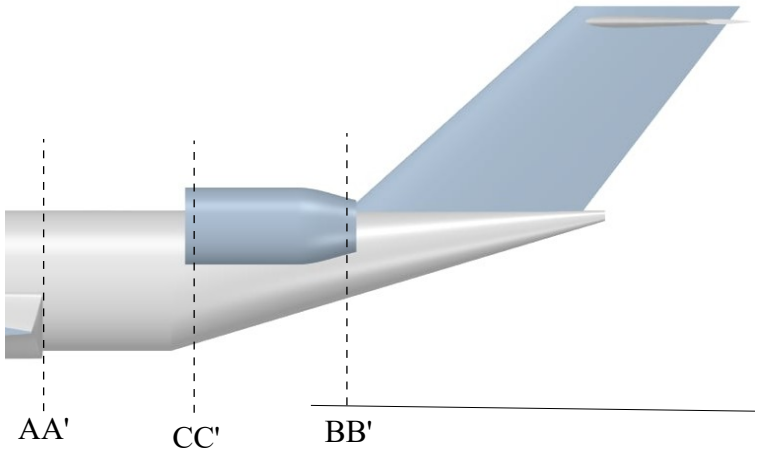

Figure 7.18: Representation of studied sections.

Critical Point	$\mathbf{T_y}$ [lbf]	$\mathbf{T_z}$ [lbf]	$\mathbf{M_y}$ [lbf.ft]	$\mathbf{M_z}$ [lbf.ft]	$\mathbf{M_x}$ [lbf.ft]
A	$-1.64 \cdot 10^4$	$2.78 \cdot 10^4$	$8.27 \cdot 10^5$	$6.47 \cdot 10^5$	$-2.17 \cdot 10^5$
D	$-3.11 \cdot 10^4$	$3.75 \cdot 10^4$	$1.19 \cdot 10^6$	$1.23 \cdot 10^6$	$-4.14 \cdot 10^5$
E	$-2.16 \cdot 10^4$	$-2.03 \cdot 10^2$	$8.15 \cdot 10^4$	$8.51 \cdot 10^5$	$-2.87 \cdot 10^5$

Table 32: Critical Loads at section AA'

Critical Point	$\mathbf{T_y}$ [lbf]	$\mathbf{T_z}$ [lbf]	$\mathbf{M_y}$ [lbf.ft]	$\mathbf{M_z}$ [lbf.ft]	$\mathbf{M_x}$ [lbf.ft]
A	$-1.64 \cdot 10^4$	$2.01 \cdot 10^4$	$1.86 \cdot 10^5$	$2.22 \cdot 10^5$	$-2.17 \cdot 10^5$
D	$-3.11 \cdot 10^4$	$2.96 \cdot 10^4$	$2.98 \cdot 10^5$	$4.20 \cdot 10^5$	$-4.14 \cdot 10^5$
E	$-2.16 \cdot 10^4$	$2.87 \cdot 10^3$	$5.47 \cdot 10^4$	$2.92 \cdot 10^5$	$-2.87 \cdot 10^5$

Table 33: Critical loads at section BB'

Critical Point	$\mathbf{T_y}$ [lbf]	$\mathbf{T_z}$ [lbf]	$\mathbf{M_y}$ [lbf.ft]	$\mathbf{M_z}$ [lbf.ft]	$\mathbf{M_x}$ [lbf.ft]
A	$-1.64 \cdot 10^4$	$2.40 \cdot 10^4$	$5.35 \cdot 10^5$	$4.79 \cdot 10^5$	$-2.17 \cdot 10^5$
D	$-3.11 \cdot 10^4$	$3.36 \cdot 10^4$	$7.96 \cdot 10^5$	$9.08 \cdot 10^5$	$-4.14 \cdot 10^5$
E	$-2.16 \cdot 10^4$	$1.32 \cdot 10^3$	$8.67 \cdot 10^4$	$6.31 \cdot 10^5$	$-2.87 \cdot 10^5$

Table 34: Structural loads at section CC'.

Rear fuselage structural design

The fuselage is made of 72 stringers. Thanks to circular cross section of the fuselage and thus the symmetry equations are simplified. To simplify computation, we assume the boom section is the same for each. Inertia of the fuselage section is computed through:

$$I_{yy} = \sum_{i}^{N_{booms}} Bz_i^2 \qquad I_{zz} = \sum_{i}^{N_{booms}} By_i^2 \tag{7.21}$$

As the booms only sustain bending, the stress in each boom is computed using the following equation:

$$\sigma_{xx,i} = \frac{M_y}{I_{yy}} z_i - \frac{M_z}{I_{zz}} y_i. \tag{7.22}$$

The minimal boom section is determined using the yield strength limit and a safety factor $s = 1.5$.

$$\frac{\sigma_{yield}}{s} = \sigma_{max} \geq max(\sigma_{xx,i}) \tag{7.23}$$

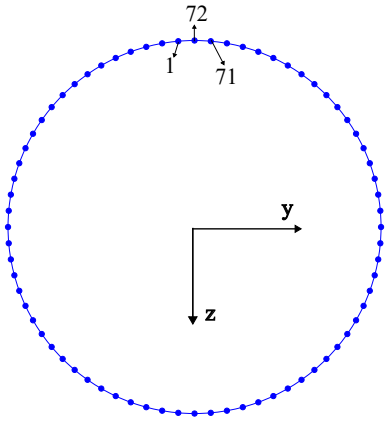

Figure 7.19: Fuselage booms representation.

The thickness of the panel is computed through the shear flow which itself is computed through equations linking shear flow from one panel to another and the second expression that exploits symmetry of the circular section (no torque).

$$q^{i+1} = q^i - \frac{T_z}{I_{yy}} Bz_i - \frac{T_y}{I_{zz}} By_i + \frac{M_x}{2A} \quad , \quad q^{71,\,72} = -q^{72,\,1}. \tag{7.24}$$

For the booms, the minimal thickness is determined using the shear strength limit and a safety factor $s = 1.5$.

$$\frac{max(q^i)}{t} \leq \tau_{max} = \frac{\tau_{yield}}{s} \tag{7.25}$$

The obtained results for the stringers and the panels are resumed in Tab. 35. The stringers are designed to prevent local buckling. Stringers between section AA' and CC' correspond to a critical load of 104 ksi while stringers between sections CC' and BB' corresponds to critical load of 83.4 ksi which ensure no buckling as the maximal stress in the stringers is 72.4 ksi.

Component	Section / thickness
Stringers section AA' to section CC' [in²]	0.124
Stringers section CC' to section BB' [in²]	0.087
Skin [in]	0.012

Table 35: Structural dimension of rear fuselage.

Rivet number or rivet pitch	Value
Number of rivets per foot along the fuselage axis [rivet/ft]	20
Rivet pitch along the fuselage axis [ft]	0.05
Distance between rivets on all frames [in]	0.095

Table 36: Required number of rivets on frames and along fuselage axis.

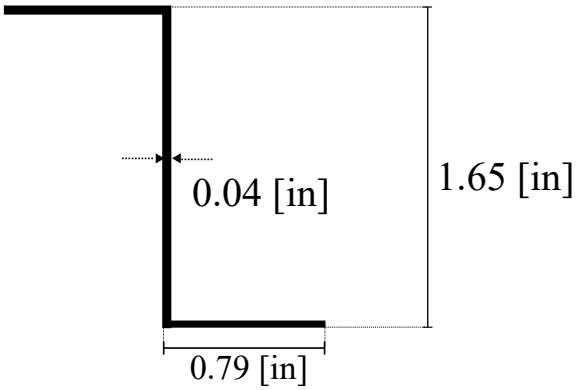

Figure 7.20: Fuselage stringers geometry between section AA' and CC'.

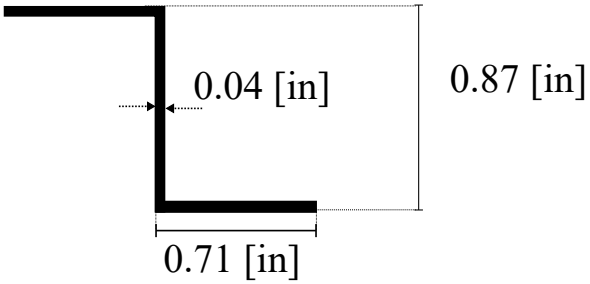

Figure 7.21: Fuselage stringers geometry between section CC' and BB'.

Rear fuselage structure assembly

As an aluminum alloy is used to build the rear fuselage structure, components are assembled using rivets. However, as the skin thickness is very thin, the rivets may not be able to be fixed to the skin. The skin thickness will therefore need to be larger to allow the use of rivets. Assuming an allowable shear load of 150.17 lbf for each rivet and knowing the maximal load per unit stringer length, the number of rivets along the centerline axis is determined and is equal to 20 rivets/ft. This necessitates placing a rivet every 0.6 in along the fuselage centerline axis.

On each frame the number of required rivets is determined using the distance available for one of the stringers, maximal load per unit stringers and the allowable load in shear for each rivet. For manufacturing simplicity, the same rivet pitch is kept for each frame based on the case that requires lowest pitch. After completing the computations, the distance between rivets is 0.095 in for all frames.

7.5.6 Wing design

Wing loads

First, the load on the wings needs to be computed in each case through an equilibrium. Shear stress are assumed to be applied at the aerodynamic center of the wing and positive along their reference axis. The moment equilibrium is performed at the AC of the wing. Loads at the wing root are written in Tab. 37.

Critical Point	$\mathbf{T_y}$ [lbf]	$\mathbf{T_z}$ [lbf]	$\mathbf{M_y}$ [lbf.ft]	$\mathbf{M_z}$ [lbf.ft]	$\mathbf{M_x}$ [lbf.ft]
A	$1.20 \cdot 10^4$	$1.18 \cdot 10^5$	$-1.78 \cdot 10^6$	$-1.96 \cdot 10^5$	$-5.08 \cdot 10^4$
D	$1.13 \cdot 10^4$	$1.32 \cdot 10^5$	$-2.05 \cdot 10^6$	$1.91 \cdot 10^4$	$-5.08 \cdot 10^4$
E	$5.76 \cdot 10^3$	$-2.07 \cdot 10^4$	$3.06 \cdot 10^5$	$2.34 \cdot 10^4$	$-5.08 \cdot 10^4$

Table 37: Loads at the wing root

Wing structural design

A similar methodology is applied to the design of the wing structure. The wing is designed with 2 spars and the section at the trailing edge is neglected as this correspond to where flaps and stabilization devices are located. The design is done at the wing root where the airfoil is symmetric. Because of this symmetry the cross inertia term $I_{yz} = 0$. The wing is built with 35 equally space stringers. This results in 1.57 in of spacing between the stringers. The position of each of the stringers is represented on Fig. 7.22. For the fuselage, the structure is designed such that the stresses are lower than the yield strength divided by a safety factor $s = 1.5$.

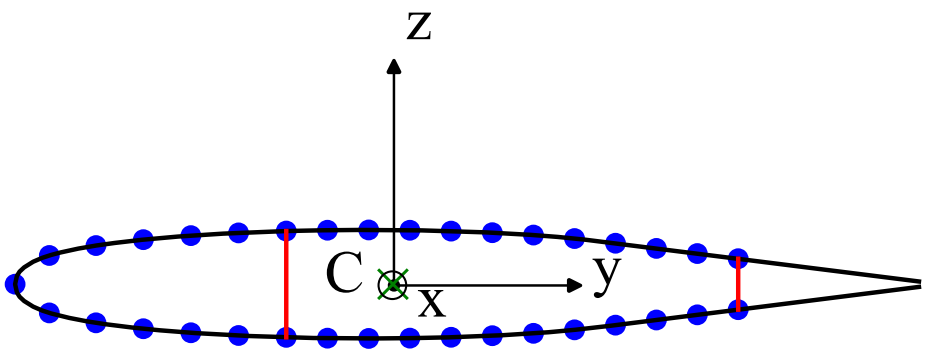

Figure 7.22: Position of stringers and spars at the wing root, centroid of the structure is indicated by C.

First, the booms section is assumed to be the same for each and stringers are assumed to be only submitted to bending. The stress is computed for each case and the case involving the largest stresses in the booms, being critical case at point D of the maneuver

envelope, is the one used to determine the boom area. As the cross inertia term is 0 the stresses are computed using:

$$\sigma_{xx,i} = \frac{M_y}{I_{yy}} z_i - \frac{M_z}{I_{zz}} y_i. \tag{7.26}$$

and the following criteria is used to determine the boom section:

$$\frac{\sigma_{yield}}{s} = \sigma_{max} \geq max(\sigma_{xx,i}) \tag{7.27}$$

The computation leads to a minimal stringer section of 0.894 [in²].

Regarding the dimension of the skin, the total shear flow in each loop is computed by adding the component of open shear flow (q_o^I) the correction term ($q^I(0)$ and the shear stress due to torsion (q_M).

$$q^I = q_o^I + q_M + q^I(0) \tag{7.28}$$

The 2 cuts are located on the left and right of the top part of the airfoil on the spars located near the leading edge. The shear flow is defined positive anti-clockwise.

First, the open shear flow is computed using the following simplified equation as the skin is assumed to carry only shear stress and the cross inertia I_{yz} is 0.

$$q^{i+1} - q^i = -\frac{T_z^{\text{web}}}{I_{yy}} Bz^i - \frac{T_y^{\text{web}}}{I_{zz}} By^i \tag{7.29}$$

T_y^{web} and T_z^{web} are defined as follows, since the wing has considerable taper, we need to account for it through the derivatives $\frac{\delta z^i}{\delta x^i}$ and $\frac{\delta y^i}{\delta x^i}$:

$$\begin{cases} T_z^{\text{web}} = T_z - \sum_{i=1}^{N_{\text{booms}}} P_z^i = T_z - \sum_{i=1}^{N_{\text{booms}}} P_x^i \frac{\delta z^i}{\delta x^i} = T_z - \sum_{i=1}^{N_{\text{booms}}} \sigma_{xx} B \frac{\delta z^i}{\delta x^i} \\ \\ T_y^{\text{web}} = T_y - \sum_{i=1}^{N_{\text{booms}}} P_y^i = T_y - \sum_{i=1}^{N_{\text{booms}}} P_x^i \frac{\delta y^i}{\delta x^i} = T_y - \sum_{i=1}^{N_{\text{booms}}} \sigma_{xx} B \frac{\delta y^i}{\delta x^i} \end{cases} \tag{7.30}$$

Once the open shear flow is computed, the correction can be obtained solving the equations expressing momentum balance and

twist rate compatibility. As both the centroid and the aerodynamic center of the wing are located on the chord the torque induced by T_y is zero. Another simplification comes from the fact that the μ is the same for each panel.

$$y_T T_z = \sum_c \int_{\text{cell}c} q_\alpha \rho \, ds + \sum_{\text{cell}c} 2A_i^c q_i^\alpha(0) + \sum_{\text{boom}j} y^j P_z^j - \sum_{\text{boom}j} z^j P_y^j \tag{7.31}$$

$$A_{II}\left(q^I(0)\Pi_I + q^{II}(0) l_{\text{spar}} + \oint_{\text{cell,I}} \frac{q_o(s)}{t}\, ds\right) = A_I\left(q^{II}(0)\Pi_{II} + q^I(0) l_{\text{spar}} + \oint_{\text{cell,II}} \frac{q_o(s)}{t}\, ds\right) \tag{7.32}$$

The length l_{spar} is the length of the spar near the leading edge, Π is the perimeter of each loop and A is the area.

The last step is to compute the shear flow due to torsion. The system of 2 equations is built from the moment equilibrium and assuming the twist rate is the same in each cell.

$$M_x = 2A_I q_{M,I} + 2A_{II} q_{M,II} \tag{7.33}$$

$$\frac{q_{M,I}\Pi_1 - q_{M,I} l_{\text{spar}}}{A_I} = \frac{-q_{M,II} l_{\text{spar}} + q_{M,II}\Pi_{II}}{A_{II}} \tag{7.34}$$

Finally, the total shear flow is computed for each case using Eq.7.28. Knowing the shear flow the thickness is determined:

$$\frac{max(q^i)}{t} \leq \tau_{max} = \frac{\tau_{yield}}{s} \tag{7.35}$$

The obtained thickness is $t = 0.028$ in.

Obtained results are summarized in Tab. 38. The shape of the stringer for the wing is represented with its dimensions on Fig. 7.23. The area is equal to the one previously determined and the dimensions are determined to ensure no local buckling using the local buckling criteria. The critical stress is 153.16 ksi while the maximum stress in the booms is 72.4 ksi. This ensures that there will be no local buckling.

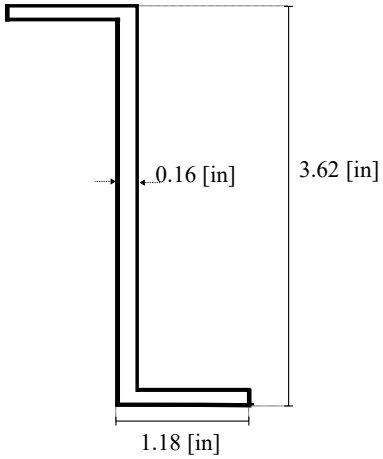

Figure 7.23: Wing stringers geometry.

Component	Section / thickness
Stringers	0.894 [in^2]
Skin	0.028 [in]

Table 38: Structural dimensions of the rear fuselage.

Wing structural assembly

As for the rear fuselage, the wing components are assembled using rivets. However, the same problem is encountered as the skin of the wing is also very thin. This skin might need to be thickened so that the rivets can be used to assemble the structure. Using the same process as the one used for the fuselage, the number of rivets on the frames and along the x-axis of the wing can be determined. The results obtained are summarized in Tab. 39.

Rivet number or rivet pitch	Value
Number of rivet per feet along the x-axis of the wing	80 [rivet/ft]
Rivet pitch along the fuselage axis	0.0125 [ft]
Distance between each rivets on all frames	0.04 [in]

Table 39: Required number of rivets on frames and along x-axis for the wing.

7.5.7 Finite Element Analysis

To validate the analytical results for both the wing and the fuselage, a structural analysis is performed using the Finite Element Method (FEM). The model is built in *Siemens NX 2212* [30] and solved using *Simcenter Samcef* [31] for a linear static analysis.

FEM analysis of the rear fuselage

Model

As illustrated in Fig.7.24, the geometry analyzed corresponds to the rear portion of the fuselage, starting at the trailing edge of the root of the wing and extending aft over a total length of 502.4 inches. In this region, the fuselage has a constant diameter of 127.6 inches and gradually tapers toward the empennage. The internal structure includes 72 longitudinal stringers with a cross-sectional

area of 0.124 in² as shown in Fig.7.20, and frames distributed regularly along the fuselage, spaced every 19.7 inches, each with a cross-sectional area of 1.75 in².

To ensure sufficient stiffness of the empennage, several bulkheads are distributed every 19.7 inches, along the conical rear section of the fuselage. Their thickness varies between 0.118 inches and 0.591 inches, depending on their location and the local loads transferred from the horizontal and vertical stabilizers.

The fuselage skin is modeled with a uniform thickness of 0.012 inches. All structural components including the skin, frames, stringers, and bulkheads are made of aluminum alloy 7068-T6511.

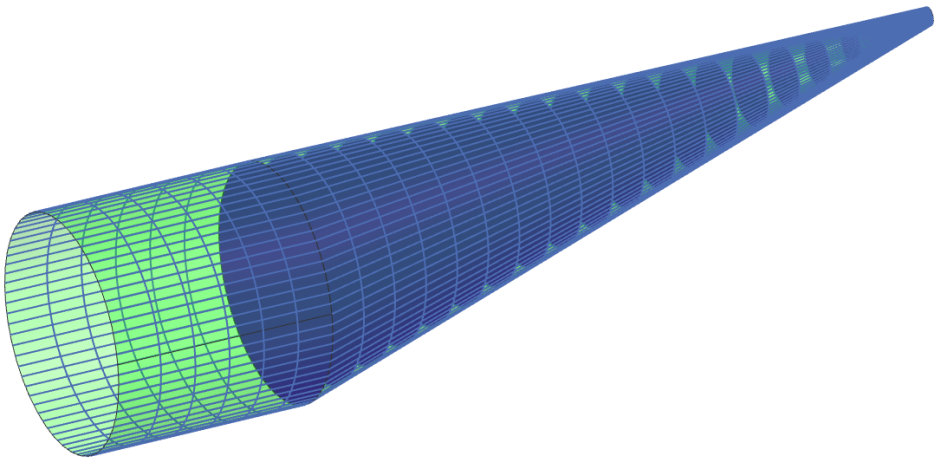

Figure 7.24: Rear fuselage structural model used for FEM analysis.

Mesh, constraints and loads

To reduce computational cost, the entire structure was modeled using only 1D and 2D finite elements. The appropriate thicknesses and cross-sectional areas, as discussed previously, were assigned to each element type. The fuselage skin and bulkheads were meshed with quadrilateral shell elements (Q4) with a mesh size of 1.57 inches, while the stringers and frames were meshed using 1D beam elements with the same discretization size.

A mesh convergence study was performed on the skin, bulkheads, frames, and stringers to ensure the results were sufficiently accurate while maintaining reasonable computation times.

To accurately replicate real boundary conditions, the fuselage cross-section located at the trailing edge of the wing root was fully clamped. Regarding the applied loads, the most critical case in structural design point of view has been considered, corresponding to the the loads obtained from the point D flight operation in the V-n diagram in Fig.7.14. Therefore, the gravity was included with the corresponding load factor ($n = 2.5$) to account for the weight of the fuselage. The aerodynamic loads from the vertical fin and horizontal stabilizer were applied locally at their respective aerodynamic centers to simulate realistic flight conditions, these point being linked to the fuselage thanks to rigid connections, as shown in Fig. 7.25.

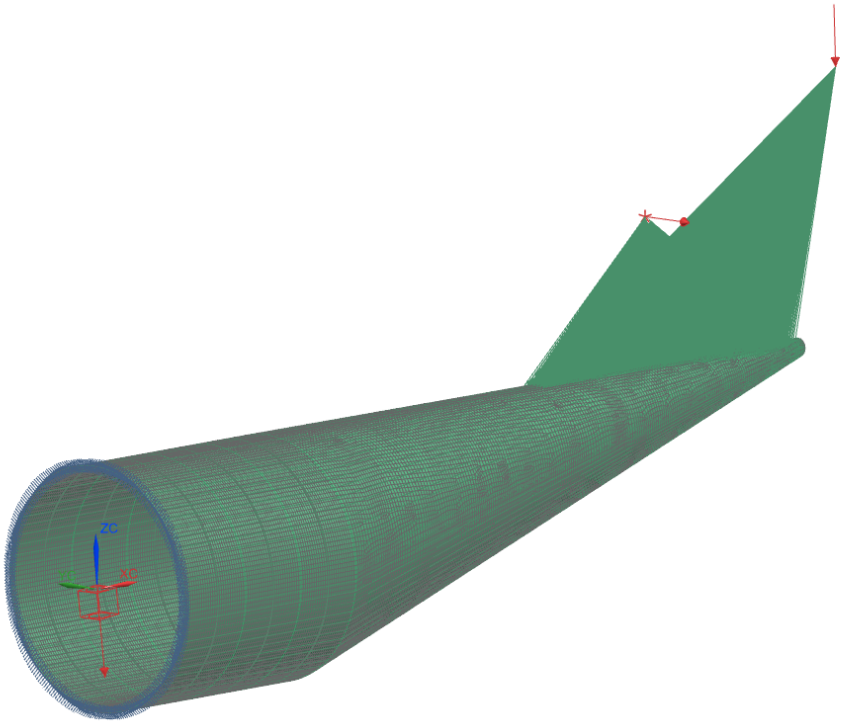

Figure 7.25: Illustration of rigid connections used to linked aerodynamic loads from the vertical fin and horizontal stabilizer, to the fuselage.

Results

The results of interest are the maximum displacement, the maximum axial load in the stringers, and the maximum shear stress in the structure.

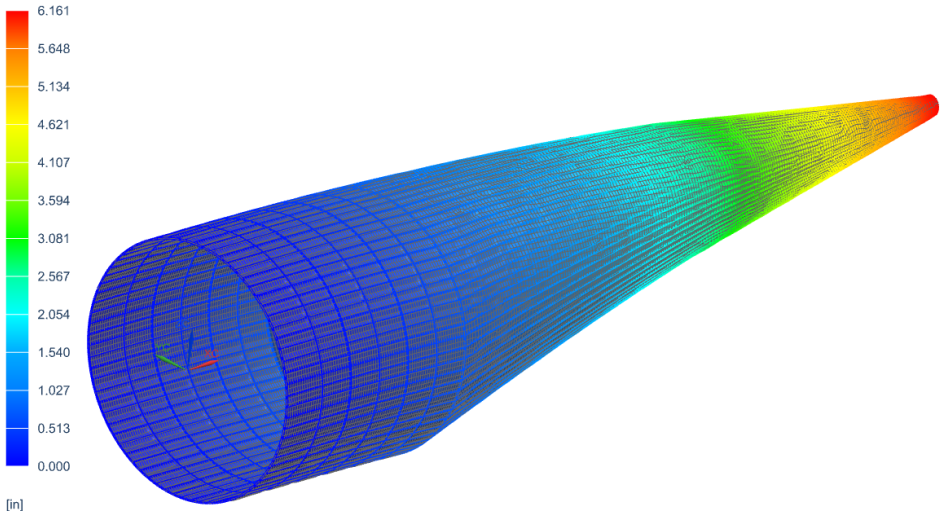

Figure 7.26: Total displacement field of the rear fuselage [in].

As shown in Fig.7.26, the maximum displacement occurs at the tip of the fuselage, as expected due to its position furthest from the constrained section and the applied loads at the empennage. This displacement reaches 6.16 inches, which remains within an acceptable range considering the structural flexibility of the rear fuselage and the extreme loading case simulated. The high value

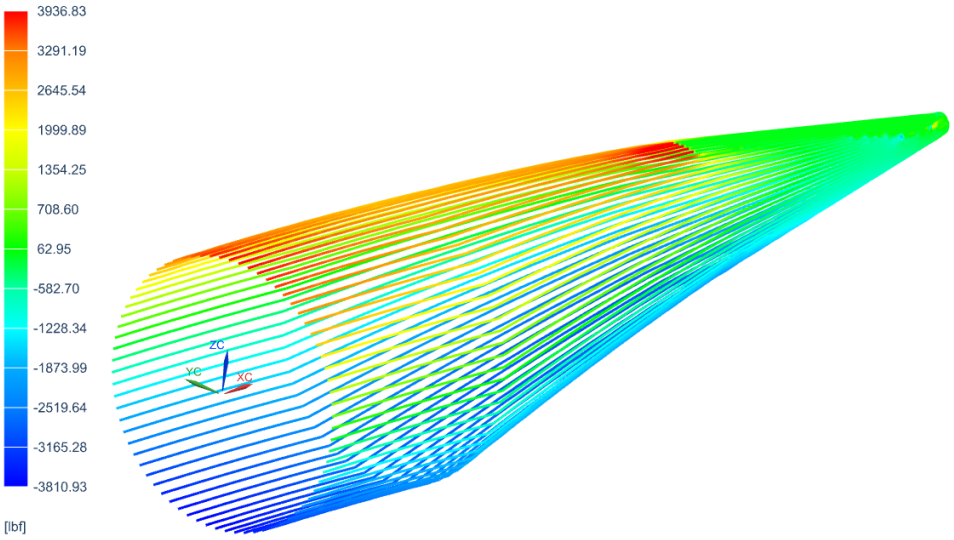

Figure 7.27: Axial load distribution in the fuselage stringers [lbf].

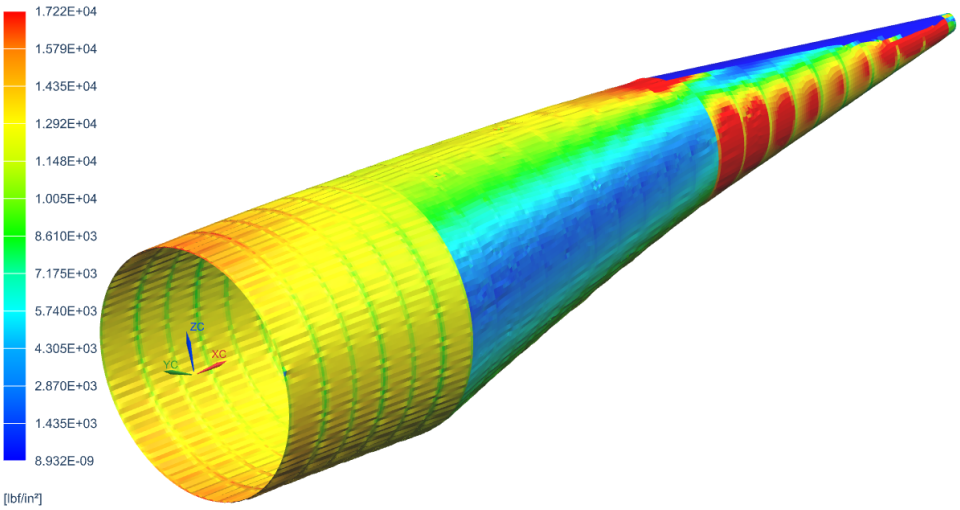

Figure 7.28: Shear stress in the fuselage skin [lbf/in²].

is primarily due to the aerodynamic forces applied by the horizontal and vertical stabilizers at the far end of a relatively slender and lightly reinforced fuselage section.

Fig.7.27 and Fig.7.28 show the axial loads in the stringers and the shear stress in the fuselage skin, respectively. The high values observed near the aft end are not physically meaningful, as the aerodynamic loads are applied locally over a small region, creating artificial stress concentrations. Only the results away from this zone particularly near the root section are considered reliable. This is where the stress state will be compared to the previously computed analytical values. As expected, the results show tensile loads in the upper stringers and compressive loads in the lower ones, which is consistent with the bending moment induced by the aerodynamic loads from the empennage.

Comparison of FEM and analytical results

As given in Tab.40, the values obtained from the FEM analysis at the clamped section of the fuselage can now be compared with the analytical results to verify that both methods perform consistently.

	Analytic	**FEM**	**relative error [%]**
Maximum displacement	/	6.2[in]	
Maximum axial stress σ_{max}	72.42 [ksi]	31.75 [ksi]	128
Maximum shear stress τ_{max}	36.27 [ksi]	17.22 [ksi]	110

Table 40: Comparison of maximum displacement, axial and shear stress obtained analytically and with the FEM analysis for the rear fuselage.

A clear difference can be noted between the obtained results using FEM and analytic computation method. As mentioned before, the analytical method is based on several assumptions including the hypothesis that stringers only retain axial forces and panels only sustain shear stress. In real load cases, this is not true as both will sustain the two types of stress. The validity of the assumption decreases as spacing between the stringers increases. As spacing between stringers is significant (2.76 in), the difference between 2 methods is non negligible. However, it is important to notice that stresses in the FEM are lower than the one computed analytically. The structure is therefore over dimensioned and is able to sustain the flight.

FEM analysis of the wing

Model

Thanks to the symmetry of the wing, the analysis is performed on a half-wing model, allowing a significant reduction in computational cost and time. As shown in Fig. 7.29, the structure includes 35 stringers, each with a cross-sectional area of 0.894 in² (see Fig.7.23), and two spars with a thickness of 0.394 in, extending from the wing root to the tip. The wing also features ribs spaced every 19.7 in, each with a thickness of 0.236 in, and a skin thickness of 0.028 in. The main geometric parameters of the wing are summarized in Fig.6.5. The entire wing structure is made of aluminum alloy 7068-T6511. It can be noticed that the thickness of the spars in the wing was not chosen to be the same as the spars of the skin (as done in the analytical part), since the goal of the FEM analysis is also to simulate the structural deformations with an actual geometry of the aircraft. The assumption of equal thickness for the skin and spars was done analytically in order to simplify the problem. This will be a source of discrepancies to take into account when comparing the FEM results with the analytical ones.

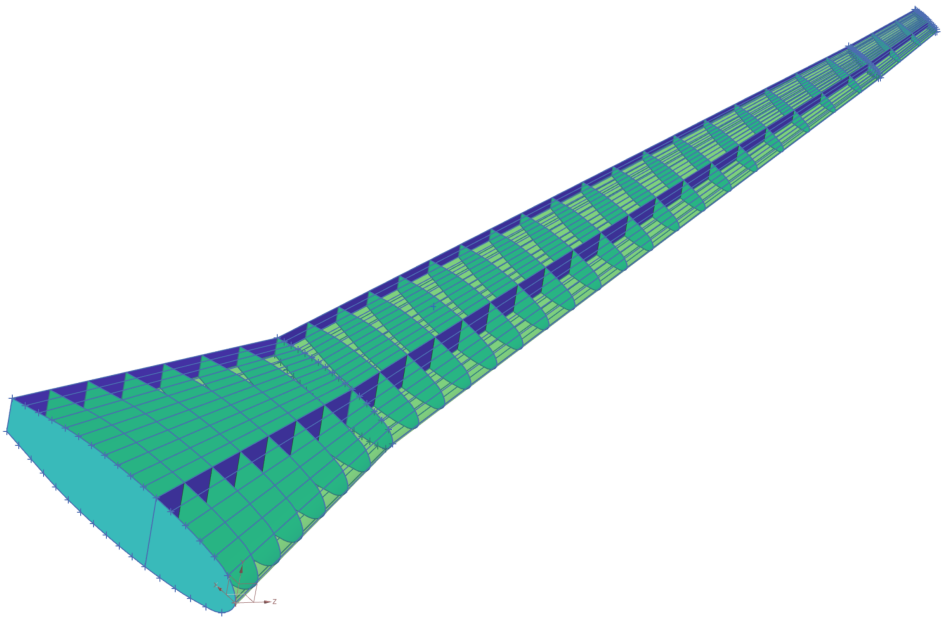

Figure 7.29: Wing structural model used for FEM analysis.

Mesh, constraints and loads

To reduce computational cost, the entire structure was modeled using only 1D and 2D finite elements once again. The appropriate thicknesses and cross-sectional areas, as discussed previously, were assigned to each element type. The wing skin, ribs and spars were meshed using second-order triangular elements (T6) with a mesh size of 1.57 inches, while the stringers were meshed using 1D beam elements using the same mesh size.

A mesh convergence study was performed on the skin, spars, ribs, and stringers to ensure the results were sufficiently accurate while maintaining reasonable computation times.

To accurately replicate real boundary conditions, the cross-section located at the root of the wing was fully clamped. Regarding the applied loads, the most critical case in structural design point of view has been considered, corresponding to the the loads obtained from the point D flight operation in the V-n diagram in Fig.7.14. Therefore, the gravity was included with the corresponding load factor ($n = 2.5$) to account for the weight of the wing. The lift, drag and pitching moment were applied at the aerodynamic center to simulate flight conditions.

Results

The results of interest for the wing structure are the maximum displacement, the maximum axial load in the the stringer, and the maximum shear stress in the skin.

As shown in Fig.7.30, the maximum displacement occurs at the wing tip, which is consistent with the bending behavior of a

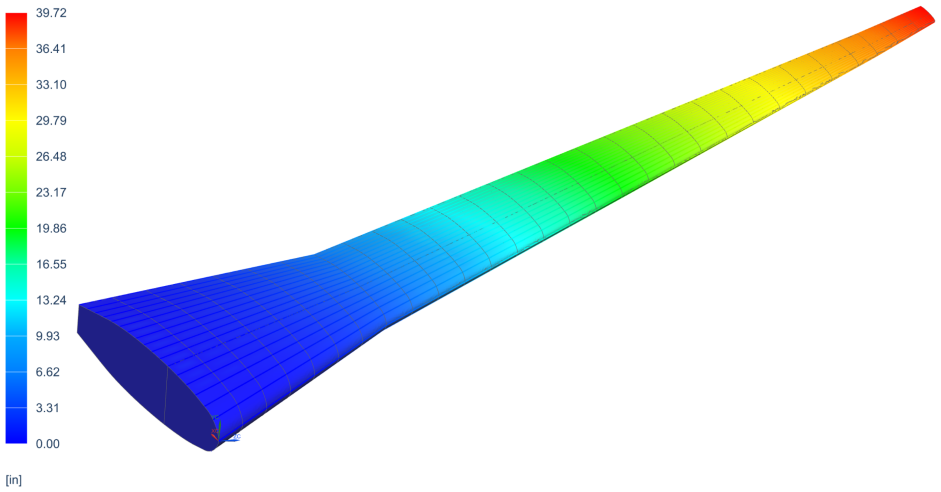

Figure 7.30: Total displacement field of the wing [in].

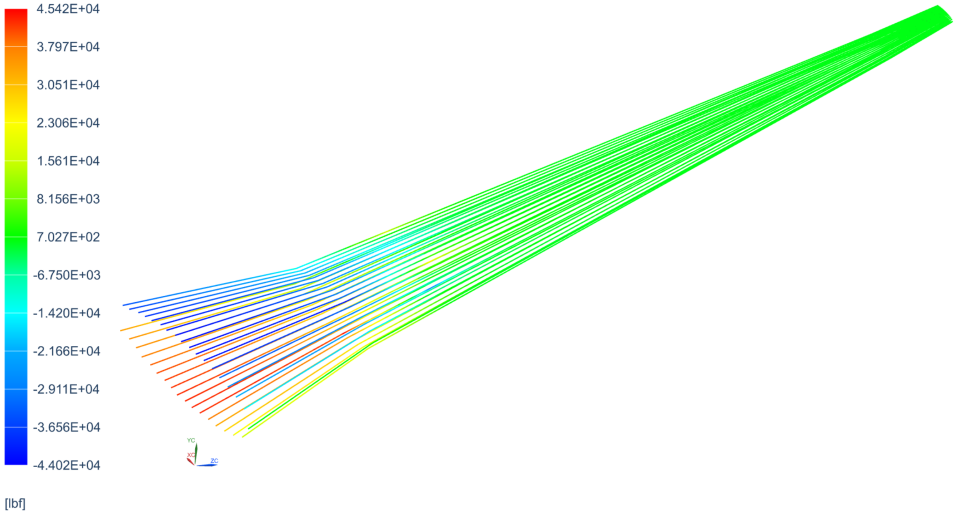

Figure 7.31: Axial load distribution in the wing stringers [lbf].

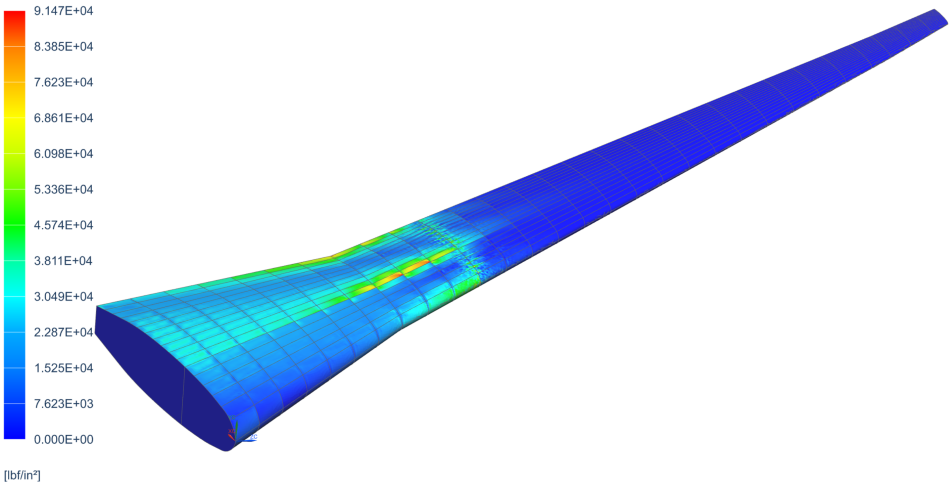

Figure 7.32: Shear stress in the wing skin [lbf/in²].

cantilevered wing under aerodynamic loading. The displacement reaches approximately 39 inches. While this is a high value, it remains realistic under the considered flight condition simulated ($n = 2.5$).

Fig.7.31 shows the axial force distribution in the stringers. As expected, the lower stringers near the wing root experience high

compressive forces, while the upper stringers carry tension, which was expected due to the bending generated by the lift force. Fig.7.32 presents the shear stress distribution in the wing skin. As the aerodynamic loads are applied over a limited spanwise region, the shear stress quickly vanishes beyond that point. Therefore, meaningful shear values are only observed near the wing root, which was the primary focus of this simulation.

The maximum stress state obtained at the root section of the wing will be compared to the previously computed analytical values.

Comparison of FEM and analytical results

As given in Tab.41, the values obtained from the FEM analysis at the root section of the wing can now be compared with the analytical results to verify that both methods perform consistently.

	Analytic	**FEM**	**relative error [%]**
Maximum displacement [in]	/	39.72	/
Maximum axial stress [ksi] σ_{max}	72.42	50.61	30.11
Maximum shear stress [ksi] τ_{max}	36.27	35.28	2.72

Table 41: Comparison of maximum displacement, axial and shear stress obtained analytically and with the FEM analysis for the wing.

As for the fuselage, the analytical method applied to the wing design is based on several assumptions. The main part of the error comes from the fact that the skin is assumed to retain only shear stress and the stringers are assumed to sustain only axial stress. As the spacing between stringers is moderate (1.57 in) the error is non-negligible. However, one can see that the error between the 2 methods regarding the wing is smaller than the one regarding the fuselage. As the space between stringers is smaller on the wing than on the fuselage the validity of the assumption is larger. As for the wing, computed stresses are lower using FEM method than the analytical one, the structure is therefore able to sustain all the loads of the critical points of the gust enveloppe.

7.6 Performance Analysis

7.6.1 Payload Range Diagram

In order to perform the Payload-Range diagram of OPULOX-1, weights specified in Tab.15 are used. The payload-range diagram for a Mach 0.85 cruise speed is represented in Fig.7.33, typically representing the case of the Design Passenger Mission. Since the payload mass (2,520 lbs) is relatively small compared to the total aircraft and fuel mass, reducing or removing it has a minimal impact on range. The fuel mass required for the longest mission is 45,068 lbs. Additionally, the fuel reserve is calculated to

sustain 45 min of flight at maximum (dash) speed, in accordance with FAR regulations [5]. At maximum takeoff weight, the aircraft achieves a range of 8,000 NM, while the maximum possible range is 8,305 NM (when there are only the crew passengers and no luggage), which fit with required missions' range.

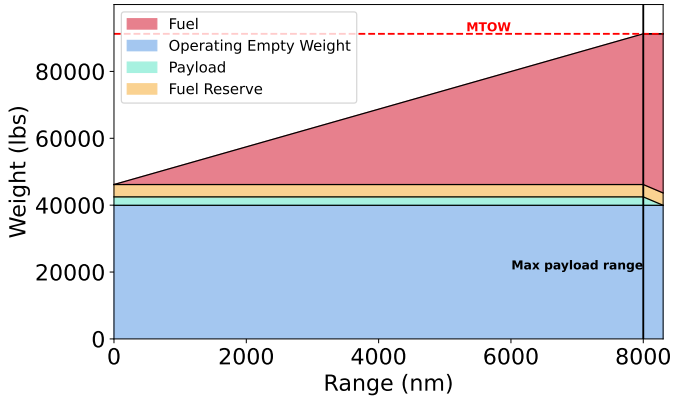

Figure 7.33: Payload-Range Diagram for cruise Mach of 0.85

Since the cruise Mach number can vary depending on the mission requirements, a new payload-range diagram is presented in Fig. 7.34 for a maximum cruise Mach number of 0.935. The increase in cruise speed leads to higher drag, primarily due to compressibility effects, and increases fuel consumption. As a result, the aircraft's range decreases, as expected. In this configuration, the maximum range with all passengers and luggage onboard is 5815 NM, and it increases to 6050 NM when flying without payload.

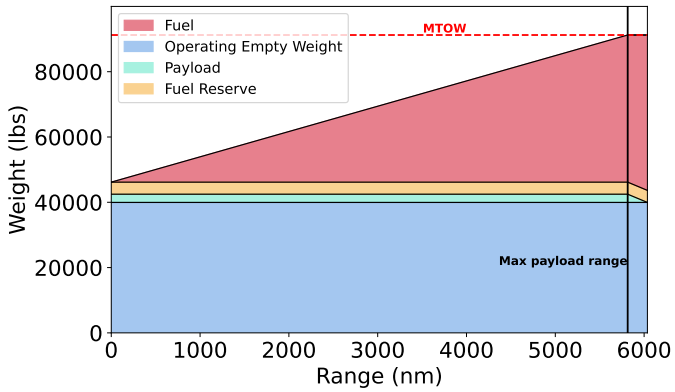

Figure 7.34: Payload-Range Diagram for cruise Mach of 0.935

For the Design Passenger Mission, all three fuel tanks are full, whereas for the other required missions, only parts on the wing tanks are filled, while obviously keeping the aircraft within stability margins.

The following pie chart represents the contribution of each flight phase in the total full weight for the Design Passenger Mission.

Figure 7.35: Fuel weight contribution during each flight phase.

As expected for this ultra-long range mission, the main part of the fuel is consumed during cruise.

7.6.2 Takeoff

The aircraft must be capable of taking off from a 6,000-foot runway under standard sea-level conditions on dry, grooved concrete, meeting the requirements for passenger mission. Economic missions, such as winter flights to Aspen or summer flights to Mexico City, involve varying environmental conditions, including higher temperatures and optimized runway configurations, which affect takeoff roll distances and overall performance. Additionally, factors such as passenger weight, baggage, and cargo (such as wine transport on the Napa-Mexico flight) influence the required takeoff distance. Evaluating these parameters ensures optimized aircraft performance that meets operational needs while adhering to safety and regulatory standards. This maximum takeoff field length must be respected, even if the aircraft experiences an engine failure beyond the decision speed during takeoff.

The methodology followed to determine takeoff distances is described in Raymer's [25] and Gudmundsson's [20] books. An obstacle clearance of 50 feet defines the point at which the aircraft has completed takeoff.

The takeoff phase is divided into the ground roll (X_G), rotation (X_R), and transition (X_{TR}) distances, as shown in Fig.7.36. During the ground roll, the horizontal forces acting on the aircraft include thrust, drag, and friction from the wheels in contact with the runway. Assuming a flat, dry, grooved concrete surface with a friction coefficient of $\mu = 0.04$ as mentioned in [20], the ground roll distance is the distance required to accelerate from zero to the liftoff velocity which is approximated as $1.1 \cdot V_{\text{stall}}$, where the stall speed is $V_{\text{stall}} = 122$ kts.

During this phase, drag is primarily affected by the deflected flaps and deployed landing gear.

In the event of an engine failure during takeoff, the rudder is deflected to compensate for the yaw caused by asymmetric thrust.

Both the rudder deflection and the inoperative engine contribute to increased drag. An idea of the augmentation in drag is presented in Section 7.4.2.

If the failure occurs before the decision speed V_1, braking devices are applied, and takeoff is aborted. Otherwise, the aircraft must reach sufficient velocity to attempt a climb and clear the 50-foot obstacle.

The rotation for liftoff occurs within 2.5 seconds, at V_{LOF} for all engines operative, and at V_2 after the incremental ground roll for a one-engine-inoperative takeoff.

The transition phase (X_{TR}) consists of acceleration from V_{LOF} to V_2 along a circular arc with radius R, determined by the mean velocity and load factor.

Considering double-slotted flaps deflected to 20°, generating a maximum lift coefficient of 2.12 , and the stall velocity at takeoff, the takeoff distances for OPULOX-1 can be determined. Each segment of the takeoff phase at sea level (Napa and KVNY airports case) and at an 7500-feet altitude (Aspen and Mexico City airports case) is shown in Tab. 42, with the total distances summarized therein.

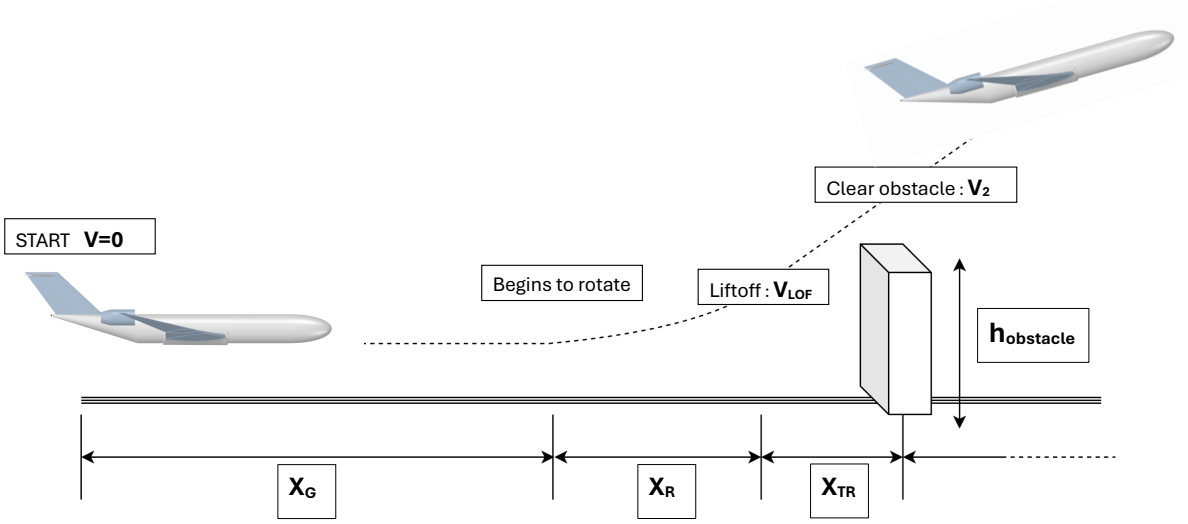

Figure 7.36: takeoff phases.

As seen in Tab.42, the short takeoff objective is reached by quite a good margin. This allows OPULOX-1 to take off in a greater number of airports around the world and makes it very useful to reach more specific airports than a classical long-range business jet.

	Ground Roll	Rotation Distance	Transition Distance	Total Takeoff field length [ft]
Distance	X_G [ft]	X_R [ft]	X_{TR} [ft]	(requirements)
Sea level	$3,583$	453	228	$4,268\ (< 6,000)$
7,500 ft altitude	$4,489$	507	228	$5,224\ (< 6,000)$

Table 42: Takeoff performance data for OPULOX-1 at different altitudes.

7.6.3 Climb

After takeoff, OPULOX-1 is expected to climb to a cruise altitude of 43,000 ft. The climb diagram representing this phase is described in Fig.7.37.

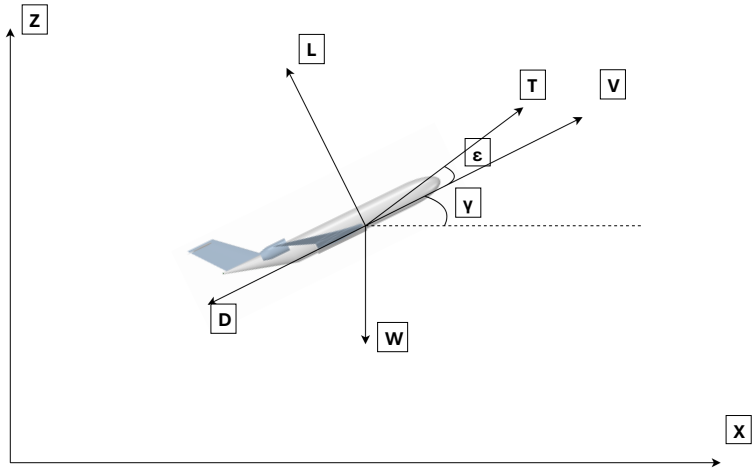

Figure 7.37: Climb Diagram.

It is assumed that the velocity V is aligned with the thrust T, hence $\varepsilon = 0$. During this part of the flight, assuming that the thrust is aligned with the aircraft velocity and that no turn is initiated, the equations of motion can be written as

$$T = \frac{1}{2}\rho C_D V^2 S + W \sin\gamma \tag{7.36}$$

$$L = W \cos\gamma \tag{7.37}$$

$$\gamma = \arcsin(\frac{T - D}{W}) \tag{7.38}$$

where γ is the angle of climb (AoC). The maximum available thrust is computed based on the thrust relation [22], explained in

the propulsion section 7.1. The equations of motion are adapted to a steady climbing flight. The airplane's climb capabilities can be evaluated using the Rate of Climb (RoC) indicator, which is an excellent measure and computed in this way.

Solving these equations allows for the determination of the vertical component of velocity, also known as the Rate of Climb (RoC). This parameter, along with the corresponding Angle of Climb (AoC), is typically represented as a function of equivalent airspeed and altitude.

The drag has been approximated as a function of altitude and Mach number and based on the zero-lift drag coefficient found for cruise in section 7.4.2, where Mach number itself is assumed to vary linearly with altitude.

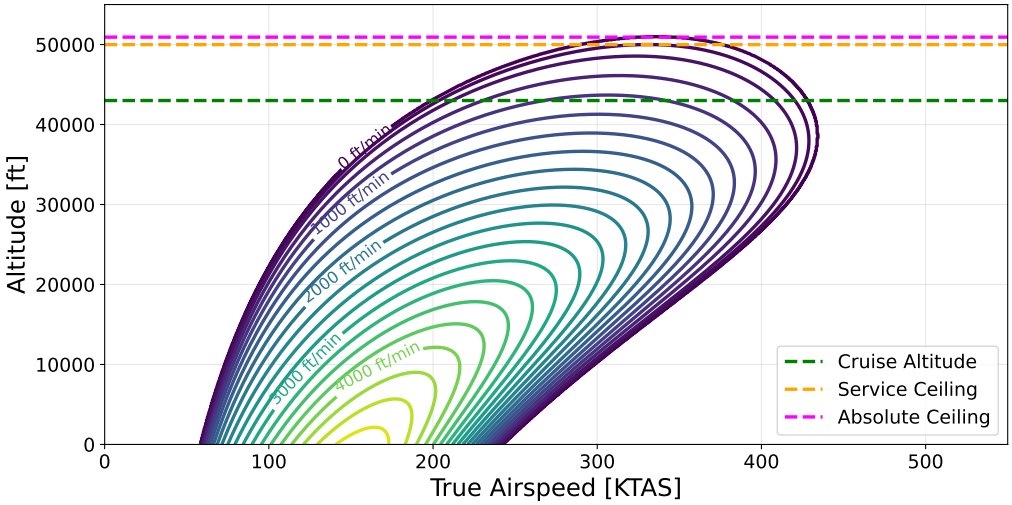

Figure 7.38: Rate of Climb Diagram.

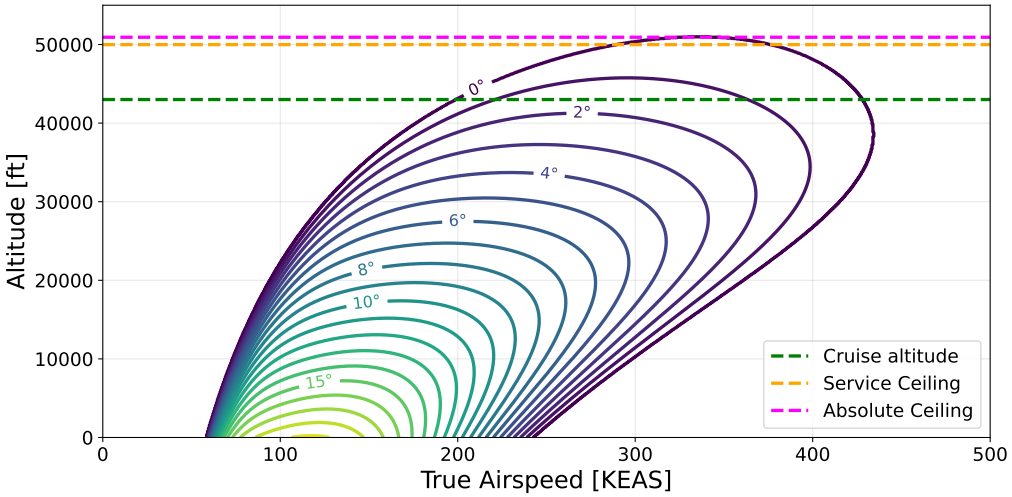

Figure 7.39: Climb Angle Diagram.

As can be seen, when reaching the cruise altitude of 43,000 ft, the climb is still possible, meaning that the ceiling altitude of OPULOX-1 is a bit higher than the cruise altitude.

The absolute and service ceiling altitudes of 49,990 ft and 50,925 ft are respectively defined as the highest altitude for a climb rate of 0 and 100 ft/min, which is higher than cruise altitude by quite a margin due to the over-dimensioned chosen engines.

The time required to reach the target altitude $h = 43,000$ ft from sea level and the corresponding horizontal distance covered are summarized in Tab.43.

t_{climb}	[min]	14
x_{climb}	[NM]	40

Table 43: Climb time and corresponding horizontal distance traveled in that time.

7.6.4 Turning performance

This section aims to analyze the characteristics of a steady, constant-velocity turn. As shown in Fig. 7.40, an aircraft banking at angle ϕ must generate enough lift to both counteract its weight and provide the necessary centripetal force for a steady turn. This requires the lift to exceed the aircraft's weight, otherwise it would lose altitude. Consequently, the airframe experiences additional loading, represented by the load factor $n = L/W$. Expanding the set of equations governing the airplane's motion in this turning condition allows for the evaluation of the aircraft's turning performance through the following expressions:

$$\text{Turn radius:} \quad R = \frac{V^2}{ng\sin\phi} = \frac{V^2}{g\sqrt{n^2-1}}, \tag{7.39}$$

$$\text{Turn rate in radian/sec:} \quad \dot{\psi} = \frac{g\sqrt{n^2-1}}{V} = \frac{V}{R}. \tag{7.40}$$

The aircraft's minimum turning radius and maximum turn rate are constrained by its velocity. At low speeds, these limits are dictated by stall conditions, while at higher speeds, they are restricted by the available thrust. Therefore, drag has been taken into account once again. As mentioned, because drag depends on speed and altitude, the corresponding drag coefficient for cruise conditions (maximum cruise speed V_C and cruise altitude) has been used.

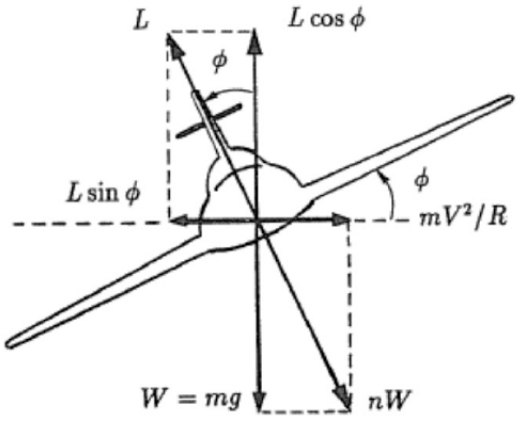

Figure 7.40: Forces acting on an aircraft in a turn, illustrating the relationship between lift, weight, load factor, and centripetal force. [24]

The turn performance map in Fig. 7.41 represents a visualization of Equations 7.40 and 7.39, showing how the aircraft maneuvers

at different airspeeds.

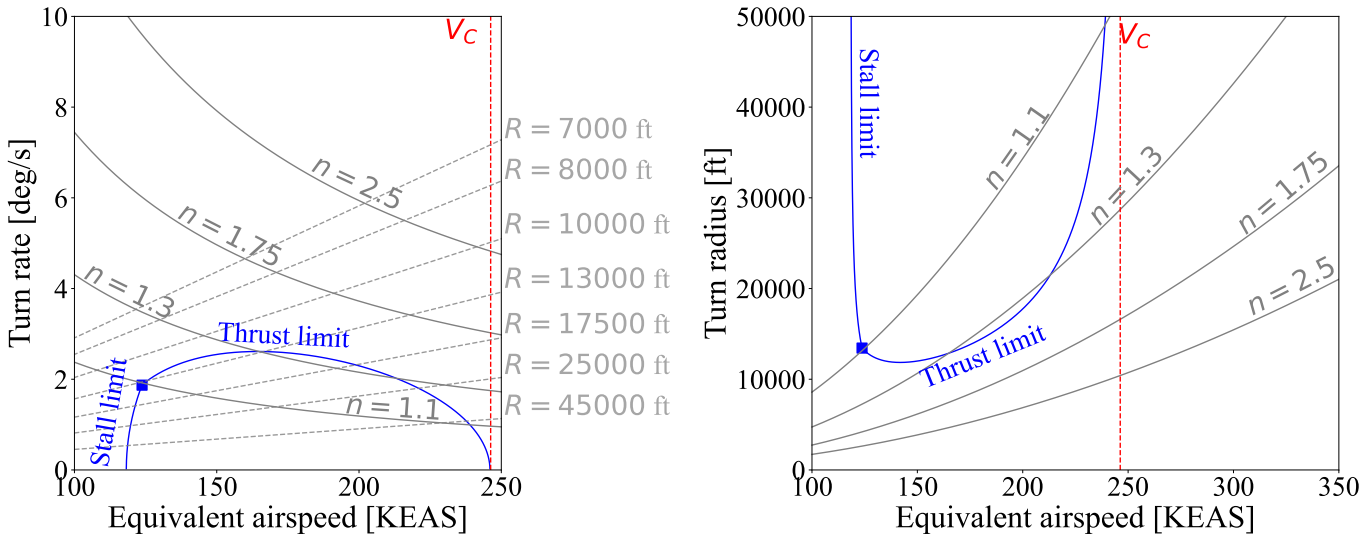

(a) Turn rate diagram.

(b) Turn radius diagram.

Figure 7.41: Turn performance diagrams for the jet OPULOX-1 at design cruise altitude of 43,000 ft.

The turn rate diagram illustrated in Fig. 7.41a shows the aircraft maneuvering capabilities, highlighting constraints imposed by stall at low speeds and thrust limitations at high speeds. At low speeds, achieving a high turn rate requires greater lift, increasing the angle of attack and leading to stall. At high speeds, maintaining a high turn rate demands greater centripetal accelerations, resulting in increased drag that exceeds available thrust.

The optimal maneuvering speed lies between these two constraints, where the highest turn rate can be sustained without exceeding aerodynamic or propulsive limits.

In the same way, Fig. 7.41b illustrates how the aircraft radius varies with airspeed and load factor. At low speeds, the aircraft can achieve tighter turns, but stall limits the minimum turn radius. At high speeds, the turn radius increases significantly due to the greater centripetal force required, and is eventually constrained by thrust limitations.

These two diagrams define the aircraft's operational turning zone, which is below the blue line limit in the turn rate diagram and above the blue line limit in the turn radius diagram, indicating the range of possible turns. It can be noted that, in no case, the structural limit load factor $n = 2.5$ is reached.

7.6.5 Landing

As it has been done for the takeoff distances calculations, the Raymer's [25] and Gudmundsson's [20] books have been used for the section. The landing phase is divided into the approach (X_A), the flare (X_F), the free-roll (X_{FR}), and the braking (X_{BR}) distances, as shown in Fig.7.42.

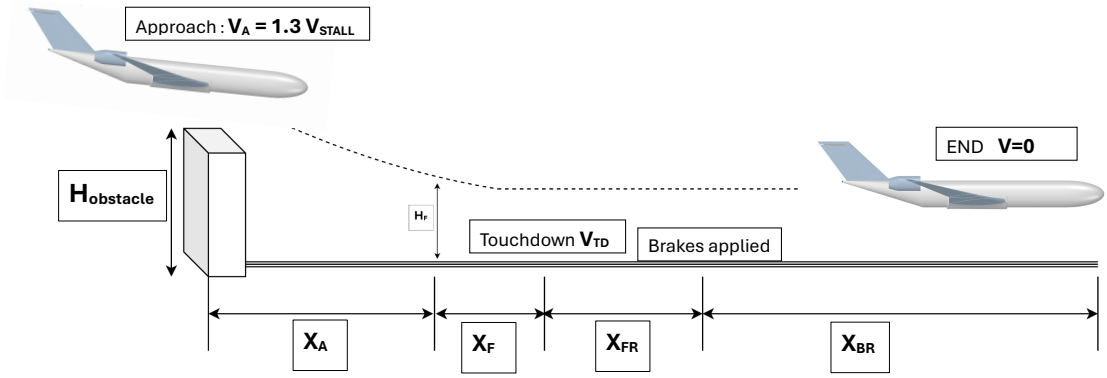

Figure 7.42: Landing phases.

The various velocities involved in landing are derived from the stall speed.

The flare distance is function of the load factor and of the speed. When the aircraft has touched the ground, a free roll of approximately 2 seconds is assumed [25] before applying the braking systems. The resulting free roll distance X_{FR} is the one traveled during this time-lapse with the touchdown velocity.

The brake roll distance (X_{BR}) is computed using a time-stepping method, integrating deceleration due to aerodynamic drag, braking force, ground friction and lift reduction. At each step, the aircraft's velocity and position are updated until it comes to a complete stop.

Results are summarized in Tab.44, for both sea level and higher altitude airports. The last column named "Best possible landing length" considers the activation of the reversed thrust system that the GE Passport has in order to decrease the landing length. The GE Passport engine is equipped with a reverse thrust system known as the Planar Exit Rear Target® (PERT®) thrust reverser. This system is integrated into the nacelle developed by Nexcelle—a joint venture between Safran Nacelles and Middle River Aerostructure Systems. The PERT® system is designed to redirect engine thrust forward, aiding in deceleration during landing, especially on short or slippery runways. It features a target-type mechanism with movable panels that deploy to reverse the thrust direction [28].

	Approach	**Flare**	**Free roll**	**Braking**	**Total landing length [ft]**	**Best possible landing length [ft]**
Distance	X_A [ft]	X_F [ft]	X_{FR} [ft]	X_{BR} [ft]	According to FAA requirements	Reversed thrust considered
Sea level	939	30	122	608	$2,175$ $(< 6,000)$	$1,699$
7,500 ft altitude	930	48	155	$1,693$	$2,826$ $(< 6,000)$	$1,871$

Table 44: Landing performance data for OPULOX-1 at different altitudes.

7.7 ADS

This section provides some results from ADS software developed by OAD [2]. This software is used to design and perform analysis of aircraft, it is based on books such as Raymer[25], and USAF DATACOM [17].

The *Performance analysis* section allows for the estimation of a large set of data and it's interesting to compare the performances computed with ADS and by other analytic methods.Fig. 7.43 shows the design of the OPULOX-1 on ADS. One of the main differences is on the wing, where there is no option to design a wing with multiple sweep angles. The wing on the OAD is designed to be as similar as possible despite lacking the double-sweep.

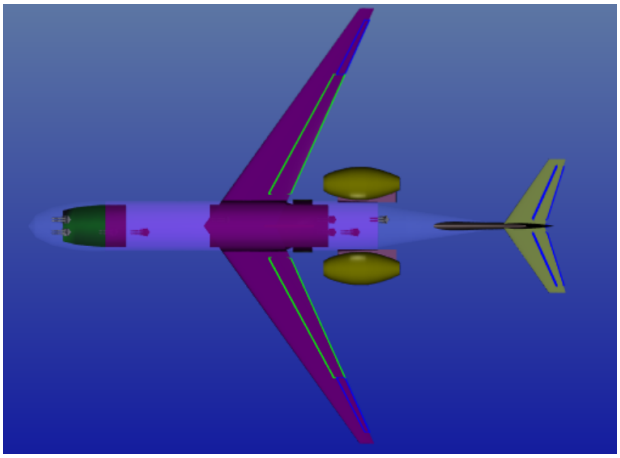

(a) Top view of the design.

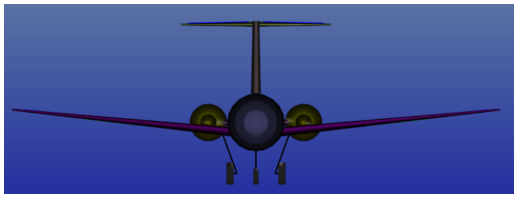

(b) Front view.

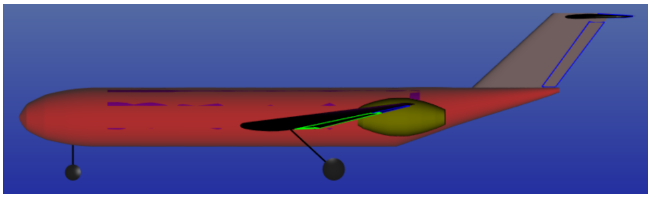

(c) Side view.

Figure 7.43: Different views of the design in ADS.

The current version of the software overestimates the sfc of turbofan engine. In order to achieve the range and cruise speed with the same limitation of fuel, the maximum thrust of the engines used is larger than the thrust from the chosen GE Passport. Therefore, the following results are displayed for cruise, but they are not as accurate for different flight conditions, like take-off for example.

On the following table Tab.45, some main performances are shown. The mach number achieved is lower than the design Mach, and the range is also slightly reduced. One of the main differences, as expected, is the take-off distances that is much smaller than the actual one due to the engines used on ADS. The SFC is higher and the range is reduced with ADS, the fuel consumption is thus much smaller on ADS.

	ADS	OPULOX-1
Weight [lbs]	$91,258.04$	$91,258$
SFC [lb/(lbf·hr)]	0.5573	0.5225
Fuel weight [lbs]	$42,879.86$	$45,068$
Mach [-]	0.84	0.85
Cruise range [ft]	$47,562,336$	$48,609,000.3$
Stall velocity [kt]	127.43	122
Take off distance [ft]	$3,225.06$	$4,268$

Table 45: Main performances computed with ADS compared to the OPULOX-1 design.

After reviewing the performance, the derivatives can also be analyzed and compared with the ones in section 7.2.2, and same for the drag coefficients in section 7.4.

The purpose is to validate the order of magnitude of the results achieved using theory.In analyzing the results, some small differences can be observed due to the approximations made, the geometrical differences between the models, and also the difference in mach number. However, all of the derivatives have the same sign, and are on the same order of magnitude. This gives some confidence in the derivatives computed with the analytical method.

Derivative	ADS [/rad]
C_{L_α}	6.072
C_{D_α}	0.247
C_{M_α}	-2.004
C_{L_u}	0.627
C_{D_u}	0.001
C_{M_u}	-0.203
C_{L_q}	11.794
C_{D_q}	0
C_{M_q}	-53.917
$C_{L_{\dot\alpha}}$	1.852
$C_{D_{\dot\alpha}}$	0
$C_{M_{\dot\alpha}}$	-9.183
C_{L_η}	/
C_{D_η}	/
C_{M_η}	/

Table 46: Longitudinal Derivative obtained with ADS.

Derivative	ADS [/rad]
C_{y_β}	-0.582
C_{l_β}	-0.208
C_{n_β}	0.018
C_{y_p}	-0.144
C_{l_p}	-0.594
C_{n_p}	-0.111
C_{y_r}	0.307
C_{l_r}	0.307
C_{n_r}	-0.120
C_{Y_ξ}	0
C_{l_ξ}	0.116
C_{n_ξ}	-0.007
C_{Y_ζ}	0.138
C_{l_ζ}	0.011
C_{n_ζ}	-0.055

Table 47: Lateral derivatives obtained with ADS.

For the drag at the lift coefficient considered, the value of the drag is coherent with the one computed in Tab.21. ADS used a value of design lift that is different from the one used in the section 7.4. The Tab.48 shows the value corresponding the same lift.

	ADS	OPULOX-1
Lift L [N]	426,035	426,035
C_L [-]	0.635	0.468
$CD_{tot}[-]$	0.04294	0.0318
CD_0 [-]	0.02702	0.02589

Table 48: Aerodynamic coefficients obtained with ADS.

The first observation is that the lift coefficient is not the same for the two cases.This is due to the underestimation of the cruise mach made by ADS. Moreover, the zero lift drag values are close to each other, which depends mainly on the geometry. This gives confidence in the computed results which were previously made. The main difference between the two total coefficients is due the lift coefficients.

To conclude, ADS is a great tool to compare the previous results with the ones obtained with the design on the software. It allows for more confidence in the similar results, and leads to more critical analysis of the differences. This iteration didn't converge to a better configuration of the airplane. This shows that the Mach and the range were too small.

8 Cost analysis

The cost analysis is a key part of the development. It shows whether the project is feasible and sustainable in the long term. It is one of the main aspects that interests the customer. In this section, the work hours and production costs will be evaluated in order to estimate the selling price of the aircraft.

8.1 Method

The model used is the Eastlake Model described in the book [19] which uses a set of statistical equations that predict aircraft costs using only basic information such as empty weight and maximum airspeed.

This method was developed in 2012, so a consumer price index (CPI) needs to be taken into account. In April 2025, the CPI according of the Bureau of Labor Statistics [34] this value was 1.41.

8.2 Development cost

First the cost of developing a new aircraft are presented. So the work hours, the fixed and variables costs will be presented. These costs are essential to determine the selling price of the OPULOX-1.

The equations depend on simple values such as the weight of the structural skeleton $W_{\text{airframe}} = 30,010.34$ lb. The maximum level airspeed is $V_c = 65.01$ KTAS from Fig.7.38. The airframe is mainly made of aluminum so the fraction of composites is $f_{\text{comp}} = 0$. The flight quality must satisfy CFR Part 25 regulations. The model presents the costs for a 5-year period. The following results are based on an assumption of 100 OPULOX-1 release on this period. This means around 1 aircraft per month, this value is further explained in section 8.2.4.

8.2.1 Hours of development

The man-hours are divided into three main contributions, first, manufacturing hours are the labor man-hours required to build the N aircraft. Then the tooling hours are needed to design and build tools, fixtures, molds,... And finally the engineering hours are for the development of the aircraft design. These hours are present on Tab.49 just below.

Type	Hour [h]	Percentage [%]
Manufacturing	5, 426, 886.8	51.58
Tooling	3, 463, 254.2	31.92
Engineering	1, 630, 726.8	15.5
Total	10, 520, 867.81	100

Table 49: Man work hours for a production of 100 aircraft on a 5 years period.

8.2.2 Fixed costs

These costs are fixed costs, they are common for all the aircraft produced over the 5 year-period. Their first take in account the cost of remuneration of tooling to design built tools or molds and engineering man hours. Development refers to the cost of overheads, administration, logistics, etc. Test refers to the development and certifications with the assumption of two prototypes. All these cost are in the Tab.50.

Type of cost	Price [$]	Percentage [%]
Tooling	624, 613, 026.09	56.63
Engineering	443, 573, 785.71	40.21
Development	24, 030, 393.51	2.18
Test	10, 810, 418.49	0.98
Total	1, 103, 027, 623.81	100

Table 50: Fixed costs for a production of 100 aircraft on a 5 years period.

8.2.3 Variable costs

Then variable costs directly linked to the production of one aircraft. This includes manufacturing, and the raw materials used in the plane. quality control covers the price of technicians and the equipment required to demonstrate that the product being manufactured is identical to the design. The power plant corresponds to the cost of the engines, and the last contribution is the avionics of the plane. All these prices are displayed in Tab. 53.

Type of cost	Price [$]	Percentage [%]
Manufacturing	850, 400, 416.07	66.58
Materials	235, 800, 918.81	18.46
Quality control	178, 137, 627.16	13.95
Power Plant	12, 775, 505.60	1.0
Avionics	100, 000	0.01
Total	1, 277, 214, 467.64	100

Table 51: Variables costs for a production of 100 aircraft in a 5 years period.

8.2.4 Break-event analysis

The break-event number corresponds to the number of airplanes that must be sold to balance costs and earnings. In Tab.52, the selling prices required to achieve 20% of benefit are shown. It reveals that the higher the number of airplanes sold, the lower the selling price. The assumption of 100 airplanes is made and based on data from similar aircraft such as the Falcon 10x[12].

Rate per year	selling price [$]
5	73, 875, 263.61
10	52, 927, 811.36
15	44, 329, 260.35
20	39, 397, 037.03
25	36, 110, 038.97

Table 52: Selling price as a function of the number of airplanes sold per year with a benefit of 20%.

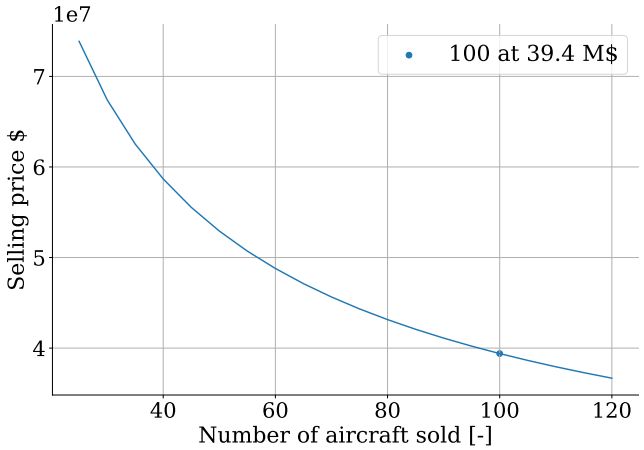

Figure 8.1: Selling price in function of the number of airplane sold in a 5-year period with a benefit of 20%.

In the case of OPULOX-1 to ensure a profit of 20% when 100 planes are sold in the 5-year period, the selling price must be 39, 500, 000$

The break-event analysis shown below in Fig.8.2 highlights the number of sales required to break even for different selling prices. The figure compares the total costs of production with the revenue. For the case of OPULOX-1, 62 airplanes are needed to break even.

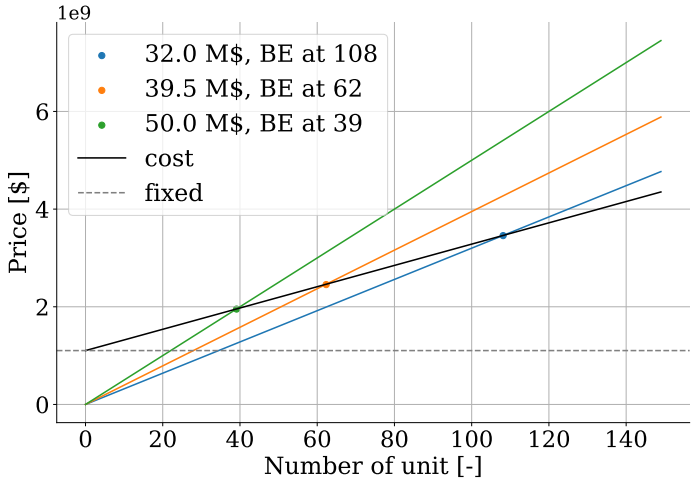

Figure 8.2: Break event analysis on a 5-year period.

8.3 Operational cost

The total annual cost for the user depends on several factors such as the number of flight hours. An assumption of 500 hours of flight per year is made. The amount of money required to own and operate the aircraft includes maintenance, storage, fuel cost, overhaul fund for the engines, and inspection costs. The salary of the crew must also be considered.

The owner may also have loan payments in addition to the generic operational cost but this is specific to each case.

	Price [$]	**Price per hour [$/h]**	**Price per flight per passenger [$/flight/pers]**
Fuel	924,129.87	1,848.26	3,925.24
Insurance	504,125.0	1,008.25	2,141.27
crew	200,000.0	400	849.5
Maintenance	13,325.0	26.65	56.59
Storage	3,000	6	424.75
Overhaul fund	5,000	10	21.23
Inspection	500	1	2.12
Total	1,650,079.87	3,300.16	7,008.714

Table 53: Annual costs for an aircraft on a 5 years period, 500 hours of flight per year, 8000nm range and 8 passengers.

So assuming 500 hours of flight per year, a flight at maximum range with 8 passengers will cost 7,008.714 $ per passengers for a total of 56,069.71 $ for the flight.

8.4 Life cycle analysis

The evaluation of an aircraft's environmental footprint must consider the entire life cycle, encompassing all stages from raw material extraction to end-of-life disposal.

In the case of aluminum, which is the only material used in the OPULOX-1 structure, the production phase alone emits several greenhouse gases, notably carbon dioxide (CO_2), methane (CH_4), and nitrous oxide (N_2O). In addition, two potent fluorinated gases, tetrafluoromethane (CF_4) and hexafluoroethane (C_2F_6), are released exclusively during the aluminum manufacturing process.

To quantify their respective contributions to global warming, the Global Warming Potential (GWP) values from the IPCC Fifth Assessment Report (AR5) are employed [18]. The total GHG emissions for each gas are then calculated using the formula:

$$\text{Emissions} = \text{mass} \cdot \frac{\text{lbs of } CO_2 \text{ per lb of material}}{\text{GWP}_{\text{gas}}} \tag{8.1}$$

where the values of GWP for CO_2, CH_4, NO_2, CF_4 and C_2F_6 are respectively 1; 28; 265; 6,630 and 11,100. The same overesti-

mated assumption of 500 hours of flight per year is taken into account to compute the total amount of burned fuel in a year. The complete breakdown of emissions across all life cycle phases is provided in Tab. 54.

	Weight [lbs]	CO_2 [lbs^{-1}]	CO_2 [lbs]	CH_4 [lbs]	N_2O [lbs]	CF_4 [lbs]	C_2F_6 [lbs]
Production (5-year period)							
Aluminum 7068 t6511	18,444	17.64	325,352	11,626	1,228	49	29
In-service (1-year period)							
Fuel	1,352,040	3.1	4,191,324	149,690	15,816	-	-
End of service: The components will either be reused, donated or recycled.							

Table 54: Life cycle GHG emissions by material production and fuel use.

The engine datasheet also insists on the fact that the emissions margin to CAEP/6 range are of NO_x: 20% and CO_2: 87% which means the aircraft engine is well below regulatory emission limits, especially for CO_2, providing high efficiency while keeping great environmental performance [4].

9 Trade-off Study

9.1 Engine Design

As one of the biggest performance objective of the aircraft is to be able to takeoff and land in short distances. This requirement leads to an overestimation of the size of the engines. In this trade-off we choose to analyze the performance of the aircraft using the PW 815GA instead of the chosen design engine, the GE Passport. This allow us to see if oversizing the engines is really worth it or if the aircraft becomes much more efficient with a smaller engine.

Both characteristics of the two engines are represented in Tab.55. The engine selection was driven by the objective of achieving

Engine	Static SL Thrust [lbf]	Dry Mass [lbs]	TSFC [lbs/lbf/hr]	BPR [-]	Length [in]	Diameter [in]
PW 815GA	16,011	3,135	0.624	5.5	105.8	50
GE Passport	18,920	3,950	0.5225	5.6	102.7	52

Table 55: Characteristic of the GE passport and the PW 815GA.

short takeoff and landing capabilities through over sizing. Comparing the takeoff distances for both engine configurations provides a meaningful metric to assess the improvement brought by the OPULOX-1 in this domain, relative to a lower-thrust engine choice. The high thrust of the GE Passport significantly enhances the aircraft's takeoff performance, demonstrating its added value compared to conventional aircraft. The results are presented in Tab. 58.

Engine	GE Passport	PW 815GA	
Weight of fuel [lbs]	45,068.91	48,530.55	+7.68 %
ZFW [lbs]	46,169.76	43,561.76	-5.64 %
Take off distance	4,264	5,955	+39.52%

Table 56: Comparison of the engines' performances.

This clearly highlights the short takeoff capabilities of OPULOX-1 .

9.2 Effectiveness of Foldable Wingtip

In order to be able to land in small airports, the feasibility of using a foldable wingtip to increase the aerodynamic efficiency of the aircraft was studied. To analyze the effectiveness of a foldable wingtip, the lift-drag ratio was studied throughout the design mission of a 8000 NM flight at Mach 0.85 and an altitude of 43000 ft. These results are then compared with those of a wing of the same dimensions but with the wingtip folded up.

The performance was calculated using a model to determine the lift required, and the subsequent drag on the aircraft. For the traditional winglet, the efficiency gain was calculated using a penalization factor of k_{wl} = 2.83 on the height of the winglet if it were considered to increase the span of the wing. This value was determined using a fit on the drag reduction data for several different aircraft [29]. The efficiency factor for the wing with wingtip can then be calculated as:

$$e_{wl} = e(1 + \frac{2h}{k_{wl}b})^2. \tag{9.1}$$

Where h represents the height of the winglet, b represents the span of the wing, and e represents the Oswald efficiency factor. Once the efficiency factor of the different variations of the wing is determined, the lift and drag can be calculated at different cruise trims to determine the effectiveness of a foldable wingtip for a long-range flight.

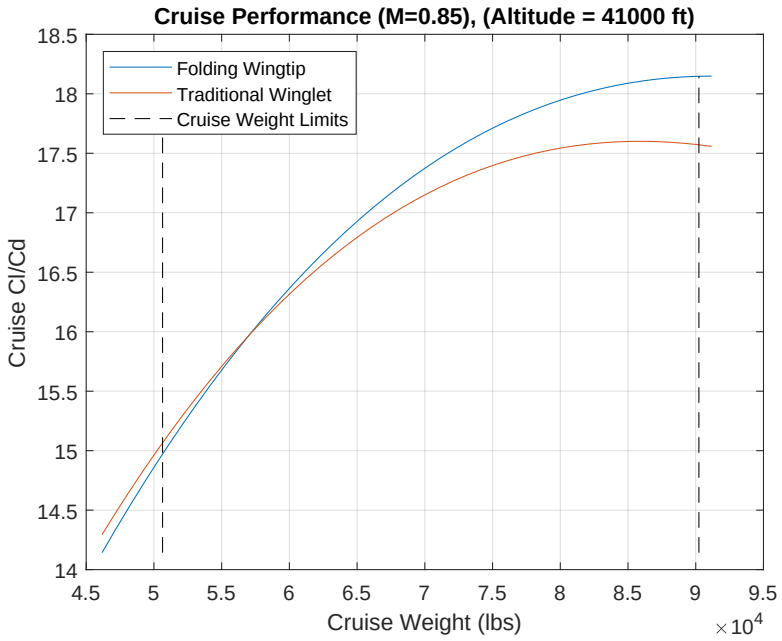

Figure 9.1: Plot showing cruise C_L/C_D values for the folding wingtip, and traditional winglet.

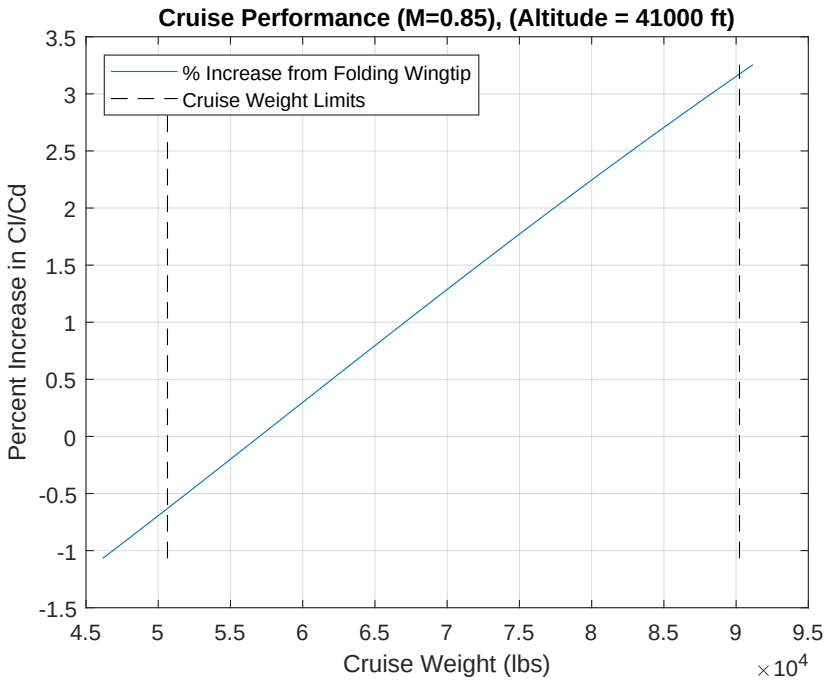

Figure 9.2: Plot showing percent increase in C_L/C_D when using a foldable wingtip compared to a traditional winglet.

Analyzing the results shows that the foldable wingtip is more aerodynamically efficient for mid-high cruise weight, while the traditional wingtip is more efficient for low-weight cruise, which is reached when the aircraft is low on fuel. The average efficiency gain is 1.11%, and is found at the mid-cruise design point used to design the cruise characteristics of the aerodynamic surfaces. The folding wingtip was ultimately chosen due to the increase in aerodynamic efficiency outweighing the downside of increased weight and mechanical complexity.

9.3 Aspect Ratio

To determine the optimal aspect ratio of the wing, the aerodynamic efficiency of the wing was maximized while ensuring the wing-fuselage structure is strong enough to support the wing loading, and that the volume of fuel is sufficient to achieve a 8000 NM cruise at Mach 0.85. In this tradeoff the wing is analyzed in these regards to determine which wing size is best for the aircraft. The evaluated wing areas were determined by maintaining a constant span, and spanwise position of the selected airfoils, while varying the root chord size to scale the wing.

		Smaller Wing	Current Wing	Larger Wing	
Surface Area [ft^2]	-5.8%	804.238	853.879	904.692	$+5.95\%$
Aspect Ratio [-]	$+6.33\%$	10.463	9.84	9.3	-5.48%
Wing C_L/C_D [-]	$+4.27\%$	20.991	20.131	18.732	-6.94%
Wing Weight [lbs]	-2.62%	4, 776.201	4, 905.115	5, 046.230	$+2.87\%$
Fuel Volume [Gallons]	-11.28%	3, 499.753	3, 945.034	4, 428.613	$+12.25\%$
MTOW [lbs]	-5.58%	86, 141.767	91, 238.687	96, 754.768	$+6.04\%$
Take off distance [ft]	-8.79%	3, 893	4, 264	4, 725	$+10.71\%$

Table 57: Comparison of Wing Sizes.

Analyzing the aerodynamic performance shows that as the aspect ratio is increased, the wing efficiency will also increase. However, the decreased fuel volume will leave the aircraft short on fuel, with the increased difficulty of storing an additional 445.281 gallons of fuel in the fuselage. If the larger wing is chosen to mitigate the current weight of fuel in the fuselage the aerodynamic efficiency of the wing will suffer due to the drastic drop in C_L/C_D. The added value of increased fuel size for the larger wing, and increased efficiency for the smaller wing are mitigated by their respective downsides, which shows that the current wing design is best at achieving the long-range high speed flight goal.

10 Conclusion

The jet OPULOX-1 has been developed to meet the expectations of the proposal from the AIAA Design Competition, which consists in designing an ultra-premium business jet combining transonic cruise performance with extended range. Additional objectives for the OPULOX-1 included being able to take off and land on short runways, and offering a high level of comfort, which led to the choice of a wide fuselage, providing generous cabin space. The increasing demand for fast, long-range, and comfortable business travel, especially in the ultra-premium market, supports the development of such aircraft.

The design process was mainly constrained by the goal of developing an aerodynamically efficient jet with structural feasibility and strong overall performance. This led to several key features of the aircarft, such as a high aspect ratio wing (AR = 9.84) to reduce induced drag, a tail-mounted propulsion system, and a span reduction mechanism to ensure compatibility with airport infrastructure. The overall geometry and aerodynamic layout were carefully design to meet the cruise requirement of 8,000 nautical miles at Mach 0.85, while keeping the takeoff field length as short as possible, with an actual takeoff distance of 4,264 ft.

For the structural design of the aircraft, analytical methods were first used to size the different components of the wing and fuselage. This ensured the structure could withstand critical loads, including those resulting from a 2.5g maneuver at Mach 1.2. These results were later validated through Finite Element Method (FEM) analysis. The simulations confirmed the structural integrity of the wing and rear fuselage, showing, for example, a wingtip deflection of approximately 1 meter under the worst-case loading, a value that remains within acceptable limits and aligns with expectations for long, slender wing designs.

The propulsion system, based on two GE Passport-class engines, provides the required thrust with a focus on cruise fuel efficiency, while also ensuring sufficient power for short takeoff performance. Compared to other candidates, the Passport engine offered the best compromise between thrust-to-weight ratio and specific fuel consumption (TSFC = 0.5225), making it the most suitable engine for OPULOX-1.

A complete life-cycle analysis (LCA) and cost study has been carried out to evaluate both the environmental impact and the economic viability of the aircraft. The use of high-strength aluminum alloy 7068-T6511 helps reduce structural weight while maintaining good fatigue resistance and manufacturing feasibility. With a projected unit price of 39.5 million and operational costs aligned with market expectations, the OPULOX-1 remains competitive both in terms of production and operating expenses.

During the project, trade-off studies played a critical role in selecting the most suitable design to achieve the best possible performance. For instance, the choice of engine, the evaluation of the foldable wingtip system, and the optimization of the aspect ratio were all the result of in-depth analyses that led to the final configuration of the OPULOX-1.

Future work could include more detailed CFD studies for transonic shock behavior, aeroelastic analyses for flutter risk, and in-depth optimization of structural reinforcements, especially in the conical tail section and wing-fuselage junction.

In the end, OPULOX-1 successfully meets its design objectives: it combines long range, high-speed cruise (up to Mach 0.935 for short missions), exceptional runway flexibility, and luxury-level cabin comfort in a technically and economically viable configuration. It stands as a promising concept for the next generation of ultra-long-range business jets.

A Summary

Variable	value [unit]
Fuselage	
Fuselage height	10.62 [ft]
Fuselage width	10.62 [ft]
Fuselage length	103.06 [ft]
Wing	
Span	101.71 [ft]
Aspect ratio AR	9.84 [-]
Gross Surface S	853.88 [ft^2]
Taper ratio λ	0.1 [-]
Chord at root	22.14 [ft]
Chord at tip	2.21 [ft]
Mean aero chord	12.13 [ft]
Mach cruise	0.85 [-]
Mach max	0.935 [-]
Cruise	
Cg position in cruise	55.73 [ft]
C_{l_w} in cruise	0.469
Stall velocity	433.48 [kts]
Cruise velocity	1,755.29 [kts]
Range	80,000 [nm]
Altitude	43,000 [ft]
Propulsion	
Motor type	GE Passport
Thrust	18,920 [lbf]
Take off distance	4,264[ft]
Landing distance	1,699 [ft]
Price	39.5 [M$]

Table 58: Summary of main information

References

[1] European Union Aviation Safety Agency (EASA). *Proposed Special Condition on CS 25.415, 25.703, 25.1385 at Amdt 18 – "Folding Wing Tip" Applicable to Boeing 777-9*. Special Condition SC D-21-9. Accessed: 2025-05-15. European Union Aviation Safety Agency (EASA), 2017. url: https://www.easa.europa.eu/sites/default/files/dfu/Consultation%20-%20SC%20D-21-9%20-%20FINAL.PDF.

[2] Optimal Aircraft Design (OAD). *ADS - Aircraft Design Software*. https://www.pca2000.com/index.html. Consulté le 23 avril 2025. 2024. url: https://www.pca2000.com/index.html.

[3] AEROAFFAIRES. *Our Fleet*. Consulted on April 22, 2025. 2025. url: https://aeroaffaires.com/our-fleet/.

[4] GE Aerospace. *GE Passport Data Sheet*. Accessed on April 24, 2025l. 2022. url: https://www.geaerospace.com/sites/default/files/2022-01/GEPassport-DataSheet.pdf.

[5] *Airworthiness Standards: Normal Category Airplanes*. Apr. 2023. url: https://www.ecfr.gov/current/title-14/chapter-I/subchapter-C/part-23#23.2430 (visited on 02/2025).

[6] Vassberg Et al. "Development of a Common Research Model for Applied CFD Validation Studies". In: (2008).

[7] Ansys. *Granta EduPack | Software for Materials Education*. https://www.ansys.com/products/materials/granta-edupack. Accessed on April 4, 2025. 2021.

[8] *Aspen/Pitkin County Airport Wingspan Restriction Briefing Paper*. Briefing Paper. Mar. 2014.

[9] Civil Aviation Authority. *General Aviation Safety Topics*. Consulté le 15 mai 2025. 2025. url: https://www.caa.co.uk/general-aviation/safety-topics/.

[10] Michael V. Cook. *Flight Dynamics Principles: A Linear Systems Approach to Aircraft Stability and Control*. Third. Butterworth-Heinemann, 2012.

[11] Adrien Crovato. "Steady Transonic Aerodynamic and Aeroelastic Modeling for Preliminary Aircraft Design". Doctoral dissertation submitted to the Department of Aerospace and Mechanical Engineering. Ph.D. thesis. Liège, Belgium: University of Liège, Oct. 2020.

[12] Dassault Aviation. *Key Figures of the Group*. https://www.dassault-aviation.com/fr/groupe/finance/chiffres-cles-du-groupe/. Accessed on April 20, 2025. 2025. url: https://www.dassault-aviation.com/fr/groupe/finance/chiffres-cles-du-groupe/.

[13] Department of Defense. *Military Specification: Flying Qualities of Piloted Airplanes (MIL-F-8785C)*. Technical Report. Washington, DC: Department of Defense, 1980.

[14] Inc. Desktop Aeronautics. *Aircraft Design: Synthesis and Analysis*. Pre-release development version. Desktop Aeronautics, Inc., 2001.

[15] Federal Aviation Administration. *Advisory Circular AC 25-7D – Flight Test Guide for Certification of Transport Category Airplanes*. https://www.faa.gov/documentLibrary/media/Advisory_Circular/AC_25-7D.pdf. Section 7.e.1: Spiral Mode Stability. U.S. Department of Transportation, Federal Aviation Administration, May 2018.

[16] *Federal Aviation Regulations - Part 25: Airworthiness Standards: Transport Category Airplanes*. https://www.ecfr.gov/current/title-14/chapter-I/subchapter-C/part-25. Accessed: 2024-04-25. 2023.

[17] R. D. Finck. *USAF Stability and Control DATCOM (AFWAL-TR-83-3048)*. Technical report. Air Force Flight Dynamics Laboratory, Wright-Patterson AFB, 1978.

[18] Greenhouse Gas Protocol. *Global Warming Potential Values*. https://ghgprotocol.org/sites/default/files/Global-Warming-Potential-Values. Accessed: 2025-03-24. 2015. url: https://ghgprotocol.org/sites/default/files/Global-Warming-Potential-Values.

[19] Snorri Gudmundsson. *Aircraft Cost Analysis*. Oxford, UK: Butterworth-Heinemann, 2014. Chap. 2.

[20] Snorri Gudmundsson. *General Aviation Aircraft Design: Applied Methods and Procedures*. Oxford, UK; Waltham, MA, USA: Butterworth-Heinemann, 2014.

[21] Koen Hillewaert and Remy Princivalle. *Introduction to Airbreathing Propulsion Systems*. Aerospace Design Project, ULiège, 2022.

[22] John D. Anderson Jr. *Aircraft Performance and Design*. New York: McGraw-Hill, 1999. isbn: 978-0070019713.

[23] Timothy R. McClung. *Airfoil Tools*. Accessed: 2025-04-25. 2023. url: http://airfoiltools.com.

[24] Ludovic Noels. *APRI0004-1 - Aircraft Design Conceptual Design*. Uliege 2024-2025.

[25] Daniel P. Raymer. *Aircraft Design: A Conceptual Approach*. 6th ed. Playa del Rey, California: Conceptual Research Corporation, 2018.

[26] Jan Roskam. *Methods for Estimating Stability and Control Derivatives of Conventional Subsonic Airplanes*. Roskam Aviation and Engineering Corporation, 1983.

[27] Mohammad H. Sadraey. *Aircraft Design: A Systems Engineering Approach*. John Wiley & Sons, 2012.

[28] Safran. *Global 7500 nacelles*. Accessed: 2025-05-14. 2023. url: https://www.safran-group.com/products-services/global-7500-nacelles.

[29] Dieter Scholz. *OPerA: Open Parametric Aircraft - Ein Entwurfstool zur Auslegung und Bewertung von Verkehrsflugzeugen*. https://www.fzt.haw-hamburg.de/pers/Scholz/OPerA/OPerA_PUB_DLRK_12-09-10.pdf. Berlin, Germany, 2012.

[30] Siemens Digital Industries Software. *Siemens NX 2212 Documentation*. 2022.

[31] Siemens Digital Industries Software. *Simcenter Samcef - Finite Element Solver*. 2022.

[32] Engineering ToolBox. *Liquids - Densities*. Accessed: 2025-02-12. n.d. url: https://www.engineeringtoolbox.com/liquids-densities-d_743.html.

[33] Egbert Torenbeek. *Synthesis of Subsonic Airplane Design*. The Netherlands: Delft University Press / Kluwer Academic Publishers, 1982. isbn: 90-246-2724-3.

[34] U.S. Bureau of Labor Statistics. *CPI Inflation Calculator*. https://www.bls.gov/data/inflation_calculator.htm. Accessed on April 19, 2025. 2025.